Microscopic 3D plant imaging with high-resolution optical coherence tomography

de Wit, J.

DOI
10.4233/uuid:73271cad-d4c1-4dbb-97b6-3682b2c1c9c4

Publication date
2023

Document Version
Final published version

Citation (APA)
de Wit, J. (2023). *Microscopic 3D plant imaging with high-resolution optical coherence tomography*. [Dissertation (TU Delft), Delft University of Technology]. https://doi.org/10.4233/uuid:73271cad-d4c1-4dbb-97b6-3682b2c1c9c4

Important note
To cite this publication, please use the final published version (if applicable).
Please check the document version above.

Microscopic 3D Plant Imaging with High-resolution Optical Coherence Tomography

Jos de Wit

Microscopic 3D plant imaging with high-resolution optical coherence tomography

Microscopic 3D plant imaging with high-resolution optical coherence tomography

Dissertation

for the purpose of obtaining the degree of doctor
at Delft University of Technology,
by the authority of the Rector Magnificus, prof. dr. ir. T.H.J.J. van der Hagen,
chair of the Board for Doctorates
to be defended publicly on Wednesday 6 December 2023 at 15.00 o'clock

by

Johannes DE WIT

Master of Science in Applied Physics,
Delft University of Technology, Delft, The Netherlands
born in Woerden, The Netherlands.

This dissertation has been approved by the promotors.

Composition of the doctoral committee:

Rector Magnificus,	chairperson
Prof. dr. S. Stallinga,	Technische Universiteit Delft, promotor
Dr. J. Kalkman,	Technische Universiteit Delft, promotor
Independent members:	
Prof. dr. J.F. de Boer,	Vrije Universiteit Amsterdam
Prof. dr. D. Weijers,	Wageningen University & Research
Prof. dr. ir. M.H.G. Verhaegen,	Technische Universiteit Delft
Dr. Y. Ling,	Shanghai Jiao Tong University
Prof. dr. B. Rieger,	Technische Universiteit Delft, reserve member

This work is part of the research programme Pathoview with project number 16293, which is partly financed by the Netherlands Organisation for Scientific Research (NWO).

The inset in the front cover and the entire back cover show an en face dynamic OCT image of a *B. lactucae* infected lettuce leaf section. It contains a several different cell types and some clear pathogen hyphae. Thanks to Sebastian and Mon-Ray from Utrecht University for preparing the plant material. The lettuce leaf image in the background by Racool_studio on Freepik and the magnifying glass by Nina Garman from Pixabay.

Printed by Ipskamp Printing

ISBN 978-94-6384-509-0

An electronic version of this dissertation is available at
http://repository.tudelft.nl/.

Contents

Summary

This thesis describes the application of optical coherence tomography (OCT) for microscopic 3D imaging of plants and plant pathogens. With its unique optical sectioning, label-free, and *in-vivo* imaging capability, OCT can complement traditional microscopic plant imaging methods. Especially, for the challenging imaging of unlabeled pathogens inside plants, OCT can have a clear advantage. However, for optimal imaging of small pathogens inside the plant the imaging depth, resolution, and specificity of OCT imaging needs to be improved, which is the topic of this thesis.

The optical imaging depth in plant leaves is largely restricted by the presence of air-filled cavities for gas exchange of the plants. The air-tissue interfaces strongly scatter light and distort the wavefront, resulting in a poor image quality. We show in chapter 2 that by infiltrating the leaf tissue with water or perfluorodecalin, the detrimental effect of the air-filled cavities on the OCT imaging is mostly removed and the OCT imaging depth is extended to the full leaf cross section of a few hundred micrometers. The improved imaging depth makes it possible to quantify the lateral resolved leaf thickness.

OCT imaging is based on obtaining the travel distance of scattered light with the interference of broadband light. In spectral-domain OCT, the interference is measured as a function of the wavenumber, and the reflectance at each depth is obtained simultaneously by taking the Fourier transform of the interference signal. This conventional reconstruction limits the axial resolution to the coherence length of the source, which can only be improved by hardware adaptations. Spectral estimation (SE) methods can estimate the scattering positions with higher accuracy than the Fourier transform by assuming sparsity in the reflectivity profile. In chapter 3 of this thesis, an SE method, the iterative adaptive approach (IAA), is optimized for OCT processing yielding an axial resolution improvement of a factor 2 to 10, dependent on the signal-to-noise ratio. Contrary to other SE methods, IAA gives a faithful reconstruction of the intensity and speckle statistics and in its computationally efficient implementation has a sub-second OCT B-scan reconstruction time.

In chapter 4, SE-OCT is made compatible with coherent refocusing techniques for extending the depth of field (DOF) and computational aberration correction. Using a short wavelength in the visible light range and a high numerical aperture for light focusing, a high lateral resolution of 0.8 µm was obtained. SE-OCT improved the axial resolution of the small-bandwidth visible light source from 8 µm to 1.5 µm. Refocusing the signal and applying computational aberration correction gave a DOF extension with a factor of 20, resulting in a high 3D resolution over a large volume.

Conventional OCT imaging has a poor specificity to different tissue structures as it images the morphology based on the scattering properties which are quite

similar for different tissue structures. Hence, distinguishing plant pathogens from the tissue in which they are growing is challenging if only the morphology is imaged. In chapter 5, we show how we imaged the temporal fluctuation of the speckle amplitude in OCT images to create contrast between pathogen and plant tissue. Dynamic OCT (dOCT) uses both the amount and the time-scale of fluctuations to create a false-color image with functional contrast of different tissue subcellular activity. *Bremia lactucae*, a downy mildew in lettuce, gives a strong fluctuation of speckle amplitude at intermediate frequencies between 0.7 and 5.5 Hz, while plant tissue gives a more stationary signal at a frequency of 0 Hz. This difference in dynamic signal is used to image *Bremia* hyphae in a living plant leaf. By segmenting the 3D pathogen structure in the dOCT leaf images we quantified the degree of *Bremia* infection and saw a significant difference in resistance between different lettuce genotypes. Moreover, we demonstrate the *in-vivo* imaging capability of OCT by imaging and quantifying the progress of *Bremia* infection over the course of three to four days and the growth speed of individual hyphae.

In the concluding chapter, promising future directions for OCT plant imaging are discussed. The extension of spectral estimation OCT for reducing phase leakage in phase-sensitive OCT imaging is discussed with potential application in OCT vibrometry. Also, 2D SE-OCT is presented for the computational enhancement of the lateral resolution.

This thesis has shown the value of high-resolution OCT for plant imaging with biological relevance. This was achieved by optical clearing-based image depth enhancement, spectral-estimation OCT for computational resolution and DOF improvement, and dynamic OCT contrast enhancement.

Samenvatting

Dit proefschrift beschrijft de toepassing van optische coherentie tomografie (OCT) voor microscopische 3D-beeldvorming van planten en plant pathogenen. OCT kan traditionele microscopische beeldvormingsmethoden die gebruikt worden voor het beeldvormen van planten aanvullen met zijn unieke eigenschappen voor het onderscheiden van diepte en het in *in-vivo* beeldvormen zonder labels. Vooral voor de uitdagende taak van het beeldvormen van ongelabelde ziekteverwekkers in planten kan OCT een duidelijk voordeel hebben. Echter, voor optimale beeldvorming van kleine en weinig contrastrijke pathogenen in de plant moeten de beeldvormingsdiepte, ruimtelijke resolutie en specificiteit van OCT-beeldvorming worden verbeterd. Dat is het onderwerp is van dit proefschrift.

De optische beeldvormingsdiepte in plantenbladeren wordt grotendeels beperkt door de aanwezigheid van met lucht gevulde holtes voor gasuitwisseling van de planten. De lucht-weefsel-overgangen verstrooien het licht sterk en vervormen het golffront, wat resulteert in een slechte beeldkwaliteit. We laten in hoofdstuk 2 zien dat door het bladweefsel te infiltreren met water of perfluordecaline, het nadelige effect van de met lucht gevulde holtes op de OCT-beeldvorming grotendeels wordt geëlimineerd en de OCT-beeldvormingsdiepte wordt uitgebreid tot de volledige dwarsdoorsnede van het blad van enkele honderden micrometers. De verbeterde beeldvormingsdiepte maakt het mogelijk om de bladdikte te kwantificeren over het hele blad.

OCT-beeldvorming is gebaseerd op het verkrijgen van de afgelegde weg van verstrooid licht door middel van interferentie van breedbandlicht. In spectraal-domein OCT wordt de interferentie gemeten als functie van het golfgetal en wordt de reflectie op elke diepte gelijktijdig verkregen door het interferentiesignaal Fourier te transformeren. Deze conventionele reconstructie beperkt echter de axiale resolutie tot de coherentielengte van de bron. Deze kan normaliter alleen worden verbeterd door hardware-aanpassingen.

Spectrale schattingsalgoritmes (SE) kunnen de verstrooiingsposities met een hogere nauwkeurigheid schatten dan die bepaald worden met een Fourier-transformatie door uit te gaan van een open structuur in het reflectiviteitsprofiel. In hoofdstuk 3 van dit proefschrift wordt een SE-methode, de iteratieve adaptieve methode (IAA), geoptimaliseerd voor OCT-reconstructie, wat een axiale resolutieverbetering oplevert van een factor 2 tot 10, afhankelijk van de signaal-ruisverhouding. In tegenstelling tot andere SE-methoden, geeft IAA een getrouwe reconstructie van de intensiteit en spikkel-verdeling. De efficiënte implementatie in de code geeft een OCT B-scan reconstructietijd van minder dan een seconde.

In hoofdstuk 4 wordt SE-OCT geschikt gemaakt om te combineren met coherente herfocusseringstechnieken voor het vergroten van de scherptediepte (DOF) en het computationeel corrigeren van aberraties. Door gebruik te maken van een

korte golflengte in het zichtbare deel van het spectrum en een hoge numerieke apertuur voor het focussen van licht wordt een hoge laterale resolutie van 0.8 µm verkregen. SE-OCT verbeterde de diepteresolutie van de zichtbare-golflengte lichtbron met kleine bandbreedte van 8 µm naar 1.5 µm. Door het signaal opnieuw te focussen en computationele aberratiecorrectie toe te passen wordt de DOF vergroot met een factor 20, wat resulteerde in een hoge 3D-resolutie over een groot volume.

Conventionele OCT-beeldvorming heeft een slechte specificiteit voor verschillende weefselstructuren aangezien het de structuur afbeeldt op basis van de verstrooiingseigenschappen. Deze zijn vrij gelijkaardig voor verschillende weefselstructuren. Daarom is het een uitdaging om plant pathogenen te onderscheiden van het omliggende weefsel waarin ze groeien, als alleen de morfologie in beeld wordt gebracht.

In hoofdstuk 5 hebben we de temporele fluctuatie van de OCT signaal amplitude gebruikt om contrast te creëren tussen pathogeen en plantenweefsel. Dynamische OCT (dOCT) gebruikt zowel de sterkte van het signaal als de tijdschaal van de fluctuaties hierin om een afbeelding in valse kleuren te maken met functioneel contrast van subcellulaire activiteit in verschillende weefsels. *Bremia lactucae*, een valse meeldauw in sla, geeft een sterke fluctuatie van de OCT amplitude bij middenfrequenties tussen 0.7 en 5.5 Hz, terwijl plantenweefsel een meer stationair signaal geeft bij een frequentie van 0 Hz. Dit verschil in het dynamische signaal wordt gebruikt om *Bremia* hyfen in een levend plantenblad af te beelden. Door de 3D-structuur van de pathogeen in de dOCT afbeeldingen te segmenteren, kwantificeerden we de mate van *Bremia*-infectie en zagen we een significant verschil in resistentie tussen verschillende sla-genotypes. Bovendien demonstreren we het *in-vivo* beeldvormingsvermogen van OCT door de voortgang van *Bremia*-infectie in de loop van drie tot vier dagen in beeld te brengen en de groeisnelheid van individuele hyfen te kwantificeren.

In het afsluitende hoofdstuk worden veelbelovende toekomstige richtingen voor de toepassing van OCT voor het beeldvorming van planten besproken. De toepassing van spectrale schatting OCT voor het verminderen van onderlinge fase verstoring in fasegevoelige OCT-beeldvorming wordt besproken met mogelijke toepassing in OCT-vibrometrie. Ook wordt 2D SE-OCT gepresenteerd voor de computationele verbetering van de laterale resolutie.

Dit proefschrift heeft de waarde aangetoond van OCT met hoge resolutie voor beeldvorming van planten met biologische relevantie. Dit werd bereikt door het toepassen van blad infiltratie voor het verbeteren van de beeldvormings diepte, spectrale schatting OCT voor het verbeteren van de resolutie en scherptediepte, en dynamische OCT voor het creëren van verbeterd contrast.

1

Introduction

1

1.1. Imaging in plant phenotyping

Vegetables and fruits constitute an indispensable part of human's daily nutrition. In the past centuries, agriculture has developed from small scale growing to large scale production on specialized farms. This development has increased efficiency and yield, allowing to feed the growing world population.

As the yield in agriculture is highly dependent on circumstances like weather, soil condition, and the presence of diseases, farmers have tried to control these circumstances by irrigation, fertilization, climate control in greenhouses and the use of pesticides. However, these techniques are not only expensive, but often also have detrimental effects to the environment and biodiversity. Irrigation, for example, exhausts water resources in times of drought, the use of artificial fertilizer increases the nitrogen deposit in nature resulting in biodiversity loss, and pesticides kill many organisms that are crucial to the ecosystem.

To complement these techniques and reduce their use, while maintaining or even increasing yield, plant breeders develop crop varieties that are better resistant against biotic stress, such as pathogens, and abiotic stress, such as drought and extreme temperatures. As environmental effects change and new pathogens develop there is a constant need for development of new varieties. Climate change and the resulting extreme weather makes this need even more urgent.

In pathogen resistance breeding, there is a constant race between plant breeders that develop resistant varieties and fast evolving pathogens that break the resistance. Until recently, most resistance breeding has largely been based on vertical resistance, where the resistance is based on a single gene and corresponding protein that makes the plant resistant to a specific disease. Horizontal resistance breeding, on the contrary, aims to improve the quality and robustness of the total immune system of the plant. The resulting resistance is not always complete, but the reduced susceptibility of a plant applies to a larger variety of diseases and is harder to break by the pathogens. As the development of horizontal resistance is gradual rather than binary, there is a need for objective, accurate and quantitative evaluation of the level of resistance of a variety [1–3].

Evaluation of plant performance, resulting from the combination of its genes and its environment, is called phenotyping [4, 5]. Besides resistance to disease, accurate and quantitative phenotyping is also crucial for developing crops with better drought resistance, higher yield, more appealing visual appearance and better taste. Since these improvements are often made in small steps, phenotype quantification is of paramount importance. While genetic technology has rapidly developed, a lot of the phenotyping is still done in a subjective and labour intensive way by visual scoring or measuring by hand. Thus, phenotyping is currently a bottleneck in effective plant breeding, since fast, automated, and accurate phenotyping technology has lagged behind [6, 7]. Digital imaging and image processing can be a major plant phenotyping method, as images can form the basis for accurate and quantitative description of the plant structure as well as function.

1.1.1. Plant imaging methods

In the imaging process, information from the sample is obtained through interaction of waves with the sample, which then brings the information to the detector. Different imaging approaches make use of different wave types, such as electron waves (electron microscopy), electromagnetic waves (X-ray, optics, MRI) or mechanical waves (ultrasound). Through scattering, transmission, reflection, emission, and/or fluorescence, information about the structure or function of the plant can be obtained.

The kind of structural or functional properties of the sample that can be imaged is dependent on the type of waves, the characteristics of the tissue interaction and the imaging method. Besides the type of contrast, the performance of the different imaging methods also differs in terms of resolution, imaging depth, and imaging speed. Moreover, some of of the imaging methods allow for non-invasive, in-vivo imaging while other methods need destructive sample preparation. All these factors have to be taken into account when an imaging modality is applied to investigate particular plant phenotypes.

Common functional optical plant imaging methods are (hyper-) spectral imaging [8, 9], thermal imaging [10, 11] and fluorescence imaging [12]. Spectral imaging measures the spectral reflectance or transmittance of plants, which can be an indication of the plant's condition. Also the plants temperature, measured with thermal imaging, reveals information of the plants response to, for example, drought. Fluorescence imaging can give valuable information on the condition of the photosynthesis (chlorophyll fluorescence imaging) [12] or the presence of metabolic compounds that are formed in stress responses [13]. These three methods are sensitive to the function and chemical composition of the plants.

Morphological imaging does not directly probe the function or chemical composition of plants, but instead measures their structure in 2D or 3D. Quantitative analysis of the structural images can give information that can be related to genes and the environment. 2D imaging with conventional cameras can give basic structural information, but as a plant is a 3D object, 3D imaging techniques give more precise information. The most common way to obtain the 3D structure is by obtaining distance maps through light detection and ranging (LIDAR), laser scanning, and stereo vision [14, 15]. LIDAR measures the time-of-flight of light reflected by the plant and can be used for single plants [16] up to measuring canopy height with airplanes or drones [17]. Laser scanning can be based on time-of-flight measurement (similar to LIDAR) or triangulation. With triangulation, a laser spot, line or other structure is projected on the object and moved. From the motion and deformation of these structures, captured by a 2D camera, the 3D structure of the object is reconstructed [15]. Stereo vision uses 2D images from different angles to reconstruct the 3D plant structure [18]. LIDAR, laser-scanning and stereo vision can only image the external structure of the plant, most often at the whole plant level.

Tomographic methods like micro-CT [19] and micro-MRI [20] and PET [21] provide 3D imaging of both the external and the internal plant morphology or localized functionality at whole plant or organ scale with resolutions of typical 100 µm and up

to 10 µm. These three tomographic methods have a useful place in plant science, but their application is limited because they require access from all sides, and are relatively expensive and slow. Moreover, they work with ionizing radiation (CT), radioactive isotopes (PET) or strong magnetic fields (MRI), which requires special precautions.

Smaller scale microscopic imaging of plants can be applied to study the more fundamental plant processes at cellular level, such as microscopic growth, organ initiation, and interaction with pathogens [22]. The main imaging modality for studies at the millimeter to cellular level is optical microscopy [23], either based on fluorescence, absorption, scattering or refractive index contrast.

In this thesis, we will focus on optical imaging of plants at microscopic scale, ranging from sub-cellular scale to parts of plant organs, such as leafs or roots. In the following section we will discuss microscopic optical imaging theory and its application to plant imaging. We will identify challenges with the standard microscopic techniques, when it comes to application to plant imaging. Optical coherence tomography (OCT) is a relatively new imaging technique that can be applied to plant imaging. This technique will be discussed in the third section of this chapter, and will be the technique central in this thesis.

1.2. Microscopic optical imaging

In optical imaging electromagnetic waves transfer the spatial information of the object, on the one side, to the detector at the other side, which is for example a camera or a retina. The light waves travel through an imaging system which usually consist of lenses and mirrors that focus and steer the light waves in order to obtain a sharp image on the detector. In this section we explain the basis of light wave propagation, different microscopic imaging systems and their strengths and limitations when applied to plant imaging. At the end we indicate how OCT can perform better on some of these limitations.

1.2.1. Diffraction and resolution

Figure 1.1 shows one of the most basic optical imaging systems: the 4-f system. Light from the object is captured by an objective lens and then imaged on the detector by a tube lens. In geometrical optics, light is assumed to travel along straight rays such that a point in the object corresponds to a point at the detector. In reality, light is a spherically propagating wave that diffracts around edges. Thus, even for a perfectly designed imaging system, a point in the object becomes a blurred spot at the detector, as shown in Fig. 1.1. This blurred spot is called the point spread function (PSF), and is one of the most important parameters to characterize an imaging system.

When two points in the image are closer to each other than the width of the PSF, their blurred spots will overlap and they cannot be distinguished. Thus, the width of the PSF is an indication of the smallest details from the object that can be visualized in the image, also called its optical resolution. According to the Rayleigh criterion two points of the object are just distinguishable when their relative distance is at

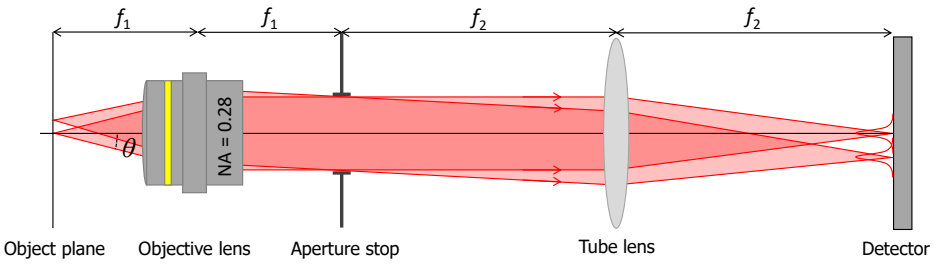

Figure 1.1: A 4-f imaging system.

least the radius of the first dark ring of the Airy pattern [24, p.157], which is the PSF resulting from a circular aperture with uniform illumination. The radius of this dark ring is [24, p.77]

$$r = 0.61\frac{\lambda}{\mathrm{NA}}, \tag{1.1}$$

where λ is the wavelength of the light and NA is the numerical aperture of the imaging system, defined as

$$\mathrm{NA} = n \cdot \sin\theta, \tag{1.2}$$

where n is the refractive index of the medium and θ the half opening angle as shown in Fig. 1.1. Thus the NA of an imaging system, together with the wavelength, determines the smallest lateral details that can be distinguished in a system that is limited by diffraction.

1.2.2. Wide field microscopy

Figure 1.2(a) shows a schematic overview of a widefield microscope. In widefield microscopy the sample is uniformly illuminated (from either the top or the bottom) and the image formation takes place in the receiving light path. The reflected, emitted fluorescence or transmitted light from the whole field of view (FOV) of the object is captured simultaneously by the objective lens and projected on the camera by the tube lens. The lateral PSF of a diffraction limited wide-field microscope is an Airy disc with the radius of the first dark ring given by Eq. 1.1.

When the imaged sample extends outside the focal depth region (which is typically in the order of 10-30 µm), the blurred signal from these regions is also captured on the camera, which gives a large background signal that reduces the contrast. This is especially prevalent in highly scattering samples or samples with a large background fluorescence. Together with the limited axial resolution, this contrast reduction makes wide-field microscopy not well suitable for 3D imaging. Thicker samples need to be fixated and sliced in thin layers to obtain good quality images.

Plant imaging with wide-field microscopy

Widefield microscopy is extensively applied for plant imaging. Brightfield microscopy, where transmitted light is captured and differences in absorption or scattering are used as contrast mechanism, is often used in combination with optical clearing and

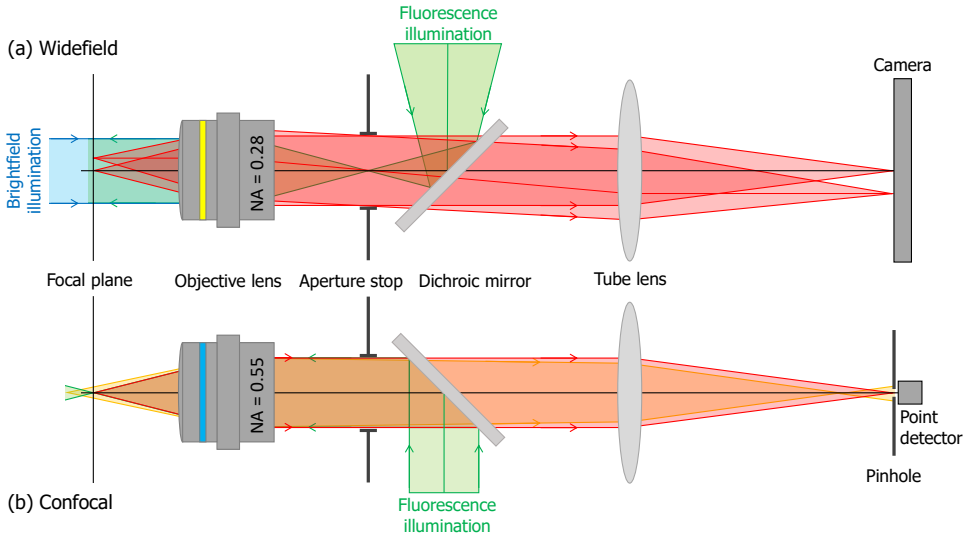

Figure 1.2: Illustrations of (a) a widefield and (b) a confocal microscope. The fluorescence illumination paths are indicated in green, the brightfield illumination path is indicated in blue and the detection paths are indicated in red. The orange illumination path in (b) indicates out-of-focus fluorescence that is partially blocked by the point detector.

staining of the structures of interest. For example, Trypan blue staining with clearing can be used to image downy mildew inside lettuce leaves [25]. Physically slicing is another strategy to reduce the scattering background and obtain clear widefield images from within the tissue. Without clearing or slicing, only the epidermal cells and stomata at the surface can be visualized in 2D.

Also widefield fluorescence microscopy is widely used for microscopic plant imaging, as it has a high contrast between fluorescence and background. Using genetic transformations, specific features can be made to express fluorescent proteins that allow for imaging these labeled structures [26, 27]. Without genetic transformation, less specific auto-fluorescence of for example chloroplasts can be utilized [28], or the sample can be labeled with fluorescent markers that chemically bind to a target compound [29]. Widefield fluorescence microscopy also suffers from a high background signal, including signal from auto-fluorescence and signal from scattering when a thick sample is used, and is not well suitable for 3D imaging.

1.2.3. Confocal microscopy

Confocal microscopy (CM) strongly reduces the background signal and improves the axial resolution compared to widefield microscopy [30]. Figure 1.2(b) shows a schematic image of a confocal microscope. In CM, the illumination beam is focused on the sample and the illuminated spot is imaged back on a point detector. The focused illumination spot has the same shape as the wide-field PSF. However, this spot is imaged in collection and sampled with a pinhole before the detector, which gives a lateral PSF that is equal to the square of the wide-field PSF. Hence, the

resolution improves by a factor $\sqrt{2}$. Moreover, the pinhole that is placed before the detector, blocks most of the blurred light from the out-of-focus regions (the orange path in Figure 1.2(b)), while it lets the light from the focus point pass through. This leads to a strong contrast enhancement. Since the beam is scanned in lateral directions to obtain an image over the whole sample, CM requires a more advanced setup and larger imaging time than wide-field microscopy.

The ability to select the signal only from the depth of field and suppress signal from other depths is called optical sectioning. This allows for 3D imaging without physically slicing the sample, even when imaging a scattering sample. Usually a volume image is created as a stack of en-face images by moving the sample in the axial direction with an accurate translation stage.

While CM is most commonly based on fluorescence, it is also applied in a reflection configuration, but at the cost of a smaller optical sectioning ability due to coherence between illuminated and reflected light.

Plant imaging with confocal microscopy

Fluorescence-based CM is a widely used approach for optical 3D imaging of plants at sub-cellular resolution [31]. As non-destructive imaging method, it can image *in-vivo*, allowing for imaging of plant processes like root growth and plant-pathogen interaction over time [32]. The typical maximum imaging depth with confocal microscopy in uncleared plant tissue is 60-80 µm [33]. For imaging deeper into the plant tissue or reduce image degradation, the plant tissue can be made transparent using different optical clearing protocols [33, 34] that can be combined with staining using fluorescent labels [35]. A point of attention for confocal microscopy is the high illumination intensity at the focal spot. While a high light intensity leads to a better fluorescence signal, it may result in phototoxicity, leading to the formation of substances that affect the living organisms biochemistry [36], and can cause photo bleaching, leading to a decrease of fluorescence. Thus, especially for *in-vivo* imaging, the illumination intensity needs to be limited.

Generalization of selective fluorescence excitation

CM applies local illumination to reduce background signal and increase the resolution. This concept can be extended to other selective illumination approaches, for example light sheet fluorescence microscopy (LSFM). In LSFM, the sample is illuminated with a light sheet from the direction perpendicular to the collection path [37, 38]. This allows for optical sectioning and background fluorescence reduction in combination with simultaneously imaging the whole lateral field of view in a wide-field collection configuration. LSFM has been used for 3D imaging of plant organs with cellular resolution [39]. However, it requires a good access to the sample from all sides both to generate a good light sheet for illumination and to collect the fluorescence. In addition, it also suffers from scattering in tissue.

1.2.4. Limitations of optical microscopy for plant imaging

Though optical microscopy successfully has been applied in many plant imaging applications, there are still significant limitations. First, the highly scattering plant

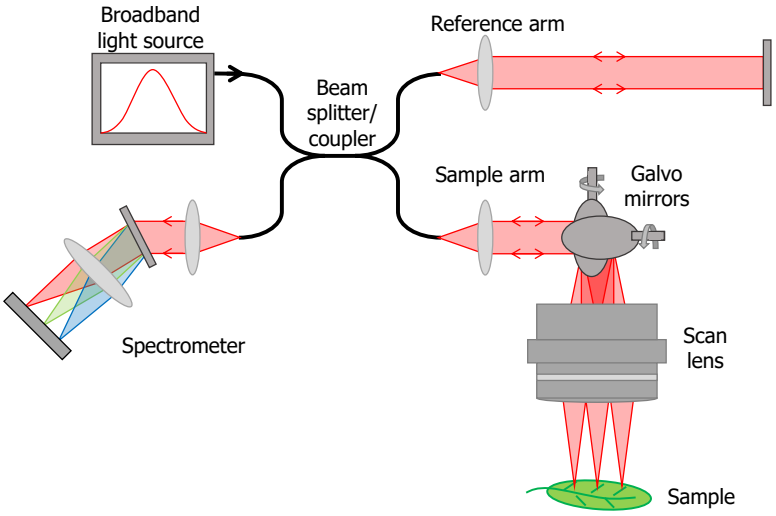

Figure 1.3: Schematic overview of a spectral-domain OCT setup.

tissue limits the imaging depth in non-cleared tissue. Second, many techniques depend on (fluorescence) labeling, which is not always available nor desired. Third, optical microscopy has limited optical sectioning abilities, especially in absence of fluorescence, which hampers its 3D imaging capability. The next section discusses optical coherence tomography and how some of these limitations can be addressed with this imaging technique.

1.3. Optical coherence tomography

Optical coherence tomography (OCT) uses interference of broadband light to measure travel distance of reflected light from the sample to create optical sectioning. When the optical beam is scanned in the lateral direction over the sample, a 2D or 3D image of the reflecting structures can be obtained. OCT was first introduced in a time-domain implementation in 1991 [40]. Its development has accelerated after the introduction of Fourier domain OCT (FD-OCT) with its superior sensitivity [41, 42]. Fourier-domain OCT has become the standard imaging modality in ophthalmology, and has also found its way to other fields such as cultural heritage imaging [43] and plant imaging [44, 45].

This section gives a short introduction to OCT theory, followed by two subsections on axial resolution and the trade-off between lateral resolution and depth-of-focus (DOF), topics that are further developed in this thesis.

1.3.1. OCT theory

Figure 1.3 gives a schematic overview of a spectral-domain OCT (SD-OCT) setup. Light from a broadband light source is split into a reference arm and a sample arm. After reflecting on the reference mirror and the sample respectively, the light is

recombined and interferes on a spectrometer.

The light field from the reference arm can be described as

$$E_r = \sqrt{S_0(k)} a_r \mathrm{e}^{2iz_r k}, \tag{1.3}$$

where $S_0(k)$ is the source spectral density as function of wavenumber k, i is the complex number, a_r is the reference arm reflectivity and z_r is the reference arm length. Note that for simplicity the splitting ratio of the beamsplitter is omitted. The field from the sample arm reflects at multiple depths in the sample, and can thus be described as

$$E_s = \sqrt{S_0(k)} \int a(z_s) \mathrm{e}^{2iz_s k} \mathrm{d}z_s, \tag{1.4}$$

where $a(z_s)$ is the reflectance as function of depth z_s in the sample. Note that depth z_s is measured in optical path length (OPL), being the integral of the refractive index over depth. In the rest of the theory, this dependency on the refractive index is implicitly assumed.

The detected light intensity combines these fields as

$$I_D(k) = |E_r + E_s|^2 = |E_r|^2 + |E_s|^2 + E_r E_s^* + E_r^* E_s. \tag{1.5}$$

The first term $|E_r|^2$ is a constant reference signal with the source shape, also called the direct current (DC) term as it does not contain interference information. This term can easily be subtracted. The second term, $|E_s|^2$, is the auto-correlation signal, the interference of the signal from the sample with itself. When the sample reflectivity is much lower than the reference arm reflectivity, which is the case for OCT imaging of tissue, this term is relatively small and is only relevant for small path length differences. Hence this term can be separated from the last two terms in the reconstruction by putting the sample at a small offset from the zero delay. The last two cross-interference terms are the signal of interest for OCT. Using eqs. 1.3 and 1.4, the interference signal can be written as

$$I(k) = E_r E_s^* + E_r^* E_s = S_0(k) a_r \int a(z_s) \cos(2(z_s - z_r)k) \mathrm{d}z_s. \tag{1.6}$$

Omitting the constant reference arm reflectivity, defining $z = z_s - z_r$ as new depth coordinate system and $\tilde{z} = 2z$ as the double pass path length difference between the sample and reference arm, equation 1.6 can be rewritten to the product of the source intensity and the inverse Fourier transform of combined reflectivity $\tilde{a}\left(\frac{\tilde{z}}{2}\right)$:

$$I(k) = S_0(k) \int \tilde{a}\left(\frac{\tilde{z}}{2}\right) \mathrm{e}^{-i\tilde{z}k} \mathrm{d}\tilde{z}, \tag{1.7}$$

where

$$\tilde{a}\left(\frac{\tilde{z}}{2}\right) = \tilde{a}(z) = a(z) + a^*(-z) \tag{1.8}$$

is the combination of the reflectivity and the mirrored complex conjugate of the reflectivity. Thus the reflectivity $\tilde{a}(z)$ of the sample is encoded as frequency in the

wavenumber domain and can be estimated by taking the inverse Fourier transform of $I(k)$. The estimated reflectivity $\hat{a}\left(\frac{\tilde{z}}{2}\right)$ becomes

$$\hat{a}\left(\frac{\tilde{z}}{2}\right) = \mathcal{F}^{-1}\{I(k)\} = \mathcal{F}^{-1}\{S_0(k)\}(\tilde{z}) * \tilde{a}\left(\frac{\tilde{z}}{2}\right), \tag{1.9}$$

where $\mathcal{F}^{-1}$ denotes the inverse Fourier transform and $*$ denotes a convolution.

In reality, $I(k)$ is measured for discrete wavenumbers k_n and the inverse Fourier transform is normally done by an inverse discrete Fourier transform (DFT). Moreover, as most spectrometers do not have a uniform sampling in wavenumber space, the interference signal needs to be interpolated to be able to use the fast Fourier transform (FFT). Discrete sampling of the interference signal limits the absolute path length difference between reference and sample arm z that can be measured. Using the Nyquist criterion and the relation $\tilde{z} = 2z$, we obtain a maximum imaging depth

$$z_{max} = \frac{\tilde{z}_{max}}{2} = \frac{\pi}{2\delta k}, \tag{1.10}$$

with δk the wavenumber sampling step size.

1.3.2. Axial resolution in OCT

Equation 1.9 shows that the estimated reflectance is a convolution of the inverse Fourier transform of the source spectrum, also indicated by γ, with the combined reflectivity $\tilde{a}\left(\frac{\tilde{z}}{2}\right)$. The inverse Fourier transform of a Gaussian source spectrum with a full-width at half maximum (FWHM) of Δk is

$$\gamma(z) = \mathcal{F}^{-1}\left\{I_0 \mathrm{e}^{-\frac{4\ln 2(k-k_c)^2}{\Delta k^2}}\right\}(\tilde{z})\Big|_{\tilde{z}=2z} = \frac{I_0 \Delta k \mathrm{e}^{i2zk_c}}{4\sqrt{\pi \ln 2}} \mathrm{e}^{-\frac{\Delta k^2 z^2}{4\ln 2}}. \tag{1.11}$$

The FWHM of $\gamma(z)$ is also called the round trip coherence length l_c of the source, and can, for the Gaussian source spectrum, be expressed as

$$l_c = \frac{4\ln 2}{\Delta k} \approx \frac{2\ln 2}{\pi}\frac{\lambda_c^2}{\Delta\lambda}, \tag{1.12}$$

where $\lambda_c = 2\pi/k_c$ is the center wavelength and $\Delta\lambda$ the FWHM of the corresponding wavelength spectrum.

A close look at Eq. 1.9 shows that $\gamma(z)$ acts as an axial PSF for the complex field reflectance, making the coherence length a measure for the axial resolution. Sometimes, the PSF based on reflectance intensity $i(z) = \left|\hat{a}(z)\right|^2$ is used as measure for the axial resolution, which is a factor $\sqrt{2}$ narrower. Equation 1.12 clearly shows the inverse relationship between source bandwidth and coherence length. The main method to improve the axial resolution has been to extend the source bandwidth or reduce the source center wavelength λ_c. However, when that is difficult, due to limited source availability or design purposes, computational methods can be used to obtain a higher resolution with a limited source bandwidth.

Computational methods for improving axial resolution

Various computational methods for improving the axial resolution have been proposed: spectral reshaping [46], deconvolution [47], and sparsity-based optimization methods [48, 49].

For spectral reshaping the interference signal $I(k)$ is divided by the source spectrum $S_0(k)$ and multiplied by the desired spectral shape. This shapes the axial PSF, as it is determined by the inverse DFT of the chosen spectral shape. For non-smooth spectral source shapes, spectral reshaping to a smooth window, such as a Gaussian or Hanning window, is often applied to obtain a smooth, symmetric PSF with low side-lobes [50]. Reshaping to a wide window, such as a rectangular or crater-like window [46], reduces the FWHM of the PSF at the cost of increasing side-lobes. However, when low-SNR edges of the spectrum are amplified, the SNR of the OCT image may decrease.

Deconvolution is a method to undo the distortion of the image caused by the convolution of the imaged object with the PSF. Using the known or estimated PSF shape, the blurring effect on the image can be reduced by the implementation of deconvolution algorithms. To avoid noise enhancement, some regularization needs to be applied to yield an optimal image. One of the most successful deconvolution approaches for axial resolution enhancement in OCT is the iterative Lucy-Richardson deconvolution [51].

Instead of using the DFT (equivalent to Eq. 1.9), the reflectivity $\tilde{a}(z)$ of the sample can be estimated using other inversion approaches. These methods improve the resolution by adding a sparsity promoting regularization [49] or by using a parametric model [52]. They avoid certain drawbacks of the DFT method, such as periodic boundary conditions and spectral leakage [53]. Many of these methods borrow from the spectral estimation methods from the field of signal processing, since the reconstruction in FD-OCT is equivalent to a spectral estimation problem. In chapter 3 of this thesis we will explore one of such methods for improving the axial resolution.

1.3.3. Lateral resolution and depth of field

The axial and lateral resolution in OCT are largely decoupled. While the axial resolution in OCT is based on the interference of broadband light, the lateral resolution is determined by the optics that focuses the beam on the sample.

The optical setup of OCT is similar to that of a confocal microscope in reflection mode. With a single-mode optical fiber as the illumination source and pinhole, the lateral PSF will be Gaussian shaped. Taking the $1/e^2$ intensity as the aperture edge to calculate the NA of the system, the FWHM of the PSF in focus is

$$\mathrm{FWHM}_{xy} = \frac{\sqrt{2\ln 2}}{\pi}\frac{\lambda_c}{\mathrm{NA}} \approx 0.37\frac{\lambda_c}{\mathrm{NA}}. \tag{1.13}$$

Although a high lateral resolution is preferred, it reduces the depth of field (DOF), the axial depth range in which the width of the focused beam is close to its width in focus. Since, Fourier-domain OCT simultaneously measures the signal for a large depth range the ideal beam for OCT would be a pencil beam with a very narrow

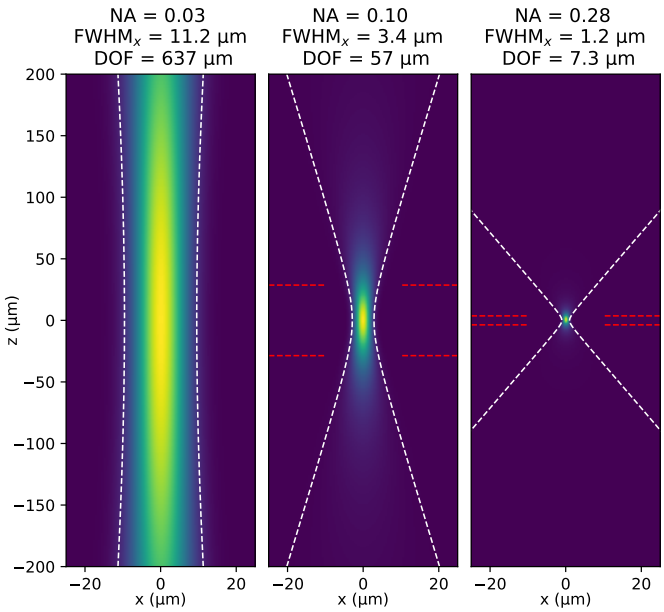

Figure 1.4: Plot of the lateral PSF for a Gaussian OCT beam focused at $z = 0$ for three different NAs and a center wavelength $\lambda_c = 900$ nm. The white dotted lines indicate the edge of the PSF, defined as the location where the intensity is $1/e^2$ of the intensity at the center ($x = 0$). The red-dotted lines indicate the edges of the depth-of-focus (DOF) in the right two images. In the left image the DOF extents to outside the displayed depth range. Note that the x and z axes have a different scale.

width. However, with conventional optics the beam diverges outside the focus plane. This widening of the beam is stronger with a high NA, as visible in Fig. 1.4, where Gaussian beams with different NAs are plotted around focus. Defining the DOF as the depth over which the PSF is smaller than $\sqrt{2}$ times the width in focus, we can express the DOF for a Gaussian beam as

$$\mathrm{DOF} = 2z_R = \frac{2\lambda_c}{\pi \mathrm{NA}^2}, \tag{1.14}$$

where z_R is the Rayleigh length of the Gaussian beam. Equation 1.14 and the plots in Fig. 1.4 explain why most OCT setups have a low NA in the order of 0.01-0.03, which is much lower than most (confocal) microscopes. A low NA makes it possible to acquire a sharp image over a large depth range at once, without having to move the sample or the optics.

Note that the DOF reduces quadratically with the NA, while the lateral resolution only increases linearly with the NA. While an NA of 0.03 gives a DOF than about 60 times the lateral resolution (Fig. 1.4 left), an NA of 0.28 reduces this to 6 times the lateral resolution. Increasing the resolution by decreasing the OCT center wavelength, reduces the DOF only linearly. However, this is only partially possible, because scattering in tissue increases with smaller wavelengths and light

with wavelengths below that of the visible range are more harmful to biological tissue.

The trade-off between lateral resolution and DOF is a well known problem within OCT research and a lot of research efforts has been spent on extending the depth of field while maintaining a high lateral resolution. The methods for solving this can be split in to hardware-based approaches and computational approaches.

Hardware based approaches for extending the DOF

Hardware based DOF extension methods can be divided into two categories. The first method is engineering beams that are narrow over a larger axial range than a Gaussian beam with similar lateral resolution. The most well-known example is a Bessel beam [54, 55], which has a constant beam profile over a large depth range. However, for Bessel beams the DOF extension comes at the cost of transferring energy from the main lobe into side-lobes, which both reduce the SNR and introduce side-lobe artefacts in the PSF. Another example is wavefront shaping that focuses different rings of the aperture onto different depths. In effect, this is similar to introducing spherical aberrations [56]. This DOF extension comes at the cost of a reduced PSF width in focus and ringing artefacts.

The second class of hardware-based methods acquire multiple images, each focusing at a different depth. This can be done sequentially in time, for example by moving the sample [57] or using a tunable lens to vary the focal plane [58]. Another approach is by giving each focal distance a distinct optical path length offset, such that the images can be acquired simultaneously and combined in the reconstruction [59, 60]. The first method requires more acquisition time, while the second approach requires a dense k-sampling for sufficient imaging depth to separate the images. In both cases, the acquired images need to be stitched together in post-processing to obtain a high resolution image over a large DOF.

Computational methods for extended depth of field

The depth of field can also be extended computationally after acquisition [61]. Amplitude or intensity based deconvolution using a depth dependent defocused PSF has been used to sharpen the image outside focus [47]. This approach is often combined with axial deconvolution. Because these deconvolution methods neglect the phase information, they do not give good results for closely separated scatterers whose coherent fields interfere with each other. Thus they mainly improve image sharpness, and are less able to resolve dense structures in the sample [61]. To achieve that, we have to turn to methods that use the complex field.

One such method to extend the DOF is propagating the complex field of an out-of-focus en-face plane to focus using scalar diffraction theory [61, 62]. Propagation can be implemented by Fresnel propagation or using the angular spectrum method. It also can be done by multiplying the 2D Fourier transform of the en-face image with a complex exponential with a parabolic phase that effectively eliminates the defocus aberration and results in a sharply focused image. While this method yields good results, it has to be applied plane by plane, each having a different defocus factor, which requires a lot of computations. Moreover, signals that end up

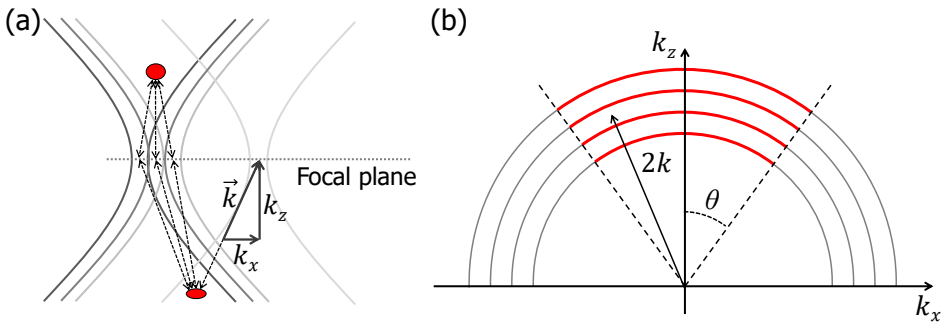

Figure 1.5: Schematic overview over interferometric synthetic aperture microscopy. (a) The back and forth propagation path between a scatterer (red) and the focal point of laterally shifted beams. The scattering vector $\vec{k}$ consists of an x and y component. (b) Graphical illustration of the spatial frequencies k_x and k_z that are captured from the object. Red arcs correspond to a constant wavenumber $2k$, with the factor 2 accounting for the round trip. Note that this figure shows a 2D cross-section of a 3D geometry, with the geometry in the out-of-plan direction (k_y) being the same as the geometry in the k_x direction. Thus the the arcs are in reality parts of the Ewald sphere.

in another en-face plane because of the wavefront curvature outside focus cannot be focused correctly using this method [61].

Interferometric synthetic aperture microscopy (ISAM) views OCT imaging as an inverse scattering problem [61, 63]. This problem can be solved by a resampling in the Fourier domain, a method that originates from the field of seismic imaging [64]. In ISAM, a synthetic aperture is placed in focus, and the scattered light can be considered as traveling back and forth along the same straight path from the focal point to the scatterer, as visualized in Fig. 1.5(a). The wavenumber of the scattered light has both a depth (z) component and a lateral (in the figure x) component. The lateral location of the focus determines what lateral component of the wavenumber is obtained for the scatterer in Figure 1.5(a). Taking the 3D Fourier transform of the complex OCT field, after shifting the focus to $z = 0$, allows to obtain the field in k-space, as function of the scattering wavenumbers k_x and k_y. However, in the axial direction the wavefield is recorded as function of total wavenumber k rather than k_z. Thus the recorded scattering wavenumbers lie on the red arcs in Figure 1.5(b), rather than on straight, horizontal lines. Now, using the lateral wavenumbers, the signal along these arcs in the k-space can be reassigned to the proper k_z values:

$$k_z = \sqrt{(2k)^2 - k_x^2 - k_y^2}, \tag{1.15}$$

where the factor 2 in front of k is to account for the back-scattering geometry. With a small NA, the opening angle is small, thus the arcs can be approximated by straight lines. However, when the the NA (and thus θ) increases, this approximation is invalid. With ISAM, the recorded field is placed at its proper place in the frequency domain using an interpolation to a linear grid in k_z, as determined by Eq. 1.15. The ISAM refocused field with diffraction limited resolution can be obtained by a 3D inverse Fourier transform of the resampled data.

As both refocusing and ISAM are based on coherent interference of fields from different scan lines, these methods require the signals from different scan lines to be phase stable [61, 63, 65]. The most common sources of unstable phase are drift in the sample or reference arm, jitter in the scanning system, and sample motion during acquisition. Fast acquisition and sample fixation can reduce phase instability [66]. However, phase stability can also be obtained computationally, using the phase from a reference interface on top of the sample, for example that from a coverslip [63], or by estimating bulk phase shifts from correlating neighbouring scan lines [67].

While with refocusing and ISAM, the DOF is not limited anymore by the beam shape, there are still limits to the depth range where these methods can be successfully applied. First, the phase stability requirement needs to be fulfilled over a large lateral FOV for signal far from the focal plane. Second, the SNR outside the focal region decreases significantly because the confocal gate suppresses scattering signal from outside the focal plane [63, 68]. While the coherent combination of the signal from multiple scan lines increases the signal intensity outside the focal plane, it does not reach the same level as the signal at the focal plane. Despite the limitation from phase stability and decreasing SNR, the DOF can be extended by more than an order of magnitude [61, 66].

1.3.4. Challenges for plant imaging with microscopy and OCT

While OCT naturally addresses some of the limitations of wide-field and confocal microscopy as mentioned in subsection 1.2.4, other limitations are still present to some degree. In this section we discuss three important challenges that will be addressed in this thesis: improving the imaging depth in the presence of scattering, obtaining a high resolution in 3D, including the need for optical sectioning, and reducing the dependency on (fluorescence) labels. Though we focus on plant imaging, the mentioned challenges are also present when imaging other (biological) samples.

Imaging deep in scattering tissue

One of the major drawbacks of microscopy is the limited imaging depth in plant tissue due to light scattering. Especially in leaves and other tissue with cavities that are filled with gas [33], light scattering is very strong due to the large contrast in refractive index between air and tissue. Although some amount of light scattering is required to obtain scattering contrast, it reduces the direct light intensity from deeper imaged structures, and gives rise to a diffuse background signal that does not contain direct information from the sample. Thus, scattering reduces the signal to background ratio, and thus the effective imaging depth. As the background signal is not suppressed in wide-field microscopy, this method has a very shallow penetration depth of typical a few tens of micrometer. With the confocal gate, that suppresses out-of-focus background signal, CM can go deeper up to about 60-80 µm in plant tissue [33]. Imaging deeper inside plant tissue requires either physically slicing or optical clearing of the tissue. These methods are not only incompatible with *in-vivo* imaging, they also require labour-intensive sample preparation follow-

ing detailed protocols.

Point-scanning OCT can image deeper into scattering media than confocal microscopy. Similar to confocal microscopy, it uses a confocal gating to suppress diffuse scattering light outside the focal area. In addition, OCT uses interference gating to measure the travel distance of the scattered light. Light that scatters multiple times has a larger path length and will end up deeper inside the image. Thus, especially the part of the image close to the surface will suffer less from diffuse scattering light. However, the gas-filled cavities inside the leaves still strongly reduce the imaging depth, causing a haze of multiple scattered light that occludes the image of deeper regions. Moreover, refraction and variation of OPL due to strong variation in refractive index causes further distortion of deeper leaf structures in the OCT image. These effects together reduce the imaging depth in plant tissue to about two to three cell layers, up to about 100-140 µm.

The effect of the gas-filled pockets on the imaging depth can be reduced by filling these pockets with a liquid that has refractive index close to that of leaf tissue, such as perfluorcarbons [69] or water [33]. As it reduces the contrast in refractive index of the tissue, it can be called an optical clearing method, though it is less aggressive than most clearing methods and compatible with *in-vivo* imaging. Filling the cavities with perfluorcarbons resulted in an increased imaging depth up to 100-135 µm with confocal microscopy [69].

Obtaining a high resolution in 3D

One of the main goals of microscopic plant imaging is to study morphology and interaction at the cellular level. While most optical microscopy setups have a sufficiently high lateral resolution, in the order of 500 nm to 2 µm, the axial resolution is a lot worse. To be able to image in 3D, the imaging method needs to have a good optical sectioning ability. As we have seen, widefield microscopy has a very limited sectioning ability, making it merely a 2D imaging method. CM has a better optical sectioning ability and can thus be used for optical 3D imaging at cellular level. However, for CM the sectioning ability is mainly achieved with a high NA, which is more prone to optical aberrations. Moreover, such a high lateral resolution is not always needed as it reduces the lateral field of view and the imaging speed. LSFM obtains optical sectioning from the illumination with a light sheet. This is a promising technique for microscopic 3D imaging, but requires access to the sample from the side. Moreover, LSFM and most CM need fluorescence labeling.

OCT uses broadband light interference to create optical sectioning allowing for a high axial resolution also with a low NA. With typical lateral resolutions of 5-20 µm, it performs significantly worse than that of optical microscopy. To visualize cells, small pathogen structures and subtle changes in the plant tissue, a higher resolution of about 1-3 µm is needed. This can be obtained by using shorter light wavelengths in the visible range and a higher NA together with depth of field extension. Computational methods as discussed above may give an additional improvement in resolution.

When using a higher NA, optical aberrations, i.e., the deviation from the spherically focused wavefront, become more prevalent. They cause the PSF to broaden,

transfer power from the main lobe to the side-lobes, or cause additional ringing artifacts around the PSF [24, p.145-151]. Aberrations can be caused by non-ideal lenses, poor optical design, or by inhomogeneity of the sample, the latter being the hardest to correct. In contrast to widefield and confocal microscopy, OCT gives the complex wavefield that can be used for computational aberration correction. Using a method similar to refocusing, but now also including other aberrations than defocus, much of the aberrations can be eliminated [70]. Yet, the aberration first needs to be estimated, which can be done by, for example, optimization of the image with an image-sharpness metric [70], using a guide star [71], or cross-correlating subapertures [72].

Label-free imaging with sufficient contrast

For *in-vivo* or minimal invasive microscopic plant imaging, there is an increasing demand for label-free imaging methods. Label-free means that the imaging is done without relying on an artificially added label, whether it is a chemical compound that binds to the structures of interest or a genetically expressed label in a transgenic plant or pathogen. Label free methods rely, for example, on (wavelength dependent) scattering, transmission, refractive index differences, or autofluorescence properties of the natural plant tissue.

Fluorescence CM and LSFM need fluorescence in the target structures. Because autofluorescence is not specific and is not present in all structures of interest, these imaging techniques often use fluorescent labeling. While labeling allows for a high level of specificity, *in-vivo* fluorescence labeling is not always possible or wanted. Genetically transformed plant varieties that express targeted fluorescence are very limited available, especially for varieties that are not model plants systems such as *Arabidopsis*. Fluorescence labeling with chemical compounds is often destructive and requires long and labour-intensive sample preparation. The same is true for labeling with absorptive stains, such as Tryphan blue, which is usually combined with optical clearing. Thus, there is a clear need for label free imaging.

OCT is a label-free imaging method based on scatterring from refractive index differences in the medium and does not rely on fluorescence or absorptive stains. However, OCT's contrast mechanism also introduces extra challenges as all structures that scatter will be imaged, making OCT imaging rather unspecific. This makes it harder to target specific structures or distinguish well between, for example, plant cells and pathogen structure. Segmentation based on morphology can help in this process, but segmentation of 3D data is challenging and requires good quality data. Hence, OCT imaging of plants focuses more on bulk leaf properties, such as cell layer thickness over a laterally averaged B-scan [73] or attenuation coefficient [74].

In the biomedical OCT imaging field, some promising methods for obtaining functional contrast have been developed that may be applicable to plant imaging. Most of these methods somehow exploit the change in signal over time when the imaged tissue moves. These methods include quantification of flow speed with Doppler [75] and dynamic light scattering [76] OCT, blood vessel and flow channel visualization with optical coherence angiography (OCA) [77], and pixel-level frequency of motion contrast to create contrast based on the time-scale of cellular dynamics [78]. With spectroscopic OCT, the reflected OCT signal is split into

smaller spectral bands, enabling 3D multi-spectral imaging at microscopic scale at the expense of a reduced axial resolution [79, 80].

Few of these methods have yet been applied to plant imaging. The most noteworthy example is biospeckle imaging [81, 82], which, similar to OCA, uses the variance of the speckle signal in time as contrast mechanism. However, it has mainly been limited to average biospeckle signal over a large area, rather than to create contrast within an image. There is still a high potential of the other functional imaging methods to improve specificity in plant imaging, especially if it would enable quantification of physical properties of the plant that are not setup dependent.

1.4. Thesis outline

In this thesis we address imaging challenges for OCT applied to microscopic plant imaging. In this way we make OCT better suited for plant phenotyping.

In chapter 2 we address the problem of the limited imaging depth caused by high scattering from gas filled cavities. We significantly increase the imaging depth in plant leaves by infiltrating them with water. We extent the imaging depth from about 100-150 µm to the entire leaf cross-section of up to 300 µm. Moreover, we quantify plant leaf refractive index and local leaf thickness.

Chapter 3 presents a computational method to improve the axial resolution in OCT using the iterative adaptive approach (IAA). We show a factor 2.7 improvement in the axial resolution in experimental data and up to a factor 10 for high SNR simulation data. This can be used as building block to obtain a higher 3D resolution for plant imaging with visible light OCT.

Chapter 4 discusses a high resolution OCT setup with a superluminescent diode in the visible light range that has a relatively low bandwidth. Combining the method that was developed in chapter 3 to improve the axial resolution with ISAM and computational aberration correction for lateral resolution improvement, we obtain single micrometer 3D resolution over a depth range that is much larger than the original DOF. We apply this setup and method to perform high resolution 3D imaging of plant tissue.

Chapter 5 applies dynamic OCT imaging, which is based on the temporal frequency of the signal, to create label-free high contrast 3D images of plant tissue. We demonstrate label-free visualization of downy mildew, a pathogen in lettuce, at tissue level in 3D.

Chapter 6 concludes this thesis, discusses the contributions of this thesis to microscopic imaging of plants using OCT, and gives an outlook on promising directions for further development of this field.

References

[1] J. A. Corwin and D. J. Kliebenstein, *Quantitative resistance: more than just perception of a pathogen,* The Plant Cell **29**, 655 (2017).

[2] R. Nelson, T. Wiesner-Hanks, R. Wisser, and P. Balint-Kurti, *Navigating com-*

plexity to breed disease-resistant crops, Nature Reviews Genetics **19**, 21 (2018).

[3] M. Gou, P. Balint-Kurti, M. Xu, and Q. Yang, *Quantitative disease resistance: Multifaceted players in plant defense,* Journal of Integrative Plant Biology **65**, 594 (2023).

[4] D. Houle, D. R. Govindaraju, and S. Omholt, *Phenomics: the next challenge,* Nature Reviews Genetics **11**, 855 (2010).

[5] M. Minervini, H. Scharr, and S. A. Tsaftaris, *Image analysis: the new bottleneck in plant phenotyping [applications corner],* IEEE Signal Processing Magazine **32**, 126 (2015).

[6] R. T. Furbank and M. Tester, *Phenomics–technologies to relieve the phenotyping bottleneck,* Trends in Plant Science **16**, 635 (2011).

[7] F. Fiorani and U. Schurr, *Future scenarios for plant phenotyping,* Annual Review of Plant Biology **64**, 267 (2013).

[8] S. Thomas, M. T. Kuska, D. Bohnenkamp, A. Brugger, E. Alisaac, M. Wahabzada, J. Behmann, and A.-K. Mahlein, *Benefits of hyperspectral imaging for plant disease detection and plant protection: a technical perspective,* Journal of Plant Diseases and Protection **125**, 5 (2018).

[9] M. Kuska and A.-K. Mahlein, *Aiming at decision making in plant disease protection and phenotyping by the use of optical sensors,* European Journal of Plant Pathology **152**, 987 (2018).

[10] F. Fiorani, U. Rascher, S. Jahnke, and U. Schurr, *Imaging plants dynamics in heterogenic environments,* Current Opinion in Biotechnology **23**, 227 (2012).

[11] L. Li, Q. Zhang, and D. Huang, *A review of imaging techniques for plant phenotyping,* Sensors **14**, 20078 (2014).

[12] E. H. Murchie and T. Lawson, *Chlorophyll fluorescence analysis: a guide to good practice and understanding some new applications,* Journal of Experimental Botany **64**, 3983 (2013).

[13] E. Granum, M. L. Pérez-Bueno, C. E. Calderón, C. Ramos, A. de Vicente, F. M. Cazorla, and M. Barón, *Metabolic responses of avocado plants to stress induced by rosellinia necatrix analysed by fluorescence and thermal imaging,* European Journal of Plant Pathology **142**, 625 (2015).

[14] M. Vázquez-Arellano, H. W. Griepentrog, D. Reiser, and D. S. Paraforos, *3-D imaging systems for agricultural applications—a review,* Sensors **16**, 618 (2016).

[15] S. Paulus, *Measuring crops in 3D: using geometry for plant phenotyping,* Plant Methods **15**, 1 (2019).

[16] S. Thapa, F. Zhu, H. Walia, H. Yu, and Y. Ge, *A novel LiDAR-based instrument for high-throughput, 3D measurement of morphological traits in maize and sorghum,* Sensors **18**, 1187 (2018).

[17] N. Camarretta, P. A. Harrison, A. Lucieer, B. M. Potts, N. Davidson, and M. Hunt, *From drones to phenotype: Using UAV-LiDAR to detect species and provenance variation in tree productivity and structure,* Remote Sensing **12**, 3184 (2020).

[18] Y. Bao, L. Tang, M. W. Breitzman, M. G. Salas Fernandez, and P. S. Schnable, *Field-based robotic phenotyping of sorghum plant architecture using stereo vision,* Journal of Field Robotics **36**, 397 (2019).

[19] S. Dhondt, H. Vanhaeren, D. Van Loo, V. Cnudde, and D. Inzé, *Plant structure visualization by high-resolution X-ray computed tomography,* Trends in Plant Science **15**, 419 (2010).

[20] H. Van As and J. Van Duynhoven, *MRI of plants and foods,* Journal of Magnetic Resonance **229**, 25 (2013).

[21] M. Hubeau and K. Steppe, *Plant-PET scans: in vivo mapping of xylem and phloem functioning,* Trends in Plant Science **20**, 676 (2015).

[22] S. Dhondt, N. Wuyts, and D. Inzé, *Cell to whole-plant phenotyping: the best is yet to come,* Trends in Plant Science **18**, 428 (2013).

[23] E. Truernit, H. Bauby, B. Dubreucq, O. Grandjean, J. Runions, J. Barthélémy, and J.-C. Palauqui, *High-resolution whole-mount imaging of three-dimensional tissue organization and gene expression enables the study of phloem development and structure in arabidopsis,* The Plant Cell **20**, 1494 (2008).

[24] J. W. Goodman, *Introduction to Fourier Optics* (McGraw-Hill, 1996).

[25] M. Govindarajulu, L. Epstein, T. Wroblewski, and R. W. Michelmore, *Host-induced gene silencing inhibits the biotrophic pathogen causing downy mildew of lettuce,* Plant Biotechnology Journal **13**, 875 (2015).

[26] G. Jach, E. Binot, S. Frings, K. Luxa, and J. Schell, *Use of red fluorescent protein from discosoma sp.(dsRED) as a reporter for plant gene expression,* The Plant Journal **28**, 483 (2001).

[27] S. J. Lawit, M. A. Chamberlin, A. Agee, E. S. Caswell, and M. C. Albertsen, *Transgenic manipulation of plant embryo sacs tracked through cell-type-specific fluorescent markers: cell labeling, cell ablation, and adventitious embryos,* Plant Reproduction **26**, 125 (2013).

[28] L. Donaldson, *Autofluorescence in plants,* Molecules **25**, 2393 (2020).

[29] T. Sugimoto, Y. Wada, S. Yamamura, and M. Ueda, *Fluorescence study on the nyctinasty of Cassia mimosoides L. using novel fluorescence-labeled probe compounds,* Tetrahedron **57**, 9817 (2001).

[30] J. Pawley, *Handbook of biological confocal microscopy*, Vol. 236 (Springer Science & Business Media, 2006).

[31] P. M. Kopittke, E. Lombi, A. Van Der Ent, P. Wang, J. S. Laird, K. L. Moore, D. P. Persson, and S. Husted, *Methods to visualize elements in plants,* Plant Physiology **182**, 1869 (2020).

[32] C. T. Anderson, A. Carroll, L. Akhmetova, and C. Somerville, *Real-time imaging of cellulose reorientation during cell wall expansion in Arabidopsis roots,* Plant Physiology **152**, 787 (2010).

[33] A. C. Timmers, *Light microscopy of whole plant organs,* Journal of Microscopy **263**, 165 (2016).

[34] D. Kurihara, Y. Mizuta, Y. Sato, and T. Higashiyama, *ClearSee: a rapid optical clearing reagent for whole-plant fluorescence imaging,* Development **142**, 4168 (2015).

[35] T. J. Musielak, L. Schenkel, M. Kolb, A. Henschen, and M. Bayer, *A simple and versatile cell wall staining protocol to study plant reproduction,* Plant Reproduction **28**, 161 (2015).

[36] P. P. Laissue, R. A. Alghamdi, P. Tomancak, E. G. Reynaud, and H. Shroff, *Assessing phototoxicity in live fluorescence imaging,* Nature Methods **14**, 657 (2017).

[37] J. Huisken, J. Swoger, F. Del Bene, J. Wittbrodt, and E. H. Stelzer, *Optical sectioning deep inside live embryos by selective plane illumination microscopy,* Science **305**, 1007 (2004).

[38] O. E. Olarte, J. Andilla, E. J. Gualda, and P. Loza-Alvarez, *Light-sheet microscopy: a tutorial,* Advances in Optics and Photonics **10**, 111 (2018).

[39] M. Ovečka, D. von Wangenheim, P. Tomančák, O. Šamajová, G. Komis, and J. Šamaj, *Multiscale imaging of plant development by light-sheet fluorescence microscopy,* Nature Plants **4**, 639 (2018).

[40] D. Huang, E. A. Swanson, C. P. Lin, J. S. Schuman, W. G. Stinson, W. Chang, M. R. Hee, T. Flotte, K. Gregory, C. A. Puliafito, *et al.*, *Optical coherence tomography,* Science **254**, 1178 (1991).

[41] R. Leitgeb, C. Hitzenberger, and A. F. Fercher, *Performance of Fourier domain vs. time domain optical coherence tomography,* Optics Express **11**, 889 (2003).

[42] M. A. Choma, M. V. Sarunic, C. Yang, and J. A. Izatt, *Sensitivity advantage of swept source and Fourier domain optical coherence tomography,* Optics Express **11**, 2183 (2003).

[43] T. Callewaert, J. Guo, G. Harteveld, A. Vandivere, E. Eisemann, J. Dik, and J. Kalkman, *Multi-scale optical coherence tomography imaging and visualization of Vermeer's Girl with a Pearl Earring,* Optics Express **28**, 26239 (2020).

[44] J. W. Hettinger, M. d. l. P. Mattozzi, W. R. Myers, M. E. Williams, A. Reeves, R. L. Parsons, R. C. Haskell, D. C. Petersen, R. Wang, and J. I. Medford, *Optical coherence microscopy. A technology for rapid, in vivo, non-destructive visualization of plants and plant cells,* Plant Physiology **123**, 3 (2000).

[45] T. H. Chow, K. M. Tan, B. K. Ng, S. G. Razul, C. M. Tay, T. F. Chia, and W. T. Poh, *Diagnosis of virus infection in orchid plants with high-resolution optical coherence tomography,* Journal of Biomedical Optics **14**, 014006 (2009).

[46] J. Gong, B. Liu, Y. L. Kim, Y. Liu, X. Li, and V. Backman, *Optimal spectral reshaping for resolution improvement in optical coherence tomography,* Optics Express **14**, 5909 (2006).

[47] Y. Liu, Y. Liang, G. Mu, and X. Zhu, *Deconvolution methods for image deblurring in optical coherence tomography,* Journal of the Optical Society of America A **26**, 72 (2009).

[48] Y. Takahashi, Y. Watanabe, and M. Sato, *Application of the maximum entropy method to spectral-domain optical coherence tomography for enhancing axial resolution,* Applied Optics **46**, 5228 (2007).

[49] Y. Ling, M. Wang, Y. Gan, X. Yao, L. Schmetterer, C. Zhou, and Y. Su, *Beyond Fourier transform: super-resolving optical coherence tomography,* arXiv preprint arXiv:2001.03129 (2020).

[50] R. Tripathi, N. Nassif, J. S. Nelson, B. H. Park, and J. F. de Boer, *Spectral shaping for non-Gaussian source spectra in optical coherence tomography,* Optics Letters **27**, 406 (2002).

[51] S. Hojjatoleslami, M. Avanaki, and A. G. Podoleanu, *Image quality improvement in optical coherence tomography using Lucy–Richardson deconvolution algorithm,* Applied Optics **52**, 5663 (2013).

[52] X. Liu, S. Chen, D. Cui, X. Yu, and L. Liu, *Spectral estimation optical coherence tomography for axial super-resolution,* Optics Express **23**, 26521 (2015).

[53] Y. Ling, M. Wang, X. Yao, Y. Gan, L. Schmetterer, C. Zhou, and Y. Su, *Effect of spectral leakage on the image formation of Fourier-domain optical coherence tomography,* Optics Letters **45**, 6394 (2020).

[54] K.-S. Lee and J. P. Rolland, *Bessel beam spectral-domain high-resolution optical coherence tomography with micro-optic axicon providing extended focusing range,* Optics Letters **33**, 1696 (2008).

[55] D. Lorenser, C. C. Singe, A. Curatolo, and D. D. Sampson, *Energy-efficient low-Fresnel-number Bessel beams and their application in optical coherence tomography,* Optics Letters **39**, 548 (2014).

[56] K. Sasaki, K. Kurokawa, S. Makita, and Y. Yasuno, *Extended depth of focus adaptive optics spectral domain optical coherence tomography,* Biomedical Optics Express **3**, 2353 (2012).

[57] R. Huber, M. Wojtkowski, J. G. Fujimoto, J. Jiang, and A. Cable, *Three-dimensional and C-mode OCT imaging with a compact, frequency swept laser source at 1300 nm,* Optics Express **13**, 10523 (2005).

[58] I. Grulkowski, K. Szulzycki, and M. Wojtkowski, *Microscopic OCT imaging with focus extension by ultrahigh-speed acousto-optic tunable lens and stroboscopic illumination,* Optics Express **22**, 31746 (2014).

[59] J. Mo, M. de Groot, and J. F. de Boer, *Depth-encoded synthetic aperture optical coherence tomography of biological tissues with extended focal depth,* Optics Express **23**, 4935 (2015).

[60] E. Bo and L. Liu, *Spectral domain optical coherence tomography with extended depth-of-focus by aperture synthesis,* in *Optics in Health Care and Biomedical Optics VII*, Vol. 10024 (SPIE, 2016) pp. 733–739.

[61] Y.-Z. Liu, F. A. South, Y. Xu, P. S. Carney, and S. A. Boppart, *Computational optical coherence tomography,* Biomedical Optics Express **8**, 1549 (2017).

[62] L. Yu, B. Rao, J. Zhang, J. Su, Q. Wang, S. Guo, and Z. Chen, *Improved lateral resolution in optical coherence tomography by digital focusing using two-dimensional numerical diffraction method,* Optics Express **15**, 7634 (2007).

[63] T. S. Ralston, D. L. Marks, P. Scott Carney, and S. A. Boppart, *Interferometric synthetic aperture microscopy,* Nature Physics **3**, 129 (2007).

[64] R. H. Stolt, *Migration by fourier transform,* Geophysics **43**, 23 (1978).

[65] N. D. Shemonski, S. G. Adie, Y.-Z. Liu, F. A. South, P. S. Carney, and S. A. Boppart, *Stability in computed optical interferometric tomography (Part I): Stability requirements,* Optics Express **22**, 19183 (2014).

[66] A. Ahmad, N. D. Shemonski, S. G. Adie, H.-S. Kim, W.-M. W. Hwu, P. S. Carney, and S. A. Boppart, *Real-time in vivo computed optical interferometric tomography,* Nature Photonics **7**, 444 (2013).

[67] K. Oikawa, D. Oida, S. Makita, and Y. Yasuno, *Bulk-phase-error correction for phase-sensitive signal processing of optical coherence tomography,* Biomedical Optics Express **11**, 5886 (2020).

[68] Y. Xu, X. K. B. Chng, S. G. Adie, S. A. Boppart, and P. S. Carney, *Multifocal interferometric synthetic aperture microscopy,* Optics Express **22**, 16606 (2014).

[69] G. R. Littlejohn, J. C. Mansfield, J. T. Christmas, E. Witterick, M. D. Fricker, M. R. Grant, N. Smirnoff, R. M. Everson, J. Moger, and J. Love, *An update: improvements in imaging perfluorocarbon-mounted plant leaves with implications for studies of plant pathology, physiology, development and cell biology,* Frontiers in Plant Science **5**, 140 (2014).

[70] S. G. Adie, B. W. Graf, A. Ahmad, P. S. Carney, and S. A. Boppart, *Computational adaptive optics for broadband optical interferometric tomography of biological tissue,* Proceedings of the National Academy of Sciences **109**, 7175 (2012).

[71] S. G. Adie, N. D. Shemonski, B. W. Graf, A. Ahmad, P. Scott Carney, and S. A. Boppart, *Guide-star-based computational adaptive optics for broadband interferometric tomography,* Applied Physics Letters **101**, 221117 (2012).

[72] D. Hillmann, C. Pfäffle, H. Spahr, S. Burhan, L. Kutzner, F. Hilge, and G. Hüttmann, *Computational adaptive optics for optical coherence tomography using multiple randomized subaperture correlations,* Optics Letters **44**, 3905 (2019).

[73] R. Wijesinghe, S.-Y. Lee, N. K. Ravichandran, M. F. Shirazi, and P. Kim, *Optical screening of Venturianashicola caused Pyruspyrifolia (Asian pear) scab using optical coherence tomography,* International Journal of Applied Engineering Research **11**, 7728 (2016).

[74] T. Anna, S. Chakraborty, C.-Y. Cheng, V. Srivastava, A. Chiou, and W.-C. Kuo, *Elucidation of microstructural changes in leaves during senescence using spectral domain optical coherence tomography,* Scientific Reports **9**, 1167 (2019).

[75] R. A. Leitgeb, R. M. Werkmeister, C. Blatter, and L. Schmetterer, *Doppler optical coherence tomography,* Progress in Retinal and Eye Research **41**, 26 (2014).

[76] J. Lee, W. Wu, J. Y. Jiang, B. Zhu, and D. A. Boas, *Dynamic light scattering optical coherence tomography,* Optics Express **20**, 22262 (2012).

[77] R. F. Spaide, J. G. Fujimoto, N. K. Waheed, S. R. Sadda, and G. Staurenghi, *Optical coherence tomography angiography,* Progress in Retinal and Eye Research **64**, 1 (2018).

[78] T. Kohlfaerber, M. Pieper, M. Münter, C. Holzhausen, M. Ahrens, C. Idel, K.-L. Bruchhage, A. Leichtle, P. König, G. Hüttmann, *et al.*, *Dynamic microscopic optical coherence tomography to visualize the morphological and functional micro-anatomy of the airways,* Biomedical Optics Express **13**, 3211 (2022).

[79] D. J. Faber, E. G. Mik, M. C. Aalders, and T. G. van Leeuwen, *Toward assessment of blood oxygen saturation by spectroscopic optical coherence tomography,* Optics Letters **30**, 1015 (2005).

[80] A. Lichtenegger, D. J. Harper, M. Augustin, P. Eugui, M. Muck, J. Gesperger, C. K. Hitzenberger, A. Woehrer, and B. Baumann, *Spectroscopic imaging with spectral domain visible light optical coherence microscopy in Alzheimer's disease brain samples,* Biomedical Optics Express **8**, 4007 (2017).

[81] U. M. Rajagopalan, M. Kabir, Y. Lim, and H. Kadono, *Biospeckle optical coherence tomography in speedy visualizing effects of foliar application of plant growth hormone to Chinese chives leaves,* BMC Research Notes **13**, 1 (2020).

[82] Y. S. K. De Silva, U. M. Rajagopalan, H. Kadono, and D. Li, *Positive and negative phenotyping of increasing Zn concentrations by biospeckle optical coherence tomography in speedy monitoring on lentil (Lens culinaris) seed germination and seedling growth,* Plant Stress **2**, 100041 (2021).

2

Quantification of plant morphology and leaf thickness with optical coherence tomography

Optical coherence tomography (OCT) can be a valuable imaging tool for in-vivo and label-free digital plant phenotyping. However, for imaging leaves, air-filled cavities limit the penetration depth and reduce the image quality. Moreover, up to now quantification of leaf morphology with OCT has been done in 1D or 2D images only, and has often been limited to relative measurements. In this paper, we demonstrate a significant increase in the OCT imaging depth and image quality by infiltrating the leaf air spaces with water. In the obtained high-quality OCT images the top and bottom surface of the leaf are digitally segmented. Moreover, high-quality en face images of the leaf are obtained from numerically flattened leaves. Segmentation in 3D OCT images is used to quantify the spatially resolved leaf thickness. Based on a segmented leaf image, the refractive index of an infiltrated leaf is measured to be 1.345± 0.004, deviating only 1.2% from that of pure water. Using the refractive index and a correction for refraction effects at the air-leaf interface we quantitatively mapped the leaf thickness. The results show that OCT is an efficient and promising technique for quantitative phenotyping on leaf and tissue level.

This chapter has been published as: **Jos de Wit**, Sebastian Tonn, Guido Van den Ackerveken, and Jeroen Kalkman, *Quantification of plant morphology and leaf thickness with optical coherence tomography*, Applied Optics 59, 10304-10311 (2020).

2.1. Introduction

With an increasing world population and growing biofuel consumption, the demand for crops is expected to increase rapidly over the coming decades [1]. Plant scientists use methods such as crop monitoring, environment control, early disease detection, and plant breeding to improve both the quality and quantity of food production. Plant phenotyping, i.e., the evaluation of the performance and appearance of a plant in its environment, is a crucial step in the development and optimization of these methods. Traditional phenotyping, i.e., scoring of plants by human raters based on visual inspection, is more and more replaced by digital phenotyping, which aims to objectively and quickly quantify relevant plant traits at low costs [2]. Imaging and computer vision approaches play a central role in digital phenotyping. While many studies focus on high-throughput phenotyping with limited resolution and dimensionality, the long term goal is for 3D high-resolution phenotyping for a deeper comprehension of plant phenotypes [3]. In this paper, we show how optical coherence tomography (OCT) can contribute to plant trait quantification in high-resolution phenotyping.

Leaves are the plant's organs where sunlight is captured and carbohydrates are synthesized, making them an important object for high-resolution plant phenotyping on organ, tissue and cellular scale [3]. Microscopic phenotyping of plant leaves often needs fixation, clearing and staining, especially when the deeper mesophyll layer and vascular tissue are investigated [4, 5]. Such extensive sample preparation not only reduces phenotyping throughput, but also makes it impossible to do longitudinal *in-vivo* measurements. Longitudinal measurements, i.e., following the same tissue in time, are important to study leaf dynamics such as leaf growth and plant interaction with the environment [6, 7].

Tomographic methods such as magnetic resonance imaging (MRI) and high-resolution X-ray computed tomography (HRXCT) are able to obtain 3D images of leaf morphology *in-vivo* at resolutions of typically 30 µm for MRI and 10 µm for HRXCT [8]. Drawbacks of these computed tomographic methods are their low speed and high costs [9], as well as the trade-off between sample size and resolution [8].

Optical coherence tomography is developed for label-free *in-vivo* imaging deep into scattering biological tissue [10]. OCT has been used to obtain 3D images of plants with resolutions between 5 and 10 µm. Due to the combination of confocal gating and coherence gating, multiply scattered light is largely filtered out and the penetration depth becomes many times that of confocal microscopy. It has been used to reveal plant anatomy [11, 12], detect plant diseases [13–17], study leaf senescence [18] and investigate root growth dynamics [19]. Moreover, OCT is used in post-harvest quality evaluation of agriculture produce [20].

Most OCT studies on (early) disease detection compared A-scans that were obtained by laterally averaging flattened B-scans [13–16]. Pathogen induced cell degradation results in a broadening of, or a changing distance between, peaks in the average A-scan. This has been successfully used as a bio-marker for plant diseases. Wijesinghe et al. quantified the average thickness of the palisade parenchyma layer by dividing the optical path length (OPL) between the two peaks in the average A-

scan through an assumed leaf refractive index [14, 15]. Other studies described changes in the average A-scan in a mere qualitative way. Chow et al. used scattering intensity as a measure for disease infection, but the values were given in arbitrary units and are hence not transferable between setups [17]. Anna et al. measured the attenuation coefficient of leaves as an indicator of senescence [18]. Additionally, they calculated texture parameters of gray level B-scans to quantitatively classify different stages of senescence.

However, all these studies demonstrate two major drawbacks. First, none of these studies were able to clearly visualize the entire cross-section of a mature leaf, including the opposite leaf surface, due to a limited penetration depth. Even if signals are picked up from deeper regions, the signals that have a low signal-to-noise ratio (SNR) are further deteriorated due to multiply scattered photons and sample-induced aberrations. The relatively low penetration depth as compared to other biological tissues is caused by the fact that leaves contain air-filled cavities. At these air-tissue interfaces, strong scattering and refraction occur, giving rise to the multiply scattered signal and sample-induced aberrations [21]. This effect can be largely reduced by infiltrating the leaves with a liquid that has a refractive index close to that of the leaf tissue. Infiltration of leaves with perfluorodecalin (PFD) has been used to enhance the resolution and image quality in *in-vivo* confocal microscopy [22]. PFD has a low surface tension and thus infiltrates easily into the leaf even under atmospheric pressure. Infiltration with PFD is done by soaking the leaves for 5 minutes in the solution [23], which is difficult to apply on leaves still on the plant. Water also can be infiltrated into leaves, by pressing the opening of a water-filled syringe against the abaxial leaf epidermis and applying gentle pressure, or by releasing air from leaves held underwater using a vacuum pump allowing water to enter after the vacuum is gently released [24]. Syringe-based water infiltration takes a few seconds and the infiltrated leaves dry within an hour, returning the leaf to its normal state. Moreover, water is available everywhere, significantly cheaper than PFD and it is part of the natural environment of plants. Both PFD and water are believed to have marginal physiological effects and thus infiltration with these liquids is feasible with *in-vivo* imaging [22].

Second, the mentioned publications did not show quantification of 3D leaf morphology and layer thickness. Current leaf quantification often yields relative values that cannot be translated into objective physical quantities. For example, the measured OPL was not always transformed into physical thickness, and if done, a literature value for water or plant cells was used. Moreover, most quantification was based on laterally averaged A-scans that do not capture the full 3D shape. This is mainly because of a lack of application of advanced image processing and segmentation.

A particular morphological feature that is of interest is leaf thickness, which can be important, for example, to accurately determine a plant's biomass [25]. The current methods to measure lateral resolved leaf thickness require extensive clearing [5], complex and costly equipment [25], or a custom-build complex setup [26], or give no accurate results [27]. OCT can be an attractive alternative method to measure leaf thickness, especially when combined with a study of the internal leaf

tissue morphology.

In this paper, we address the problems of limited penetration depth and lack of quantification of 3D morphology in current OCT plant imaging. First, we demonstrate that water infiltration successfully extends the penetration depth and gives higher quality images. Second, we use these higher quality images in combination with image processing and segmentation to quantify lateral resolved leaf thickness. Compared to alternative methods, OCT is a simple and cost-efficient tool for measuring lateral resolved leaf thickness.

2.2. Methods

2.2.1. Experimental OCT setup

The measurements are performed with a high-resolution spectral-domain OCT setup (Ganymede II HR, Thorlabs, Germany), that has a super-luminescent diode light source with a center wavelength of 900 nm and a full width half maximum (FWHM) bandwidth of 120 nm. The axial resolution is experimentally measured to be 3.0 µm in air, which corresponds to 2.2 µm in tissue. The spectrometer covers a bandwidth of 220 nm over 2048 pixels, giving a spectral sampling resolution of 0.11 nm and an axial imaging range of 1.87 mm in air. The system is operated with an A-scan rate of 36 kHz, enabling real-time acquisition of B-scans and sub-minute acquisition of volume scans. The objective lens (OCT-LK4-BB, Thorlabs, Germany) has a working distance of 41.6 mm and a maximum lateral field of view of 16 mm×16 mm, though in this research smaller scan areas were used to reduce the memory usage. The lateral resolution is experimentally determined with a knife-edge imaging a step response to have a FWHM of 6 µm. The raw spectral data is obtained with ThorImage software (version 5.2.0). The B-scans consist of 1024 A-scan lines over a width of 3 mm in x-direction, corresponding to a scan-line every 3 µm. Every A-scan is averaged 8 times to improve the signal-to-noise-ratio (SNR). The 3D scans consist of 512×512 scan lines over an area of 3×3 mm^2. The resulting separation of 6 µm between the scan-lines, corresponds well to the lateral resolution resulting in a

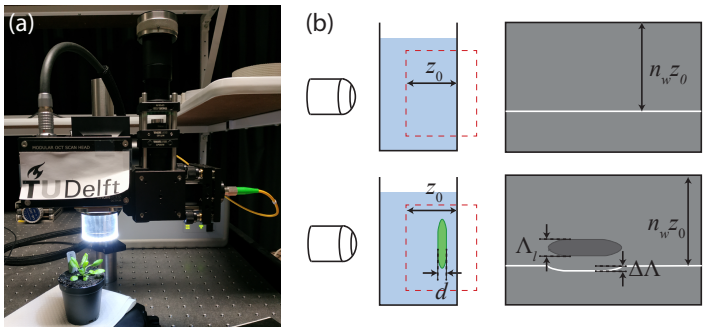

Figure 2.1: The SD-OCT setup that was used for this study. (a) The setup in action and (b) a schematic overview of the refractive index measurement. The red dashed boxes indicate the area of the image. z_0 and d are physical distances, while Λ is the distance in OPL.

well-sampled volume. One of the limitations of volume OCT imaging is the size of the data sets that are created. For the 3D acquisition with 2048 pixels per A-scan and 2 bytes per pixel (for 12 bit numbers), the raw spectral data has a size of 1 GB. To limit the data size, only two averages per A-line are made, giving a raw spectral data size of 2 GB. The scan time of $512 \times 512 \times 2$ A-scans is 15 s, which gives no practical limitation for application in plant imaging.

The raw spectral data is processed in Python 3 to obtain high-quality images. The processing consists of subsequently the subtraction of the reference spectrum, interpolation to an equally spaced grid in wavenumber domain, apodization with a Hanning window, correction for dispersion mismatch, and an inverse discrete Fourier transform. The numerical correction for dispersion mismatch between the reference and sample arm is done with a fourth-order polynomial, whose coefficients are obtained from a reference measurement of a single reflector [28]. After processing, the A-scans belonging to the same scan line are complex averaged to improve the SNR [29]. For segmentation, the absolute value of the complex averaged scan lines is used directly. For displaying in images this amplitude is subsequently converted to a dB scale by dividing through the maximum, taking the 10-base logarithm, and multiplying with 20.

2.2.2. Plant material

Measurements are taken on a fully developed leaf of a mature 4 week old Arabidopsis plant of accession C24 [30]. The leaf is infiltrated by pressing the mouth of a syringe to the abaxial side of the leaf and gently pushing the water into the leaf until it is completely infiltrated, visible because of the induced translucence. The infiltrated leaf dries within an hour and the physiological effects of infiltration on the leaf are minimal. After drying, the area of infiltration is not recognizable by the naked eye, nor in the OCT scan. This allows for *in-vivo* imaging of the same area of a leaf longitudinal, i.e. at different times during growth. The OCT measurements are taken from the adaxial (top) side of the leaf. The leaf can remain on the plant, as the whole plant is placed below the scan-head as shown in Fig. 2.1 (a). The sample is placed below the zero-delay with an extra offset to separate the image from auto-correlation artifacts.

2.2.3. Surface segmentation

For quantitative analysis of the morphological traits of plant leaves, the location of the top surface and bottom surface of the leaf are segmented.

The segmentation starts with an OCT cross-sectional image (Fig. 2(a)), where the signal from the entire leaf is well above the noise level. Thresholding is applied to obtain a rough segmentation of the leaf. The threshold is taken sufficiently low to capture the weaker reflections from the bottom surface and the places where the local normal of the top surface of the leaf is tilted with respect to the optical axis. This results in the segmentation M_s, as shown in yellow and green in Fig. 2.2(b).

The segmentation by thresholding includes many high-intensity side lobes, visible as the light green lobes on the surface in Fig. 2.2(b), annotated with arrow sl. To remove these side-lobes, an additional requirement is imposed that the second-

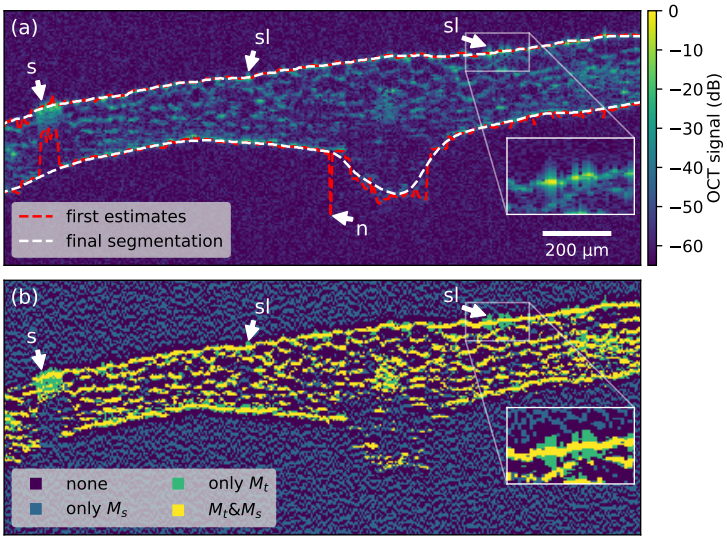

Figure 2.2: Illustration of the steps in surface segmentation to obtain leaf thickness. (a) A cross-sectional OCT image and the results of the two steps in image segmentation. (b) The segmentations resulting from thresholding (M_t, green), from taking a negative second derivative (M_s, light blue) and the overlap of both (yellow). The arrows point to a soil particle (s), side lobes of the top reflection (sl) and noise above the threshold (n).

order Gaussian derivative ($\sigma = 3$ pixels) along the axial direction should be negative. This negative second derivative filter (M_s, light blue and yellow) effectively acts as a local maximum filter, discarding the band before the peak positions of the top and bottom surface. It successfully removes the side-lobes and increases the accuracy of the segmentation of mainly the top surface.

Subsequently, the first and last non zero pixels for each A-scan in this segmentation are taken as the first estimates for respectively the top and bottom surface, indicated with the red line in Fig. 2.2(a). Higher intensity noise (indicated with n) and structures like leaf hairs or small soil particles (indicated with s) result in outliers in these first surface estimates. To remove the outliers a median filter is applied with a 7 pixel radius circular footprint. After median filtering, the bottom surface is smoothed by a Gaussian kernel with a sigma of 5 pixels. These filters result in a smooth and accurate segmentation for the top and bottom surface, as indicated with the white dashed line. Implemented with Python operating in Spyder on a desktop (Intel Xeon W-2223 CPU), the surface segmentation of the 512x512 scan lines volume took 24 s, of which 15 s spent on calculating the Gaussian derivative filtered image.

2.2.4. Leaf refractive index measurement

Optical coherence tomography measures axial distances in optical path length (OPL). Conversion between OPL and depth is done by dividing through the refractive index of the medium, in this case, the refractive index of infiltrated leaf tissue.

We quantify the refractive index of an infiltrated leaf with a method similar to the *in-vitro* method of Tearney et al. [31]. A water-filled cuvette is imaged twice: first with the leaf placed in a cuvette close to the back surface, then after the leaf is removed while the probe and cuvette remain in their position, as shown in Fig. 2.1(b). The displacement of the wall of the cuvette between the two OCT images is equal to the difference in OPL between light going through the leaf tissue and light going through water. The relative difference of the refractive index can be calculated for each lateral position with

$$\frac{n_l - n_w}{n_w} = \frac{\Delta\Lambda}{\Lambda_l - \Delta\Lambda}, \tag{2.1}$$

in which n_l and n_w are the refractive indices of respectively an infiltrated leaf and water, Λ_l is the thickness of the leaf in OPL and $\Delta\Lambda$ is the displacement of the cuvette wall in OPL, as indicated in Fig. 2.1(b). Although this method does not account for refraction at the leaf surface, the resulting error will be insignificant as the difference in the refractive index is expected to be small. For fully automated refractive index measurement, both the leaf and cuvette surface are segmented. Λ_l is obtained from the surface segmentation as described in Section C. The location of the cuvette wall is obtained for each A-scan by fitting a Gaussian to a manually selected 100 µm wide axial region around the cuvette wall. The obtained peak locations are subsequently median filtered with a 25 pixel window to remove outliers, and then Gaussian filtered with a sigma of 15 pixels to obtain a smooth curve. For each lateral position equation (2.1) is evaluated. The final refractive index is obtained by averaging over all lateral positions.

2.2.5. Leaf thickness measurement

For each lateral position, the distance in OPL between the top and bottom surface is divided by n_l to obtain the physical distance l between the top and bottom surface.

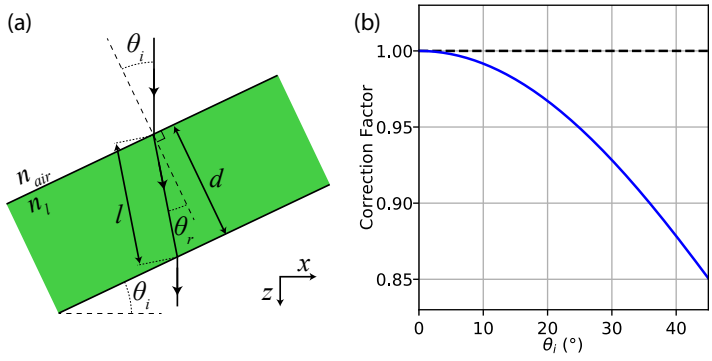

Figure 2.3: (a) The geometry and parameters for calculating the correction factor. The scan beam falls in in vertical direction and the leaf is tilted with an angle θ_i with respect to the horizontal. x and z are respectively the horizontal and vertical coordinate in the images. (b) The correction factors for leaf tilting angles θ_i between 0° and 45°, using $n_l = 1.345$.

This distance l is measured along the beam path, thus it will be larger than the leaf thickness d for an oblique leaf surface, as indicated in Fig. 2.3. Taking refraction into account and assuming that the leaf can locally be considered as having two parallel surfaces, the true leaf thickness d can be obtained with

$$d = l\sqrt{1 - \left(\frac{\sin\theta_i}{n_l}\right)^2}, \tag{2.2}$$

where d is the local thickness measured perpendicular to the top surface, l is the local thickness measured as the distance in the A-scan between the top and bottom reflection, θ_i is the angle of the leaf surface with respect to the optical axis, and n_l the leaf refractive index, as shown in Fig. 2.3(a). Fig. 2.3(b) shows the values of the correction factor d/l for incident angles up to 45°. The local θ_i is calculated by taking the inverse tangent of the Gaussian gradient magnitude of the top surface with a sigma of 10 pixels (60 µm). The leaf thickness d is calculated with Eq. (2.2).

2.2.6. En face OCT images

With the segmented top surface en face images at a fixed depth below the top surface are made. The leaf in the C-scan is numerically flattened by shifting the leaf top surface to the first pixel for each A-scan. From each depth of interest, a slice in the transverse direction is taken and displayed as an en face image. The reference intensity for conversion to the dB scale is the maximum value of the entire data set.

2.3. Results

2.3.1. The result of leaf infiltration on the OCT imaging depth

Figure 2.4 shows an image of the same leaf before and after infiltration. The images are not taken from exactly the same position as the plant moved during infiltration. In both images, the adaxial epidermal cells are clearly visible, as well as the mesophyll cells just below the epidermal cells. At some places, the strong reflections from the air-leaf interface give side-lobes that partly obscure the epidermal cells. Without infiltration, the image gets blurry after penetration of about 100 µm OPL. As this leaf is relatively thin, the abaxial side can be seen from a drop of intensity after about 200 µm OPL, but the transition is rather vague and its location far from precise. Moreover, the B-scan area crosses the midrib around the center of the image, but this is not visible in the image.

The relatively poor image quality in the deeper regions of the non-infiltrated leaf can be understood from the presence of air-filled cavities that the plant uses for gas exchange. These cavities with a refractive index that is much lower than that of leaf tissue cause aberrations and refraction of the beam such that the back-reflected signals are disturbed and, if collected, mapped to the wrong location. The many air-tissue interfaces also cause a lot of multiple scattering, which further decreases the visibility of deeper-lying structures in the leaf. Multiple scattering also gives rise to the haze, visible at the bottom of the leaf, which corresponds to the longer

path lengths of multiply scattered light [32]. This further obscures the abaxial leaf surface in the image.

Filling these cavities with water by infiltrating the leaves makes them much more transparent to the OCT signal, thereby reducing sample-induced aberrations and multiple scattering. In figure 2.4(b), cells are visible in the deeper regions of the cell, and also the vascular tissue in the midrib can be clearly distinguished. The clearest difference between the images is that with infiltration the abaxial side of the leaf is clearly and accurately imaged. Moreover, the shape of the midrib on the abaxial side can be clearly distinguished. The comparison of these images shows the huge benefit of infiltration for OCT imaging of plant leaves, making it possible to clearly image the full cross-section of the leaf *in-vivo*, and also quantifying leaf thickness as a function of lateral position. The latter we will explore in the next subsection.

2.3.2. Leaf refractive index measurement

Figure 2.5(a-b) shows a B-scan of a water-filled cuvette with and without an infiltrated leaf. The white arrows point to an auto-correlation artifact of the cuvette wall, which is sufficiently separated from the relevant features to enable accurate segmentation. The vertical stripes in the images are probably caused by aliasing of reflections of a surface of the cuvette outside the axial range. These artifacts do, however, not cause any problems in the segmentation as their intensity is well below the intensity of the leaf and the cuvette wall. The segmented leaf and cuvette surface are indicated with a white and red dashed line respectively. The average

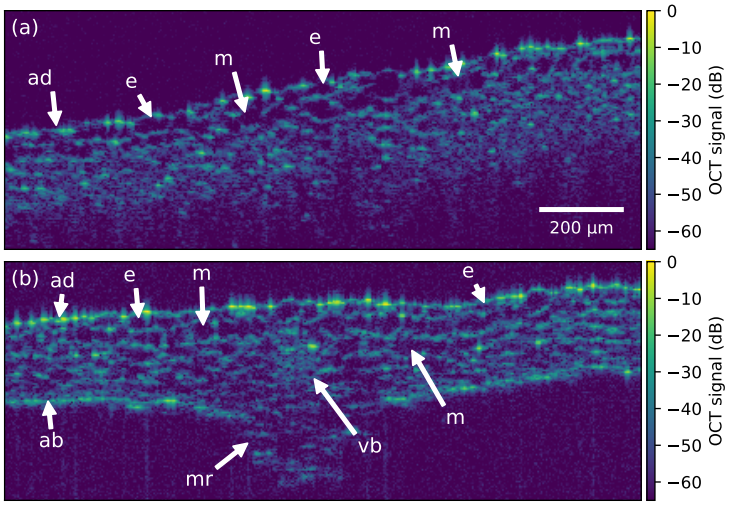

Figure 2.4: B-scan images of the central part of an Arabidopsis leaf. (a) An image before infiltration and (b) an image after infiltration. The scan area of (a) crosses the midrib about halfway the image. In (b) the midrib and vascular tissue are clearly visible. Contrary to (a), the abaxial side of the leaf is clearly visible in (b). Annotations: e: epidermal cell, m: mesophyll cell, vb: vascular bundle, mr: midrib, ad: adaxial side and ab: abaxial side.

difference in OPL of the cuvette $\overline{\Delta\Lambda} = 2$ µm, which corresponds to 1 pixel. For each lateral position equation (2.1) is evaluated and the result of it plotted in Fig. 2.5(c). The average relative difference in the refractive index between infiltrated leaf tissue and water is 1.2%. This relative difference is small enough to justify the neglect of refraction at the leaf surface. Using the literature value $n_w = 1.329$ at the center wavelength of the OCT setup ($\lambda_c = 900$ nm) [33], we obtain a refractive index for infiltrated leaf tissue of $n_l = 1.345 \pm 0.004$. The variation in the measured refractive index is caused by a combination of both uncertainty in measurement and segmentation, and natural variation of leaf tissue.

2.3.3. Leaf thickness

The leaf thickness is determined for a section of the leaf around the midrib, indicated with the red box in Fig. 2.6(a). Fig. 2.6(b) shows the segmented top and bottom surface in 3D. The midrib is clearly visible in the segmentation of the bottom surface. The peak at the right side is an artifact caused by the presence of a trichome (a leaf hair). The correction factor d/l as defined by (2.2) is evaluated and visualized in Fig. 2.6(c). For the major part of the surface, this factor is close to 1; at the lower half of the image, it decreases to values down to 0.93 due to the slope of the surface. Around the leaf hair, the gradient magnitude becomes much larger, resulting in local correction factors up to 0.83. From the segmentation, the correction factor

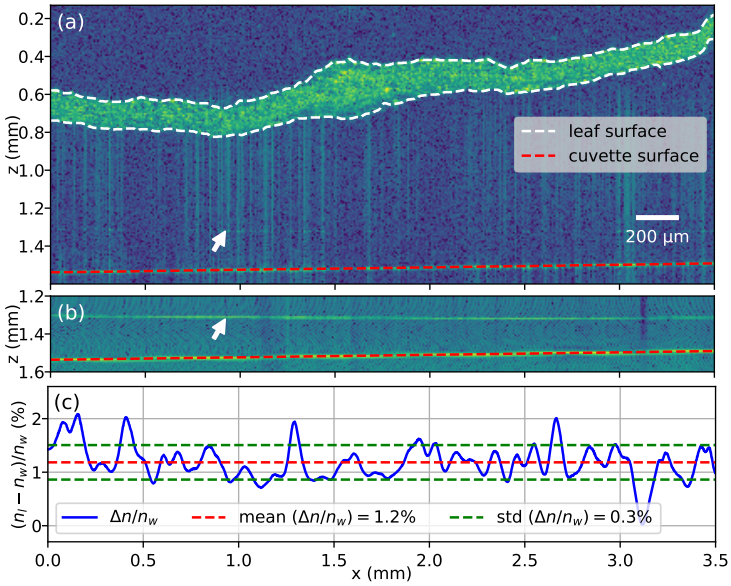

Figure 2.5: (a) B-scan image of an infiltrated leaf in a cuvette and (b) the image after the leaf has been removed while the setup and cuvette remained untouched. From the segmentation of the leaf surface and the cuvette surface, the relative refractive index difference is calculated per lateral position using (2.1) and plotted in (c). The mean relative difference $\overline{\Delta n/n_w}$ is indicated with the red dashed line and the green dashed lines indicate the single standard deviation borders.

and the measured refractive index $n_l = 1.345$, the lateral resolved leaf thickness is determined and visualized in Fig. 2.6(d). The midrib is clearly visible due to its large thickness ranging from 260 µm at the right to 366 µm at the left of the image. Moreover, the veins can be distinguished with a thickness of around 180 µm, while the lamina or leaf blade has a thickness varying between 110 µm and 150 µm. Two artifacts, caused by a soil particle and leaf hair, are indicated with arrows.

2.3.4. En face images

Using the surface segmentation, en face images are obtained at different depths with respect to the top surface of the leaf. This is shown in the single OCT cross-section in Fig. 2.7(a), with the lines indicating the depths in OPL of the en face images (b-f). In the cross-sectional image, the vascular bundle inside the midrib is clearly visible and has a diameter of about 120 µm.

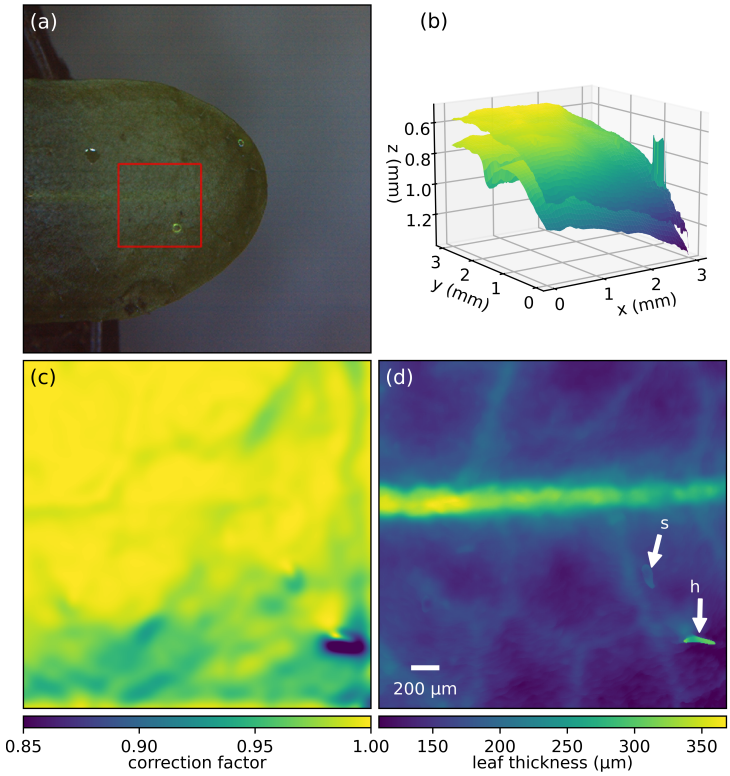

Figure 2.6: (a) The RGB image with the scan region indicated with the red box, (b) the segmented top and bottom surface, (c) the correction factor for tilted surfaces taking refraction into account, and (d) the lateral resolved leaf thickness assuming $n_l = 1.345$. The arrows indicate small artifacts in the segmentation due to a soil particle (s) and a leaf hair (h). The leaf hair is visible as the peak on the right side of (b).

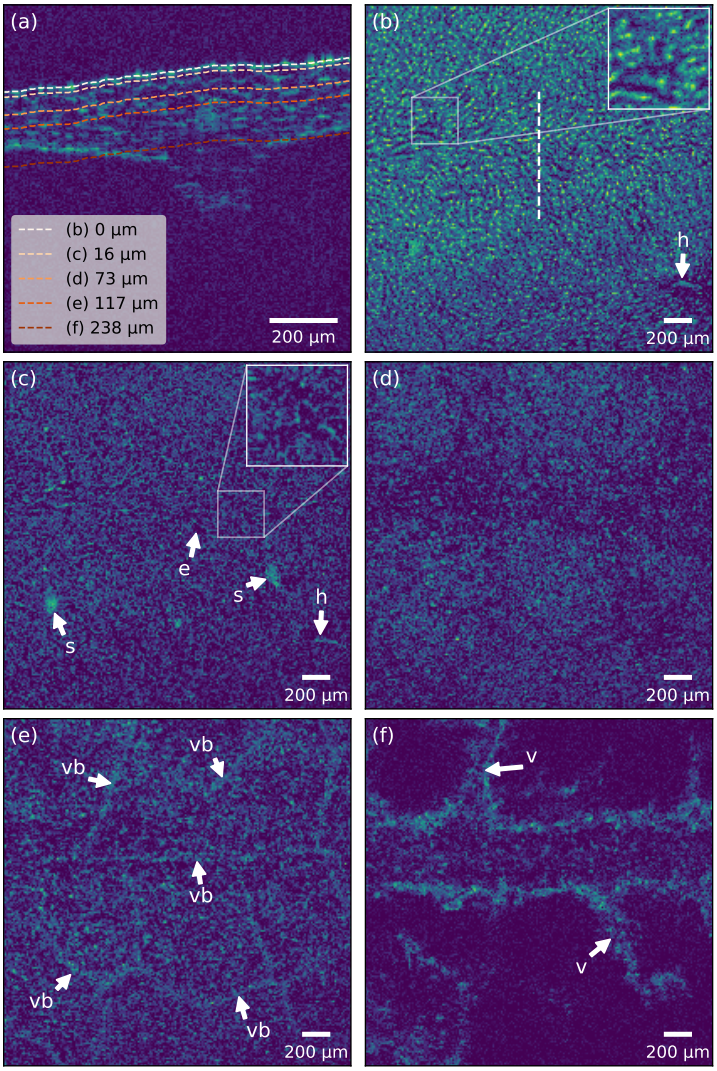

Figure 2.7: En face images of the leaf at a fixed distance in OPL from the adaxial surface, generated from the same data that is used in figure 2.6. The lines in (a) indicate the depth of the images in (b-f). (b) OCT surface intensity showing the cuticle and the top surface of the epidermal cells. The white dashed line indicates the location of the cross-section (a). (c) The image at 16 µm depth, which is located in the epidermal layer. (d) The image at 73 µm depth, which is located in the palisade mesophyll layer. (e) The image at 117 µm, showing the vascular bundles of the midrib and veins, and the spongy mesophyll layer between the veins. Several vascular bundles are annotated. (f) The image at 238 µm, which is below the leaf at the lamina or leaf blade, while it still contains tissue around the midrib and leaf veins. All images are plotted on a scale between 0 and -65 dB, where 0 refers to the maximum value in the 3D data set. The distance from the surface and z in (a) are given in OPL. Annotations: e: epidermal cell, h: leaf hair, s: soil particle, vb: vascular bundle, and v: vein.

The first layer (Fig. 2.7(b)) corresponds to the cuticle and the top of the epidermal cells. The air-tissue interface gives strong reflections, resulting in high intensities in this image. The structure in the image is an indication of the local orientation of the leaf surface. A surface normal along the axis of the OCT beam gives a high-intensity signal back on the detector. The reflected intensity decreases with an increasing angle. The bottom 0.5 mm area has a lower average intensity as the leaf surface is sloped downwards there. In the right bottom, a leaf hair is visible, which caused an artifact in the top surface segmentation. Figure 2.7(c) is located at the epidermal layer, and indeed many epidermal cells can be distinguished, better visible in the inset. The typical width of the lobes of the cells is 40 to 50 µm. Two bright dots contain the high-intensity reflections from grains of soil, and also the leaf hair is still visible. The epidermal cells are less well visible in the lower part, probably due to the sloped surface. Figure 2.7(d) shows the palisade mesophyll layer, and has a distinctly different texture than the epidermal layer. The lateral size of the cells is smaller, typical 20-30 µm, giving a finer texture. This layer has a more open structure at the midrib and also at some of the larger veins. When we go deeper to 117 µm (OPL) into the leaf, the vascular bundles can be seen in the midrib and the veins. The location of these vascular bundles corresponds well with the location of veins in Fig. 2.6(d). The mesophyll cells in the lamina areas look slightly more open than those in Figure 2.7(d), which indicates that this slice is indeed through the spongy mesophyll with many cavities for gas exchange and the one in (d) is located in the palisade mesophyll layer. The cavities have an irregular structure, but the width along their smallest dimension is typical 50-70 µm, and up to 90 µm close to the midrib. When taking a slice below the bottom surface of the lamina regions, the veins and the thicker leaf at the edges of the midrib are clearly visible. The signal at the right bottom is due to a locally thicker surface as can be seen from Fig. 2.6(b). Cross-section images show that this thickening appears both at the top and the bottom, which may be related to the leaf hair that is in its vicinity.

2.4. Discussion

This work presents water infiltration as a method to increase the OCT imaging depth and image quality of plant leaves. In addition, we show quantification of the refractive index of leaves and the lateral resolved leaf thickness.

The key advantages of OCT for quantifying lateral resolved leaf thickness are that it is fast, minimally invasive, compatible with label-free *in-vivo* imaging, that it gives leaf thickness and internal leaf morphology at once, and at relatively low cost using commercially available systems. The results presented in this paper show that OCT can be successfully used to quantify spatially resolved leaf thickness and that it provides further insight into the underlying leaf morphology.

A disadvantage of our method is that infiltration locally changes the leaf environment. As water is added to the leaf, this method may be less suitable for longitudinal drought monitoring studies. However, when the time between measurements is longer than the drying time of the leaf, the physiological effects of infiltration will probably be limited. Based on the presented results, it cannot be ex-

cluded that infiltration has any effect on the leaf thickness. However, this effect will be less than with optical clearing and be the same for different plants or leaf areas. Therefore, it will barely limit the applicability for plant studies. Syringe infiltration sometimes bruises the leaf on the small ring where the syringe mouth is pressed on the leaf. This can be avoided by using a vacuum pump or PFD infiltration, which is expected to give similar imaging results.

Sample-induced beam deviation and systematic errors in the segmentation may be a source for systematic errors or inaccuracy of the leaf thickness measurement. Therefore, the proposed method to compensate for beam refraction is essential to obtain an accurate result with an oblique leaf surface. Even with this method, the limited axial imaging range and the possibility of image warping still require the orientation of the leaves to be as close to horizontal as possible.

The accuracy of the leaf thickness quantification depends on the quality of the surface segmentation. In this work, we present a simple but robust segmentation method that gives good results, excluding side lobes at the top surface that would otherwise have caused a systematic error towards a thicker surface. Structures on the surface, like leaf hairs, cause errors in the segmentation. These artifacts can be removed by more aggressive filtering, at the expense of losing spatial detail. Smaller leaf hairs, of plants such as tomato or lettuce, will be largely filtered out by the proposed median filter. Moreover, leaf hairs can be a relevant feature of a plant's phenotype and OCT is very suitable to quantify both their surface density and 3D shape. The speed and accuracy of the segmentation may be improved by applying more advanced segmentation methods, for example based on deep-learning.

Our approach can also be applied to other plant species with different leaf sizes. Using syringe infiltration, we successfully imaged full cross-sections, including the bottom surface, of lettuce, tomato, dandelion and ribwort plantain leaves. However, plant leaves with many fibers, such as willow or reed leaves, were difficult to infiltrate with a syringe. Moreover, the attenuation of these leaves is higher. Therefore, our method worked less well for such leaves. We obtained the best imaging results with fresh and green leaves, where we were able to image full cross-sections for leaf thicknesses up to 350 µm.

For very thick or highly scattering leaves, infiltration may not give enough increase in penetration depth to accurately image the other side of the leaf. The penetration depth can be increased by using an OCT system with a larger center wavelength, at the expense of a lower imaging resolution. Dual-side view OCT (DSV-OCT) can be used to measure the lateral resolved thickness of opaque objects, and thus even of non-infiltrated leaves [34]. Compared to the dual confocal laser profiler [26], DSV-OCT also gives an image of the internal leaf morphology by fusing the images from both sides. However, it has the same disadvantages as the dual confocal laser profiler, namely, it is a custom-build complex setup and needs close access to both sides of the leaf.

Our OCT images have the potential for quantifying many more morphological features, such as individual cells and vascular bundles. Segmentation methods to extract such features from 3D confocal microscopy images [35–37] can be adapted for the use on OCT plant images. This may enable further quantification of plant

leaf morphology and dynamics. Moreover, our leaf thickness measurements can be applied to larger-scale plant studies. Those studies include imaging on whole leaves, comparing leaf thickness of different varieties, and longitudinal studies on the development of leaf thickness during plant growth. Hence, we foresee a great potential of our technique for quantification of 3D leaf morphology in digital phenotyping.

2.5. Conclusion

With this work, we show that water infiltration of plant leaves significantly improves the penetration depth and image quality for OCT plant imaging. With water infiltration, we imaged entire cross-sections of plant leaves, measured their refractive index, and successfully quantified the lateral resolved leaf thickness with high accuracy.

Data Availability

Data sets and analysis code is available at a Zenodo repository [38].

References

[1] D. K. Ray, N. D. Mueller, P. C. West, and J. A. Foley, *Yield trends are insufficient to double global crop production by 2050,* PLOS ONE **8**, e66428 (2013).

[2] F. Fiorani and U. Schurr, *Future scenarios for plant phenotyping,* Annual Review of Plant Biology **64**, 267 (2013).

[3] S. Dhondt, N. Wuyts, and D. Inzé, *Cell to whole-plant phenotyping: the best is yet to come,* Trends in Plant Science **18**, 428 (2013).

[4] N. Wuyts, J.-C. Palauqui, G. Conejero, J.-L. Verdeil, C. Granier, and C. Massonnet, *High-contrast three-dimensional imaging of the Arabidopsis leaf enables the analysis of cell dimensions in the epidermis and mesophyll,* Plant Methods **6**, 1 (2010).

[5] N. Wuyts, C. Massonnet, M. Dauzat, and C. Granier, *Structural assessment of the impact of environmental constraints on Arabidopsis thaliana leaf growth: a 3D approach,* Plant, Cell & Environment **35**, 1631 (2012).

[6] L. Remmler and A.-G. Rolland-Lagan, *Computational method for quantifying growth patterns at the adaxial leaf surface in three dimensions,* Plant Physiology **159**, 27 (2012).

[7] A. Walter, W. K. Silk, and U. Schurr, *Environmental effects on spatial and temporal patterns of leaf and root growth,* Annual Review of Plant Biology **60**, 279 (2009).

[8] S. Dhondt, H. Vanhaeren, D. Van Loo, V. Cnudde, and D. Inzé, *Plant structure visualization by high-resolution X-ray computed tomography,* Trends in Plant Science **15**, 419 (2010).

[9] L. Li, Q. Zhang, and D. Huang, *A review of imaging techniques for plant phenotyping,* Sensors **14**, 20078 (2014).

[10] D. Huang, E. A. Swanson, C. P. Lin, J. S. Schuman, W. G. Stinson, W. Chang, M. R. Hee, T. Flotte, K. Gregory, C. A. Puliafito, *et al.*, *Optical coherence tomography,* Science **254**, 1178 (1991).

[11] J. W. Hettinger, M. d. l. P. Mattozzi, W. R. Myers, M. E. Williams, A. Reeves, R. L. Parsons, R. C. Haskell, D. C. Petersen, R. Wang, and J. I. Medford, *Optical coherence microscopy. A technology for rapid, in vivo, non-destructive visualization of plants and plant cells,* Plant Physiology **123**, 3 (2000).

[12] A. Reeves, R. Parsons, J. Hettinger, and J. Medford, *In vivo three-dimensional imaging of plants with optical coherence microscopy,* Journal of Microscopy **208**, 177 (2002).

[13] M. Boccara, W. Schwartz, E. Guiot, G. Vidal, R. D. Paepe, A. Dubois, and A.-C. Boccara, *Early chloroplastic alterations analysed by optical coherence tomography during a harpin-induced hypersensitive response,* The Plant Journal **50**, 338 (2007).

[14] R. E. Wijesinghe, S.-Y. Lee, P. Kim, H.-Y. Jung, M. Jeon, and J. Kim, *Optical inspection and morphological analysis of diospyros kaki plant leaves for the detection of circular leaf spot disease,* Sensors **16**, 1282 (2016).

[15] R. E. Wijesinghe, S.-Y. Lee, N. K. Ravichandran, S. Han, H. Jeong, Y. Han, H.-Y. Jung, P. Kim, M. Jeon, and J. Kim, *Optical coherence tomography-integrated, wearable (backpack-type), compact diagnostic imaging modality for in situ leaf quality assessment,* Applied Optics **56**, D108 (2017).

[16] A. Rateria, M. Mohan, K. Mukhopadhyay, and R. Poddar, *Investigation of Puccinia triticina contagion on wheat leaves using swept source optical coherence tomography,* Optik **178**, 932 (2019).

[17] T. H. Chow, K. M. Tan, B. K. Ng, S. G. Razul, C. M. Tay, T. F. Chia, and W. T. Poh, *Diagnosis of virus infection in orchid plants with high-resolution optical coherence tomography,* Journal of Biomedical Optics **14**, 014006 (2009).

[18] T. Anna, S. Chakraborty, C.-Y. Cheng, V. Srivastava, A. Chiou, and W.-C. Kuo, *Elucidation of microstructural changes in leaves during senescence using spectral domain optical coherence tomography,* Scientific Reports **9**, 1167 (2019).

[19] C. J. Larimer, E. H. Denis, J. D. Suter, and J. J. Moran, *Optical coherence tomography imaging of plant root growth in soil,* Applied Optics **59**, 2474 (2020).

[20] M. Li, S. Landahl, A. R. East, P. Verboven, and L. A. Terry, *Optical coherence tomography—a review of the opportunities and challenges for postharvest quality evaluation,* Postharvest Biology and Technology **150**, 9 (2019).

[21] P.-C. Cheng, *Interaction of light with botanical specimens,* in *Handbook of Biological Confocal Microscopy*, edited by J. B. Pawley (Springer Science+Business Media, New York, 2006) 3rd ed., Chap. 21, pp. 414–441.

[22] G. R. Littlejohn, J. D. Gouveia, C. Edner, N. Smirnoff, and J. Love, *Perfluorodecalin enhances in vivo confocal microscopy resolution of Arabidopsis thaliana mesophyll,* New Phytologist , 1018 (2010).

[23] G. R. Littlejohn and J. Love, *A simple method for imaging Arabidopsis leaves using perfluorodecalin as an infiltrative imaging medium,* Journal of Visualized Experiments , e3394 (2012).

[24] P. J. De Wit and G. Spikman, *Evidence for the occurrence of race and cultivar-specific elicitors of necrosis in intercellular fluids of compatible interactions of Cladosporium fulvum and tomato,* Physiological Plant Pathology **21**, 1 (1982).

[25] J. Pfeifer, M. Mielewczik, M. Friedli, N. Kirchgessner, and A. Walter, *Non-destructive measurement of soybean leaf thickness via x-ray computed tomography allows the study of diel leaf growth rhythms in the third dimension,* Journal of Plant Research **131**, 111 (2018).

[26] V. Coneva, M. H. Frank, M. A. d. L. Balaguer, M. Li, R. Sozzani, and D. H. Chitwood, *Genetic architecture and molecular networks underlying leaf thickness in desert-adapted tomato Solanum pennellii,* Plant Physiology **175**, 376 (2017).

[27] J. Dupuis, C. Holst, and H. Kuhlmann, *Measuring leaf thickness with 3D close-up laser scanners: possible or not?* Journal of Imaging **3**, 22 (2017).

[28] M. Wojtkowski, V. J. Srinivasan, T. H. Ko, J. G. Fujimoto, A. Kowalczyk, and J. S. Duker, *Ultrahigh-resolution, high-speed, Fourier domain optical coherence tomography and methods for dispersion compensation,* Optics Express **12**, 2404 (2004).

[29] B. Baumann, C. W. Merkle, R. A. Leitgeb, M. Augustin, A. Wartak, M. Pircher, and C. K. Hitzenberger, *Signal averaging improves signal-to-noise in OCT images: But which approach works best, and when?* Biomedical Optics Express **10**, 5755 (2019).

[30] U. Bechtold, J. N. Ferguson, and P. M. Mullineaux, *To defend or to grow: lessons from arabidopsis c24,* Journal of Experimental Botany **69**, 2809 (2018).

[31] G. Tearney, M. Brezinski, J. Southern, B. Bouma, M. Hee, and J. Fujimoto, *Determination of the refractive index of highly scattering human tissue by optical coherence tomography,* Optics Letters **20**, 2258 (1995).

[32] J. Kalkman, A. V. Bykov, D. J. Faber, and T. G. van Leeuwen, *Multiple and dependent scattering effects in Doppler optical coherence tomography,* Optics Express **18**, 3883 (2010).

[33] K. F. Palmer and D. Williams, *Optical properties of water in the near infrared,* Journal of the Optical Society of America **64**, 1107 (1974).

[34] Q. Wu, X. Wang, L. Liu, and J. Mo, *Dual-side view optical coherence tomography for thickness measurement on opaque materials,* Optics Letters **45**, 832 (2020).

[35] T. Kawase, S. S. Sugano, T. Shimada, and I. Hara-Nishimura, *A direction-selective local-thresholding method, DSLT, in combination with a dye-based method for automated three-dimensional segmentation of cells and airspaces in developing leaves,* The Plant Journal **81**, 357 (2015).

[36] G. W. Bassel and R. S. Smith, *Quantifying morphogenesis in plants in 4D,* Current Opinion in Plant Biology **29**, 87 (2016).

[37] R. Fernandez, P. Das, V. Mirabet, E. Moscardi, J. Traas, J. L. Verdeil, G. Malandain, and C. Godin, *Imaging plant growth in 4D: Robust tissue reconstruction and lineaging at cell resolution,* Nature Methods **7**, 547 (2010).

[38] J. de Wit, S. Tonn, G. Van den Ackerveken, and J. Kalkman, *Quantification of plant morphology and leaf thickness with optical coherence tomography,* https://doi.org/10.5281/zenodo.4059559 (2022).

3

Fast and accurate spectral-estimation axial super-resolution optical coherence tomography

Spectral-estimation OCT (SE-OCT) is a computational method to enhance the axial resolution beyond the traditional bandwidth limit. However, it has not yet been used widely due to its high computational load, dependency on user-optimized parameters, and inaccuracy in intensity reconstruction. In this study, we implement SE-OCT using a fast implementation of the iterative adaptive approach (IAA). This non-parametric spectral estimation method is optimized for use on OCT data. Both in simulations and experiments we show an axial resolution improvement with a factor between 2 and 10 compared to standard discrete Fourier transform. Contrary to parametric methods, IAA gives consistent peak intensity and speckle statistics. Using a recursive and fast reconstruction scheme the computation time is brought to the sub-second level for a 2D scan. Our work shows that SE-OCT can be used for volumetric OCT imaging in a reasonable computation time, thus paving the way for wide-scale implementation of super-resolution OCT.

This chapter has been published as: **Jos de Wit**, Kostas Angelopoulos, Jeroen Kalkman, and George-Othon Glentis, *Fast and accurate spectral-estimation axial super-resolution optical coherence tomography*, Optics Express 29, 39946-39966 (2021)

3.1. Introduction

Since its first introduction in 1991 [1], optical coherence tomography (OCT) has been developed towards an effective and widely used method for high resolution non-invasive, non-contact and label-free imaging of tissues, fluids, and other scattering media. Especially the introduction of Fourier domain OCT (FD-OCT) with its superior signal-to-noise ratio (SNR) has accelerated the application of OCT imaging as it enables real-time imaging with high resolution and high frame-rate. Currently, it is an established modality in medical imaging [2], and is also applied in other fields such as material science [3, 4], artwork examination [5, 6] and plant imaging [7].

For imaging small details, the spatial resolution of the imaging system is one of the most crucial aspects. Improving resolution enables imaging of smaller sample structures and more accurate quantification of sample morphology. In OCT, the resolution in the lateral and the axial direction are decoupled. While the lateral resolution depends on the focusing optics and the wavelength, the axial resolution is determined by the temporal coherence of the light source, which is inversely proportional to the source bandwidth. Therefore, improving the lateral and axial resolution require a different approach and are thus often treated separately. In the current work, we focus on improvement of the axial resolution.

In FD-OCT, the sample reflectivity profile along a scan line is usually estimated from the inverse discrete Fourier transform (DFT) of the spectrum, i.e., the interference spectrum and the reflectivity profile form a Fourier transform pair. This limits the (amplitude based) axial resolution to the coherence length of the source, which, for a Gaussian spectrum depends on the center wavelength λ_c and source bandwidth $\Delta\lambda$ as $l_c = \frac{2\ln 2}{\pi}\frac{\lambda_c^2}{\Delta\lambda}$. Therefore, OCT setups have been developed using light sources with an ultra-broad bandwidth of up to 200 nm operating at wavelengths typically around 800 nm. Using these approaches axial resolutions up to about a single µm have been achieved [8, 9]. However, light sources with an ultra-broad bandwidth are not only difficult to build, their implementation also complicates the optical design of the OCT system. For swept-source OCT (SS-OCT), the source bandwidths are limited due to the limited bandwidth of gain materials and complexity of combining different gain materials [10]. For large bandwidth spectral domain OCT (SD-OCT) the spectrometer performance is the bottleneck, giving a significant intensity roll-off even when properly designed. Moreover, for any ultra-large bandwidth OCT system chromatic aberrations, sample induced dispersion, and wavelength-dependent scattering properties can be hard to compensate for. Another strategy to improve the axial resolution is to use short wavelengths reaching into the visible light range [11]. However, in the blue to green wavelength light range, available superluminescent diodes (SLDs) have a narrow bandwidth and ultra-high resolution cannot be achieved. Therefore, there is a need to overcome this traditional resolution limitation and provide a high axial resolution with a limited source bandwidth.

Early computational methods for improving the axial resolution of OCT were based on classic deconvolution techniques [12, 13], with the Wiener filtering and the Lucy-Richardson method being the most notable examples, [14–17]. However,

the improvement in the axial resolution achieved by those methods is either limited or obtained at the cost of side effects such as side-lobe or noise enhancement. A significant improvement in axial resolution was obtained with modulated deconvolution [18]. However, this method requires careful calibration of multiple kernels.

High-resolution spectral estimation (SE) techniques, that originate from the field of radar and telecommunication signal processing [19–23] have been used to improve the axial resolution in OCT by using reconstruction methods alternative to the discrete Fourier transform. The frequencies of the interferograms that are measured in FD-OCT correspond to depths of reflection. SE techniques estimate these frequencies with much higher precision than what can be obtained with the conventional DFT, thus effectively improving the axial resolution. Moreover, resolution improvement goes together with excellent side-lobe suppression, yielding high-quality images. Spectral Estimation OCT (SE-OCT) has been able to obtain an improvement in axial resolution with a factor up to 4.7 [21].

Although SE-OCT has shown promising results, there are at least three major limitations that obstruct its usage in the mentioned application areas: the large computational costs, the dependency on user-optimized parameters, and the inaccuracy in reconstructed intensity. Widescale application of SE-OCT techniques would require close to real-time B-scan processing, something that is currently not achieved. Based on reported running time and on the timing of shared code, typical computation times for a single B-scan range from several minutes [21, 22] to even hours [23]. Parametric methods only yield accurate results when the model sufficiently fits the data and parameters are well chosen. Optimal parameters often depend on the OCT setup and imaged sample, thus requiring tedious parameters optimization for each new application [19, 22]. Even for optimized parameters, misfits between the model and data can cause image artifacts in the results. For example, with the auto-regressive (AR) method, as proposed by Liu et al. [21], the estimated signal intensity is fluctuating and not proportional to the true intensity of back-scattered light, and spurious peaks appear in the images when a high model order is chosen. Similar problems are observed with the maximum entropy method [19] and the Prony method [20]. Other applied SE methods assume a high level of sparsity, thus only yielding accurate results for relative sparse samples [20, 23].

Non-parametric methods based on data-adaptive filter-banks, such as Capon [24], Amplitude and Phase EStimation (APES) [25] and the more recent Iterative Adaptive Approach (IAA) [26] form an attractive alternative for parametric spectral estimation methods [27]. These non-parametric methods provide spectral estimations with high resolution and strong suppression of side-lobes. Motivated by the recent advances in non-parametric high-resolution spectral analysis, we propose the use of IAA [26] for the improvement of the axial resolution and image quality in the SD-OCT imaging while avoiding the mentioned limitations of computation costs, dependency on model parameters, and image artifacts. As a non-parametric method, IAA does not require the data to be described by a parametric model, so it does not suffer from a model-data misfit. The computation cost is strongly reduced by using our earlier developed computationally efficient implementation of IAA [28, 29].

Additionally, we further reduce computation cost by implementing this algorithm recursively in the lateral direction [30] and limiting the axial reconstruction range to the region of interest, yielding sub-second reconstruction times for a B-scan. With this computational efficient IAA, we aim to make SE-OCT applicable to improve axial resolution in the many application areas where physical accuracy and reconstruction speed are necessary.

3.2. Theory

3.2.1. The Fourier-domain OCT signal model

The OCT interference signal, i.e., the signal with the constant reference intensity (DC) term, auto-correlation terms, and constant pre-factors omitted, is in Fourier-domain OCT described as [31]

$$I(k) = S_0(k) \int_{-\infty}^{\infty} \left(a(z) \mathrm{e}^{-i2kz} + a^*(z) \mathrm{e}^{+i2kz} \right) \mathrm{d}z, \tag{3.1}$$

where $I(k)$ is the interference intensity as function of wavenumber $k = 2\pi/\lambda$, $S_0(k)$ is the source intensity spectrum and $a(z)$ is the reflectivity at depth z, which is the single pass depth measured from the zero-delay position. The expression can be rewritten to

$$I(k) = S_0(k) \int_{-\infty}^{\infty} \tilde{a}(z) \mathrm{e}^{-i2kz} \mathrm{d}z, \tag{3.2}$$

where $\tilde{a}(z) = a(z) + a^*(-z)$, is the symmetric reflectivity function. The integral can be interpreted as the Fourier transform of $\tilde{a}(z)$, hence the reconstruction of $\tilde{a}(z)$ could be interpreted as an estimation of the frequency spectrum of $I(k)/S_0(k)$. This reconstruction is commonly obtained using an inverse Fourier transform of $I(k)$ as shown in Fig. 3.1(a), leading to a convolution of the true reflectivity $\tilde{a}(z)$ with the inverse Fourier transform of $S_0(k)$, which thus acts as an axial point spread function (PSF).

To set-up the OCT imaging process in the discrete domain we consider the interference signal measured at N discrete wavenumbers k_n, where N is normally the number of pixels on the spectrometer camera. Spectrally normalizing this discrete interference signal results in an $N \times 1$ data vector $\mathbf{y}$, with elements $y_n = I(k_n)/S_0(k_n)$ [20, 21]. The depth z can be discretized to M uniformly spaced depth locations as

$$z_m = \begin{cases} 2z_{\max}\frac{m}{M}, & 0 \le m < \frac{M}{2} \\ -2z_{\max}\frac{M-m}{M}, & \frac{M}{2} \le m \le M-1 \end{cases},$$

where $z_{\max} = \pi/(2 \cdot \delta_k)$ follows from the sampling interval δ_k. Denoting the discretized reflectivity $a(m) = \tilde{a}(z_m)$, we can write the data vector of the OCT spectrum $\mathbf{y}$ as

$$\mathbf{y} \approx \sum_{m=0}^{M-1} a(m)\mathbf{f}_m + \eta, \tag{3.3}$$

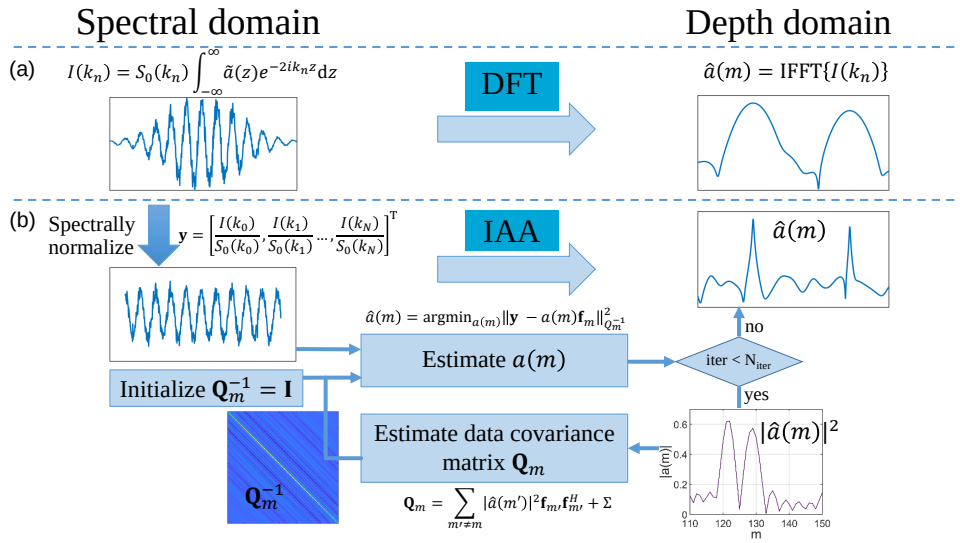

Figure 3.1: Overview of OCT reconstruction with (a) the conventional DFT-based approach and (b) the iterative adaptive approach (IAA).

where η is an $N \times 1$ noise vector, and

$$\mathbf{f}_m \triangleq \left[\, 1 \;\; \mathrm{e}^{-i\frac{2\pi m}{M}} \;\; \ldots \;\; \mathrm{e}^{-i\frac{2\pi m}{M}(N-1)} \,\right]^T \tag{3.4}$$

is an $N \times 1$ vector with corresponding Fourier components. Superscript $(.)^T$ stands for the transpose operator.
For negligible or uncorrelated (white) noise η, $a(m)$ can be estimated as the solution of a least squares data fitting problem of the form [27]

$$\hat{a}(m) = \mathrm{argmin}_{\hat{a}(m)}\|\mathbf{y} - \hat{a}(m)\mathbf{f}_m\|^2, \quad m = 0, 1, \ldots, M-1, \tag{3.5}$$

with $\|.\|^2$ denoting the $\ell 2$-norm. The solutions $\hat{a}(m)$ of Eq. 3.5 are given by the inverse DFT of $\mathbf{y}$, increased in spatial sampling by zero-padding $\mathbf{y}$ when $M > N$. This is the regular OCT reconstruction method as indicated in Fig. 3.1(a), with an additional spectrum normalization. Spectral reshaping with a smoother window may be applied prior to DFT to reduce side-lobes at the cost of axial resolution. Hereafter, for reasons of simplicity, we drop out the $\hat{(.)}$ symbol from variables that represent estimators, thus $a(m)$ means an estimate of the sought variable.

3.2.2. Iterative adaptive approach method

The iterative adaptive approach (IAA) is a high-resolution, non-parametric spectral estimation method [26, 32], proposed in the area of radar signal processing. Figure 3.1(b) gives a schematic overview of OCT reconstruction with IAA. The reflectivity $a(m)$ is estimated with a weighted least square reformulation of Eq. 3.5

$$a(m) = \mathrm{argmin}_{a(m)}\|\mathbf{y} - a(m)\mathbf{f}_m\|^2_{\mathbf{Q}_m^{-1}}, \quad m = 0, 1, \ldots, M-1, \tag{3.6}$$

where the weighting on a vector $\mathbf{u}$ is defined as $\|\mathbf{u}\|^2_{\mathbf{Q}_m^{-1}} \triangleq \mathbf{u}^T\mathbf{Q}_m^{-1}\mathbf{u}$, resulting in the solution

$$a(m) = \frac{\mathbf{f}_m^H\mathbf{Q}_m^{-1}\mathbf{y}}{\mathbf{f}_m^H\mathbf{Q}_m^{-1}\mathbf{f}_m}, \quad m = 0, 1, \dots, M-1\,. \tag{3.7}$$

As shown in Figure 3.1, $\mathbf{Q}_m^{-1}$ is initialized as the identity matrix $\mathbf{I}_N$, which gives the same result as the DFT with zero-padding. Subsequently, the $N \times N$ matrix $\mathbf{Q}_m$ is calculated based on the estimate of $a(m)$ as

$$\mathbf{Q}_m = \mathbf{R} - |a(m)|^2\mathbf{f}_m\mathbf{f}_m^H\,. \tag{3.8}$$

with $(.)^H$ standing for the Hermitian transpose (transpose and conjugate). Matrix $\mathbf{R}$ is an estimate of the data covariance matrix, $\mathbf{R} \triangleq \mathbb{E}\left(\mathbf{y}\mathbf{y}^H\right)$, where $\mathbb{E}(.)$ denotes mathematical expectation. Using Eq. 3.3 and assuming independence between data and noise, $\mathbf{R}$ can be estimated as

$$\mathbf{R} = \sum_{m=0}^{M-1} |a(m)|^2\mathbf{f}_m\mathbf{f}_m^H + \Sigma\,, \tag{3.9}$$

where $\Sigma \triangleq \mathbb{E}(\eta\eta^H) \succeq 0$ denotes the covariance of the noise η.

The matrix $\mathbf{Q}_m$ has a strong weight for signals from depths that have a high amplitude ($\left|a(m)\right|^2$), except for the estimated depth m, whose contribution is subtracted in Eq. 3.8. Weighting with the inverse of $\mathbf{Q}_m$ thus suppresses the contribution from high-intensity peaks at locations not identical to the estimated signal at location m. Thus, side-lobes and edges of the main lobe are suppressed, while the signal that belongs precisely to the location m is passed nearly undisturbed. This results in narrow peaks with limited side-lobes and thus in a high-resolution OCT reflectivity profile $a(m)$. Both $a(m)$ and $\mathbf{Q}_m^{-1}$ are further refined during subsequent iterations [26].

Use of $\mathbf{Q}_m$ in Eq. 3.7 results in a considerable computational overload because $\mathbf{Q}_m^{-1}$ has to be calculated for every m. Fortunately this can be avoided by the introduction of

$$a(m) = \frac{\mathbf{f}_m^H\mathbf{R}^{-1}\mathbf{y}}{\mathbf{f}_m^H\mathbf{R}^{-1}\mathbf{f}_m}, \quad m = 0, 1, \dots, M-1\,, \tag{3.10}$$

which is algebraically equivalent as can be readily shown using using the Matrix Inversion Lemma [27], see also [26]. This is crucial as in Eq. 3.10 $\mathbf{R}$ is independent of depth coordinate m, thus avoiding the computationally cumbersome need to invert $\mathbf{Q}_m$ for each depth coordinate m.

The noise covariance matrix Σ that appears in Eq. 3.9 has to be estimated from the given data. A common assumption is that Σ is a diagonal matrix with (non-negative) elements $\sigma^2(n), n = 1, \dots, N$. These can easily be estimated, in a scheme similar to Eq. 3.10, as

$$\sigma^2(n) = \left|\frac{\mathbf{e}_n^T\mathbf{R}^{-1}\mathbf{y}}{\mathbf{e}_n^T\mathbf{R}^{-1}\mathbf{e}_n}\right|^2, \quad n = 1, \dots, N\,, \tag{3.11}$$

with $\mathbf{e}_n$, $n = 1, 2, \ldots, N$ denoting the n-th column of the $N \times N$ identity matrix $\mathbf{I}_N$. Variables $\sigma^2(n)$, $n = 1, \ldots, N$ may be interpreted as the variance of each noise component in Eq. 3.3. In this work we assume equal variance for all noise components, equal to the average of $\sigma^2(n)$, i.e.,

$$\Sigma = \sigma^2 \mathbf{I}, \quad \sigma^2 = \frac{1}{N} \sum_{n=1}^{N} \sigma^2(n) \,. \tag{3.12}$$

The IAA estimator is obtained by iterating Eq. 3.9 and Eq. 3.10 until convergence. About 10 iterations are usually required for convergence, see also [26, 32, 33]. The algorithm is summarized in Appendix 3.7.

3.2.3. Brute force IAA

When implementing IAA in a *brute force* way, i.e., by direct use of Eqs. 3.9, 3.10, 3.11 and 3.12, without taking into account the underlying structure of the pertinent matrices and variables, the overall computational complexity denoted with $\mathcal{C}$ is approximately given by

$$\mathcal{C}^{BF}(N, M, q_i) = \mathcal{O}\left(q_i \left(2N^2 M + N^3\right)\right), \tag{3.13}$$

with q_i denoting the number of the applied IAA iterations. This comprises first the calculation of the covariance matrix $\mathbf{R}$ by means of the sum of weighted outer vector products (Eq. 3.9, $\mathcal{O}\left(N^2 M\right)$), next the inversion of the covariance matrix $\mathbf{R}$ ($\mathcal{O}\left(N^3\right)$) using a standard linear system solver, i.e., Cholosky's decomposition followed by back substitution, and, thirdly, the dyadic product in Eq. 3.10 ($\mathcal{O}\left(N^2 M\right)$). All these elements are repeated for each iteration (the factor q_i). The brute force IAA implementation is summarized in Appendix 3.7.

3.2.4. Fast IAA

The computational complexity can be significantly reduced by taking into account the particular properties of the variables resulting from the Fourier vectors (Eq. 3.4) [28, 29, 34]. As we assume the noise variances to be equal, i.e., $\Sigma = \sigma^2 \mathbf{I}$, the interference covariance matrix $\mathbf{R}$ is a Hermitian Toeplitz matrix, which instead of using Eq. 3.9, can be efficiently estimated by means of Toeplitz to Circulant matrix embedding in $\mathcal{O}\left(M \log_2(M)\right)$ operations [28]. Taking into account the special structure (the low displacement rank) of a Toeplitz matrix, $\mathbf{R}^{-1}$ can be implicitly estimated by means of the Gohberg-Semencul (GS) factorization and the use of the Levinson-Durbin algorithm [27]. Using the GS factorization of $\mathbf{R}^{-1}$, the elements in Eq. 3.10 and the noise variance elements $\sigma^2(n)$, Eq. 3.11, are computed using the FFT as the computational engine. This gives an overall computational complexity of approximately [28, 29, 34]

$$\mathcal{C}^{F}(N, M, q_i) = \mathcal{O}\left(q_i \left(N^2 + \gamma N \log_2 N + 1.5 M \log_2 M\right)\right), \tag{3.14}$$

where parameter γ is a number that depends upon the particular implementation details of the several Toeplitz vector products that are required by the method

(e.g. $\gamma = 12$ was reported in [28]). Compared with the brute force implementation (Eq. 3.13), the reduction in complexity is more than a factor N as Eq. 3.14 has terms N^2 rather than N^3 and $1.5M\log_2 M$ rather than N^2M. M is typically a factor 8-32 higher than N, leaving $\log_2 M$ still significantly below N. The extra term $\gamma N \log_2 N$ is less significant than the other two, as $N \ll \log_2 N$ and $M > N$.

3.2.5. Recursive scheme for B-scan processing (RFIAA)

B-scan OCT imaging is performed by processing N_B consecutive A-scans as columns in an image matrix. The columns are usually processed independently to produce the corresponding sequence of depth profiles, eventually combined to an OCT B-scan image. Obviously, the computational cost for processing a B-scan using the IAA method for independent A-line processing is given by

$$\mathcal{C}_{Bscan}\,(N_B, N, M, q_i) = N_B\ \mathcal{C}_{Ascan}\,(N, M, q_i) \tag{3.15}$$

with $\mathcal{C}_{Ascan}\,(N, M, q_i)$ depending upon the particular IAA implementation. As most imaged samples are slowly varying in the lateral direction, and particularly when the lateral sampling distance is around or below the lateral OCT resolution, it is expected that successive A-lines have resemblance to each other. This fact can be taken into account in the application of the IAA algorithm on the B-scan data set since upon convergence only a small variation between the data covariance $\mathbf{R}$ of successively processed A-scans is expected. Thus an efficient iterative updating procedure can be applied [30], where the data covariance of the previously processed A-scan is used for an initialization close to the convergence value of the currently processed A-scan, thereby reducing the required amount of iteration from q_i to $q_{rci} < q_i$. The computational complexity of the recursive IAA (RIAA) scheme is

$$\mathcal{C}_{R-Bscan}\,(N_B, N, M, q_i, q_{rci}) \approx N_B\ \mathcal{C}_{Ascan}\,(N, M, q_{rci})\ , \tag{3.16}$$

where the approximation is valid since $q_i \ll N_B$, noting that $q_{rci} \leq q_i$. In the recursive implementation, usually one or two iterations are enough to get results comparable to those obtained by the non-recursive approach. Compared to the standard IAA schemes where about $q_i = 10$ iterations are required for convergence, the RIAA offers a significant reduction as it needs about 5 or 10 times fewer computations typically using $q_{rci} = 1 - 2$.

In the most efficient algorithm, RIAA is implemented based on the FIAA method, resulting in the recursive fast IAA (RFIAA) method. The recursive scheme is made compatible for parallel processing by dividing the B-scan into data chunks according to the number of available CPU cores. For each chunk, the first column is initialized with q_i iterations, and subsequent columns are iterated q_{rci} times after the proposed initialization close to convergence. As the number of cores is usually much smaller than N_B, the computation complexity is not significantly affected and still follows Eq. 3.15. However, this implementation makes RFIAA applicable with parallel processing with multiple cores which results in significant computation time reduction.

3.2.6. Reduction of reconstruction range

The standard FD-OCT reconstruction implies a 50% redundancy in the estimated depth profiles as the mirror image (with negative z-values) is usually rejected, keeping only the values for the positive depth range. Moreover, due to the presence of auto-correlation artifacts and limited imaging depth, the depth range that contains useful sample information is usually even smaller.

We increase the efficiency of the OCT reconstruction with IAA by restricting the reconstruction to a useful depth range Δz. This reduces the reconstruction grid length M with a factor $1/R = \Delta z/(2z_{\max}) \leq 0.5$. Limiting the reconstruction depth range also allows for reduction of the input interference spectrum length N such that it only includes the frequencies that contribute to the useful range. This is implemented by shifting the useful depth range to the region centered at $z = 0$ using the modulation property of the DFT, followed by low-pass filtering and down-sampling at the rate $1/R_s$, where $R_s = \lfloor R \rfloor$ is the integer value operator. This reduction is most efficient when R is an integer that equals a power of 2. The computational gain due to range reduction is a factor $\mathcal{O}\left(R^2\right)$ or $\mathcal{O}\left(R\left(1+\log_2\left(R/M\right)\right)\right)$, depending on whether the first or the last term in Eq. 3.14 is predominant.

3.3. Methods

3.3.1. Experimental setup

The measurements were performed with a commercial spectral-domain OCT system (Ganymede-II-HR, Thorlabs, Germany). The light source consists of two coupled super-luminescent diodes that are combined in a spectrum with a central wavelength of 900 nm and a full width half maximum (FWHM) of 120 nm. The FWHM of the axial intensity point spread function (PSF) was experimentally measured to be 3.0 µm in air, which corresponds to 2.2 µm in tissue. The spectrometer has 2048 pixels covering a 220 nm bandwidth, giving an axial imaging range of 1.87 mm. The intensity lateral PSF was experimentally determined with a knife-edge step response to have a FWHM of 6 µm in focus. The spectral raw data was acquired using ThorImage software (version 5.2.0) and further processed in MATLAB (R2020a).

3.3.2. OCT sample imaging

Experimental OCT data was obtained from a wedge phantom, a layered interface phantom, an onion sample, and finger skin tissue.

The wedge phantom represents a sparse object that is ideal to study the ability to resolve two closely separated reflectors. The air wedge was constructed by placing a coverslip on a microscope glass; it was tilted by placing a piece of tape between them at one end. A neutral density filter (NE20A-B, Thorlabs, Germany) was placed between the lens and the wedge phantom to circumvent detector saturation, and the wedge was placed in a depth region without auto-correlation artifacts. The position of the two wedge interfaces was determined by a two-peak Gaussian fit on the FBW-DFT A-scans in the region where the interfaces were well resolved. The interface location was extrapolated using a quadratic fit to the region where the two interfaces were not well resolved. This extrapolation served as the ground truth to

determine the separation of the interfaces.

The layered interface phantom was used to study intensity fluctuations at different SNRs. It consisted of two coverslips on a microscope glass. The coverslips were spaced by a layer of tape at their edges and the space was filled with ethanol to create both air-glass and ethanol-glass interfaces with different intensities and SNRs. The phantom was placed out of focus to avoid detector saturation.

To test IAA on medium sparse objects, a slice of an onion was imaged. Onion cells are typically 50-100 µm high and have clear boundaries that consist of two closely separated interfaces, which are typically 6-10 µm separated [18]. Thus, these layers can only be resolved with a high axial resolution. First, a cross-sectional image was taken that contains 1024 scan lines over a range of 3 mm, giving a lateral spacing of 2.9 µm between the scan lines. Second, a volume data set was obtained of 512×512 scan lines, covering 2.5×2.5 mm^2. With the volume scan, 8 spectra were acquired per lateral position, which were averaged before further processing to increase SNR.

IAA was tested on a non-sparse sample by imaging skin tissue from the fingertip. The dense skin tissue has a low level of sparsity and is a good sample to evaluate the performance of the methods on reconstruction quality and contrast in the context of medical imaging. The B-scan comprises 2048 lines over a lateral range of 8.1 mm, giving a lateral spacing of 3.9 µm between subsequent scan lines. The contrast to noise ratio (CNR) was calculated as

$$CNR = \frac{|\mu_s - \mu_n|}{\sqrt{\sigma_s^2 + \sigma_n^2}}, \tag{3.17}$$

where μ and σ^2 were the mean and variance of the speckle $((.)_s)$ and noise $((.)_n)$ region respectively. Also an OCT volume data set of skin tissue was obtained with 128×128 scan lines over an area of 0.8×0.8 mm^2, with 8 spectra per scan line for spectral averaging.

Finally, contrast and speckle statistics was quantified using an Intralipid suspension (Fresenius-Kabi) diluted to 2.5 weight%. A droplet of the suspension was placed under a microscope coverslip to create a flat top surface, which was aligned to be horizontal in lateral scan direction. A B-scan of 1024 scan-lines was recorded over a lateral range of 3 mm. The depth dependent intensity due to confocal PSF, roll-off and attenuation [35] was compensated for by dividing the OCT intensity of the Intralipid region by the laterally averaged intensity of this region, thus creating a homogeneous scattering region.

3.3.3. OCT data simulations

OCT data was simulated to study the resolution, intensity preservation, and contrast in RFIAA reconstruction. The simulated spectra were based on a 1D OCT model [31]

$$I(k_i) = S_0(k_i)\left|1 + \sum_j a_j e^{i2kz_j}\right|^2 + \eta(k_i), \tag{3.18}$$

where $S_0(k_i)$ is the experimental source spectrum (see Fig. 3.2(a)) for discrete wavenumber k_i, $a_j \ll 1$ is the amplitude of reflector j at depth z_j and $\eta(k_i)$ is Gaussian noise with a standard deviation proportional to $\sqrt{S_0(k_i)}$. The terms within the bracket corresponds to respectively the reference and the sample field.

For the resolution study, a wedge was simulated as two reflectors with an equal amplitude and a spacing $z_2 - z_1$ ranging from 0 to 29 µm over 1024 A-scans. The simulated object for studying intensity preservation consisted of 8 horizontal interfaces with halved amplitude (-6 dB intensity drop) for each subsequent interface. For studying contrast and speckle statistics, 3 speckle regions with different mean intensity were simulated. The spectrum from a speckle region was simulated by taking 2048 reflectors with equal amplitude a_j located at random depths z_j (uniform probability distribution) over a 150 µm depth range. The signal from these sub-resolution reflectors added up coherently, creating a 1D speckle pattern. The amplitudes a_j were halved for each subsequent region. The position of the reflectors in subsequent A-scans was independent, so the effect of finite lateral resolution is not taken into account.

3.3.4. OCT data processing

Pre-processing of the spectral data consisted of three steps: subtracting the reference arm OCT spectrum, interpolating the data on a grid that is linear in the wavenumber domain, and multiplying with a phase vector to compensate for dispersion mismatch. The dispersion was corrected for with a fourth-order polynomial, whose coefficients are determined from a reference measurement with a single mirror as reflector [36]. After the generic pre-processing, the data were further processed according to four different methods:

1. Full bandwidth-DFT (FBW-DFT)

This is the DFT reconstruction of the full bandwidth signal and acts as a ground-truth image. The interference spectra were Gaussian reshaped to suppress side-lobes [37], as shown in Figure 3.2 (a). To avoid noise amplification, the edges

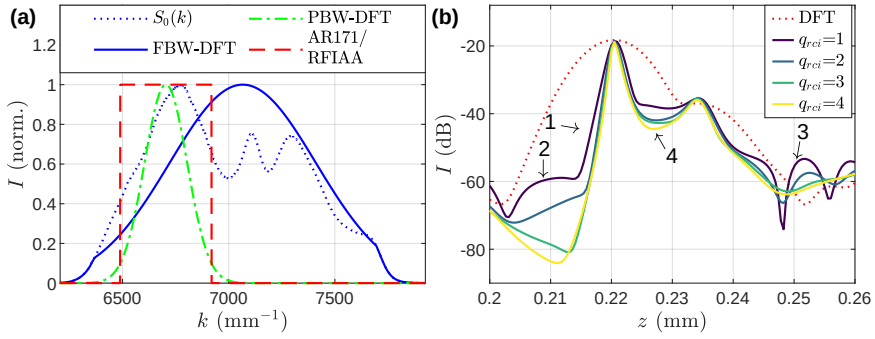

Figure 3.2: (a) The original source spectrum and the reshaped spectra for each of the four methods. (b) A typical zoom in A-scan obtained with RFIAA for different q_{rci}.

the spectrum were not reshaped but followed the original source spectrum. The FWHM of the corresponding bandwidth-limited axial PSF is 2.7 µm. The OCT depth information was obtained by taking the inverse DFT of the reshaped spectral data, with zero padding to obtain a grid spacing that is equal to that of the RFIAA reconstruction.

2. Partial bandwidth-DFT (PBW-DFT)

This is the DFT reconstruction of a partial bandwidth interference spectrum that is obtained by reshaping the spectrum with a narrow Gaussian window. The spectral interval was chosen around the high-intensity peak on the left side of the original spectrum, as indicated in Figure 3.2. This ensured that the majority of the signal comes from a single SLED, thus avoiding non-uniform modulation in the region where the spectra of different SLEDs overlap. Non-uniform modulation can be caused by polarization mismatch between the SLEDs, thereby degrading the axial resolution [38] and potentially affecting the spectral estimation result. As low-intensity spectrum tails have insufficient SNR for spectral estimation [21] but help in side-lobe reduction for DFT reconstruction, we chose the Gaussian window for PBW-DFT to have a relative intensity of 10% at the edges of the window that is used for the spectral estimation methods and extend it to outside this domain, as shown in Figure 3.2. The FWHM of the corresponding bandwidth-limited axial PSF is 8.3 µm. The reshaped spectral data was zero-padded before taking the inverse DFT to obtain a grid spacing equal to that of the RFIAA reconstruction.

3. Auto-regression filter (AR171)

This is the auto-regressive reconstruction on a spectrally normalized truncated part of the bandwidth that covers a quarter of the spectrometer bandwidth, identical to the bandwidth of the PBW-DFT except for the low intensity edges, as indicated in figure 3.2. The AR parameters were estimated using the modified covariance method and the model order was set to 171, corresponding to a third of the data pixel length as proposed by Liu et al. [21]. The DFT-based axial PSF of the corresponding rectangular source spectrum has a FWHM of 6.5 µm.

4. Recursive Fast IAA (RFIAA)

This is the proposed RFIAA spectral estimation OCT on the truncated part of the total bandwidth (same part as for AR171). The spectral data is spectrally normalized before using it in the RFIAA algorithm, resulting in a DFT-based axial PSF with a 6.5 µm FWHM.

The number of iterations q_i of the first scan line was set to 10, which was sufficient to obtain convergence. The value of q_{rci} was chosen based on a test with a reconstructed A-line for different q_{rci} of the onion sample, shown in Figure 3.2(b). A value of $q_{rci} = 2$ already gives significant side-lobe reduction (1-3) and deeper valleys (4) over $q_{rci} = 1$. The further effect of increasing q_{rci} beyond $q_{rci} = 2$ is limited. Hence, we chose $q_{rci} = 2$. The RFIAA upsampling factor M/N (for full range reconstruction) was chosen to be 64 for the wedge and simulation images to achieve an optimal evaluation of the performance, especially for high SNRs that give a high resolution. For the onion and skin sample, $M/N = 16$ was chosen for fast

computation and good image quality. The reduced reconstruction depth range for all objects covered half the positive z-range (downsampling factor $R = 4$) centered around region of interest.

For all four methods, the intensity of the OCT signal is used for further analysis. For visualization, the intensity is log compressed and the lower limit of the dynamic range is determined by fitting a Rayleigh distribution on the histogram of amplitudes of a custom selected noise region in the image, as described by Steiner et al. [39] (using $\tau = 0.95$).

All data processing was implemented as MATLAB scripts (version R2020a) using its intrinsic functions. FIAA implementation is taking advantage of the `levinson.m` intrinsic function, which is actually implemented as a mex file bundled in the MATLAB programming environment. No further attempt for speeding up the running time using MATLAB's compiler capabilities nor any direct C-code programming has been applied. The AR modified covariance estimator, which is required in the approach proposed in [21], is implemented using `armcov.m` intrinsic function. This is a plain, brute force implementation of the AR modified covariance estimator, offering some intrinsic parallel processing capabilities due to the use of the available BLAS3 routines. All code was executed on a Dell Precision 5820 with an Intel Xeon W-2223 CPU and 32 GB RAM. The B-scan was cut in 4 equal-sized sub-images for parallel processing on the 4 CPU cores, as discussed in 3.2.5. AR reconstruction was applied in parallel on scan line level.

3.4. Results

3.4.1. Sparse wedge object

Figure 3.3 shows the imaging results of the wedge phantom obtained with the different methods. The two interfaces of the wedge are clearly visible (figure 3.3(a-d)). The FBW-DFT image shows a beating pattern at the location where the interfaces approach each other. This effect becomes a lot more pronounced when the bandwidth is reduced with PBW-DFT. This beating pattern is caused by coherent addition of the reflection of both interfaces, and further influenced by spectral leakage in DFT reconstruction [40]. For PBW-DFT, the beating pattern strongly reduces the resolvability of the two interfaces and is an indication of the lower axial resolution. Using the same bandwidth as with PBW-DFT, the two spectral estimation methods reconstruct the two wedge interfaces as narrow lines and largely eliminate the beating pattern. AR171 gives the most narrow representation of the interface, which appears relatively dark due to strong variation of peak intensities caused by the AR reconstruction. This variation required the dynamic range of the image color scale to be extended to 55 dB. Where the interfaces approach each other, vertical stripe artifacts appear and the interfaces become ill-defined. Though RFIAA gives a slightly less narrow representation of the interface than AR171, the intensity of the interfaces are more constant. Still the improvement with respect to PBW-DFT is very clear and the interfaces are imaged narrower than FBW-DFT that uses a four times larger bandwidth. Towards the left of the image, the interfaces melt together in a beating pattern, and some stripe artifacts are visible.

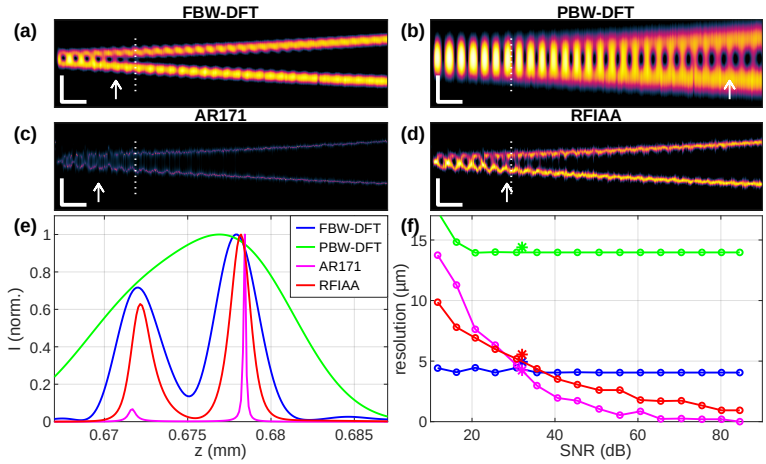

Figure 3.3: (a-d) Experimental OCT images of the wedge phantom. The SNR is 32 dB, and the dynamic range is 15 dB (a,b,d) or 55 dB (c). Scale bars indicate 10 μm vertical and 100 μm horizontal. The arrows indicate the widest separation where the surfaces are not resolved. (e) Cross section of the OCT intensity at the white dotted line in (a-d). (f) The resolution as a function of SNR based on simulations (solid line). The experimental values are indicated with the star.

The cross sections in Figure 3.3(e) further illustrate the described effects. PBW-DFT gives a broad peak from the merged interfaces. AR171 gives narrow peaks, but the intensity of the first interface is less than 10% of the second interface which does not resemble the true relative intensity as obtained with FBW-DFT. This effect is clearly a disadvantage of AR reconstruction [21] and will be explored further in the next section. RFIAA gives peaks that are about the same height and a bit narrower than FBW-DFT.

The OCT axial resolution was quantified as the widest spacing at the edge where the interfaces first merge for two successive A-scans. The two interfaces are considered to merge when the valley between the peaks is less than a factor 0.5 (3 dB) below the lowest peak intensity. The arrows in Figure 3.3(a-d) indicate the resolution limit for the shown images, at a spacing of 4.9 μm, 14.4 μm, 4.2 μm and 5.5 μm for FBW-DFT, PBW-DFT, AR171, and RFIAA respectively. RFIAA thus gives a 2.6 times better resolution than PBW-DFT that uses the same spectral bandwidth. Figure 3.3(f) shows the resolution as a function of SNR, based on simulated OCT data of a wedge. The resolution for DFT reconstruction is independent of SNR and thus follows a horizontal line. For spectral estimation methods, the resolution improves with increasing SNR [21], which is visible in the decreasing curves for AR171 and RFIAA. For an SNR above 30 dB, AR171 outperforms RFIAA and achieves resolutions up to 0.2 μm for SNR > 75 dB where RFIAA obtains a resolution of 1 μm. However, in practice, few OCT measurements are performed at such a high SNR. For SNR values below 30 dB, RFIAA outperforms AR171, showing that it is better able to handle data with a medium to low SNR. Over the full studied SNR range, RFIAA gave a better resolution than PBW-DFT. The resolutions from the experimen-

tal data are indicated in the graph with a star and correspond well to the simulated results.

3.4.2. OCT intensity reconstruction

A major drawback of AR171 is that reconstructed intensity does not correspond with the true intensity of the reflected light. In this section, we further investigate this behavior and compare it to the performance of RFIAA. Figure 3.4(a) shows the image of an OCT simulation of 8 interfaces whose intensities drop with 6 dB with every subsequent interface. The decreasing intensity is clearly visible in the DFT reconstructed regions of the image. Figure 3.4(b) shows part of an A-line at the dashed lines in (a) for the different methods. For FBW-DFT, PBW-DFT, and RFIAA, the peaks 1 to 6 have monotone decreasing intensities corresponding to the simulated reflection intensities. In contrast, the peaks of AR171 do not follow this pattern and give fluctuating intensities that do not correspond to the real reflection intensity; e.g., peak 6 has a 10 dB higher intensity than peak 1, while it should be 30 dB lower than peak 1.

This effect is also clear when we take all the 1024 lateral positions into account, as shown in figure 3.4(c). Here, the mean intensity of each interface is indicated with a diamond, together with error bars that mark the edges of the middle 95% intensity values, i.e., the 2.5^{th} and 97.5^{th} percentile. These edges correspond to

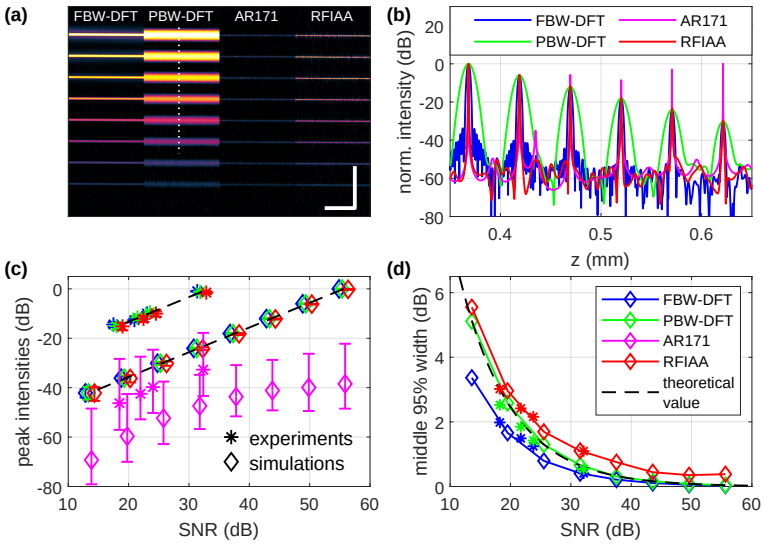

Figure 3.4: Results on OCT reflection intensity preservation. (a) OCT reconstruction of a simulated object with interfaces whose reflection intensity drops with 6 dB with every subsequent interface. The different columns indicate the results of the four methods. The scale bar is 100 µm. (b) Part of an A-scan at the dashed lines in (a), normalized to the maximum value of the A-scan. (c) The mean OCT peak intensity of the interfaces. Error bars mark the range of the middle 95% intensity values. The SNR is determined from the PBW-DFT image. (d) Full range of the middle 95% intensity values as a function of SNR of the PBW-DFT image.

2σ below and above the mean for normally distributed values. On the horizontal axis is the average SNR of the corresponding interface in the PBW-DFT image. The mean intensities for FBW-DFT, PBW-DFT, and RFIAA lie on a straight line with a slope of 1 and have small error bars. AR171 gives much lower mean intensities, due to a few high-intensity peaks on which the image is normalized. Moreover, the mean intensities do not follow a straight line, but flatten out for high SNR above 30 dB, showing that even the average intensity over 1024 lines does not follow the true reflection intensity. Most importantly, the intensity varies with 20 dB to 30 dB, clearly showing that AR reconstruction does not allow for quantifying relative reflection intensities of features within a sample.

The width of the middle 95% intensities range (95% width) as function of SNR is plotted in Figure 3.4 (d). PBW-DFT corresponds well with the theoretical value, which is based on the standard deviation of peak intensity and noise [41], and is indicated with the black dashed line. This shows that all the fluctuations are caused by the noise and not by reconstruction inaccuracies. FBW-DFT is below this theoretical value because with a larger bandwidth it has more power and thus a higher SNR than PBW-DFT, whose SNR is on the horizontal axis. The 95% width with RFIAA is less than 0.5 dB above the theoretical value, a difference that is negligible compared to typical dynamic ranges in OCT images. It is worth noticing that for high SNR, where the theoretical values and DFT-based methods go to 0, RFIAA remains at a plateau of about 0.5 dB. This may indicate that where DFT-based methods reduce the variation in peak intensity, RFIAA uses this extra SNR to increase the resolution while keeping the variation in peak intensity at an acceptable level. For the DFT and RFIAA methods, the 95% width remains below 3 dB for SNRs above 20 dB. This is in sharp contrast with AR171, that has 95% widths between 20 dB and 30 dB, which are outside the vertical range of Figure 3.4(d).

The simulation results on intensity reconstruction were complemented by measurements on the layered interface phantom. The four interfaces had SNRs ranging from 18 dB to 32 dB. The mean intensities and 95% widths are indicated with stars in Figure 3.4(c-d) and correspond well with the simulations.

In conclusion, RFIAA, in contrast to to AR171, reconstructs true reflection intensity and thus allows for quantitative analysis based on intensity (e.g. measuring optical attenuation).

3.4.3. Medium sparse sample

As a biological object, we used a slice of onion tissue, which has large cells without internal scattering structure, except for the nucleus, thus having a medium sparsity level. The cell walls are made up of two layers that are typically 5-11 µm (6.5-15 µm optical path length (OPL)) apart, and could thus only be resolved with a high axial resolution.

Figure 3.5(a-d) shows the OCT images of the slice of onion, clearly revealing the cellular structure. In the FBW-DFT, the two cell wall layers are clearly distinguishable (indicated by the white arrows), though side-lobes around high-intensity reflections (indicated by the green arrow) slightly reduce the image quality. The limited resolution of the PBW-DFT reconstruction causes the double layers to merge

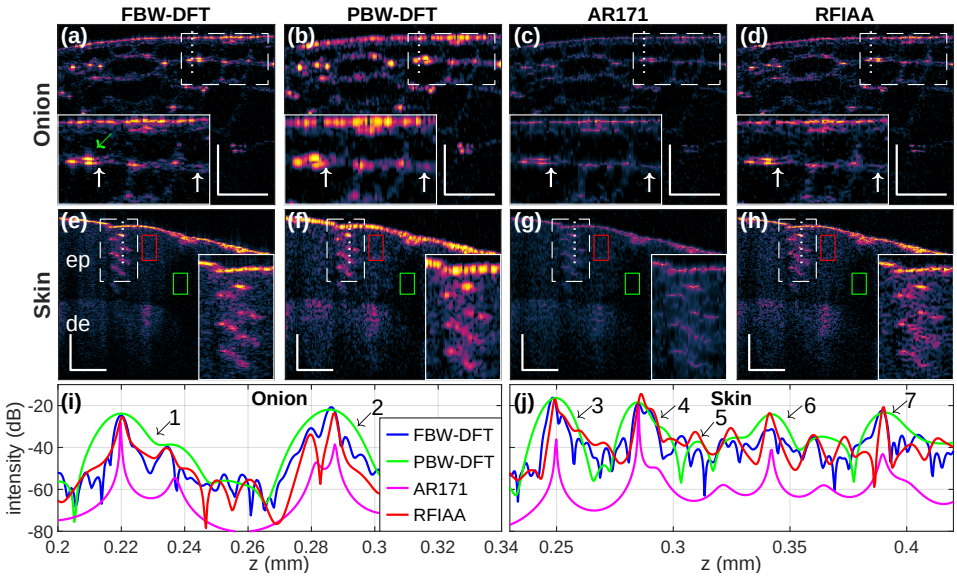

Figure 3.5: OCT imaging results of the onion and skin sample. (a-d) Are images of the onion, (e-h) are skin images and (i) and (j) are A-scans from respectively the onion and skin image at the dotted lines. The images are visualized in dB scale with the dynamic range lower limit determined from noise statistics. Scale bars indicate 150 µm.

into a thick cell wall. Even at the top surface where the separation between the interfaces is larger, they are barely resolved. AR171 and RFIAA obtain a much higher axial resolution with the same bandwidth as PBW-DFT. AR171 gives the most narrow lines, but the earlier described intensity fluctuations sometimes obscure one of the layers (e.g. at the location indicated by the right white arrow). At this position, RFIAA gives a clear image that is similar in resolution to FBW-DFT. RFIAA is designed to improve resolution while suppressing side-lobes, which is visible in the low side lobes around the high-intensity reflections (compared to FBW-DFT).

The A-scan in Figure 3.5(i) gives further insight into the performance of the studied methods. At interface 1, only PBW-DFT does not clearly resolve the two layers. AR171 gives the most narrow peaks, but the second peak has a much lower intensity and is thus barely visible in the image. Although RFIAA gives wider peaks, they are at the correct FBW-DFT intensity and the two layers are clearly resolved. In between the peaks, AR171 gives a smooth valley which is typical for AR spectral estimation. However, as these valleys are not smooth in the lateral direction, vertical stripes are visible as side-lobes in the image, which is enhanced by the necessarily large dynamic range. At interface 2, RFIAA performs well with a deeper valley and less side-lobes than FBW-DFT. AR171 again gives a much lower peak intensity and with a shallow valley, the image does not show clearly distinguished peaks. The distances (in OPL) between the peaks for FBW-DFT, AR171, and RFIAA respectively are estimated at 14.4 µm, 17.1 µm and 14.0 µm for interface 1, and 6.4 µm, 6.0 µm and 7.3 µm for interface 2. This corresponds well with each other and only AR171

on the first interface is more than 1 µm different from FBW-DFT. Concluding, RFIAA improves the resolution significantly over PBW-DFT and gives an image close to FBW-DFT with slightly less side lobes. In contrast to AR171, RFIAA reconstructs reflection intensity in better agreement with FBW-DFT which leads to enhanced image quality.

3.4.4. Non-sparse skin sample

The second biological object was a skin sample from a fingertip that has a low level of sparsity. Figures 3.5(e-h) show the OCT images of the skin sample, with the epidermal (ep) and dermal (de) layer, and the helical-shaped sweat duct (inset) clearly visible. AR171 and RFIAA have a higher axial resolution than PBW-DFT, visible in the top surface and axial thickness of the sweat duct. The top left corner of the inset shows a small crack in the top surface that is better resolved with AR171 and RFIAA. Using the red box as signal area and the green box as noise area, the CNRs are 0.76, 0.80, 0.47 and 0.64, for FBW-DFT, PBW-DFT, AR171, and RFIAA, respectively. RFIAA reconstruction gives a higher CNR than AR171, which is also visible from the appearance of the images. Moreover, where RFIAA gives well-developed speckle, AR171 gives some spurious peaks that form narrow curly structures that may be mistaken for sample features.

The A-scan at the white dotted line, Fig. 3.5(j), shows the peaks corresponding to the skin surface (number 3) and the sweat duct interfaces (indicated by numbers 4,6,7). PBW-DFT gives the broadest peaks, which RFIAA manages to narrow down to a level similar to FBW-DFT (numbers 3 and 4) or even smaller (numbers 6 and 7). AR171 gives the narrowest peaks. However, peak 7 has a significantly lower intensity than the true reflected light intensity, causing it to be less narrow and less distinct from the side lobes. RFIAA has a few high-level side lobes or speckles (number 5) that are still 7 dB below the lowest peak (6).

3.4.5. SE-OCT CNR and noise statistics

Figure 3.6 shows experimental and simulation results of homogeneous speckle regions. Figure 3.6(a) shows the images of the Intralipid suspension, which gives a homogeneous speckle pattern. As speckle size is closely linked with the spatial resolution, RFIAA gives a finer speckle pattern than PBW-DFT. The RFIAA speckle size is slightly coarser than for FBW-DFT, probably because the SNR of a single speckle that consists of a combination of multiple, unaligned, sub-resolution reflectors is relatively low. With AR171, the speckle region appears dark due to some high-intensity peaks that bring the dynamic range down. These peaks in the speckle region also cause a high variance, resulting in a CNR that is 70% below that of PBW-DFT. RFIAA gives a much better contrast with a CNR that is only 15% below that of PBW-DFT. Figure 3.6(b) shows the speckle amplitude distribution, which follows the predicted Rayleigh distribution for the DFT reconstructed images [42]. The histogram for RFIAA is very close to a Rayleigh distribution, while for AR171 it deviates significantly from this theoretical distribution. Each method gives similar histograms for the amplitude distribution in the noise region.

Figure 3.6(c) shows the simulated images of three speckle regions with decreasing

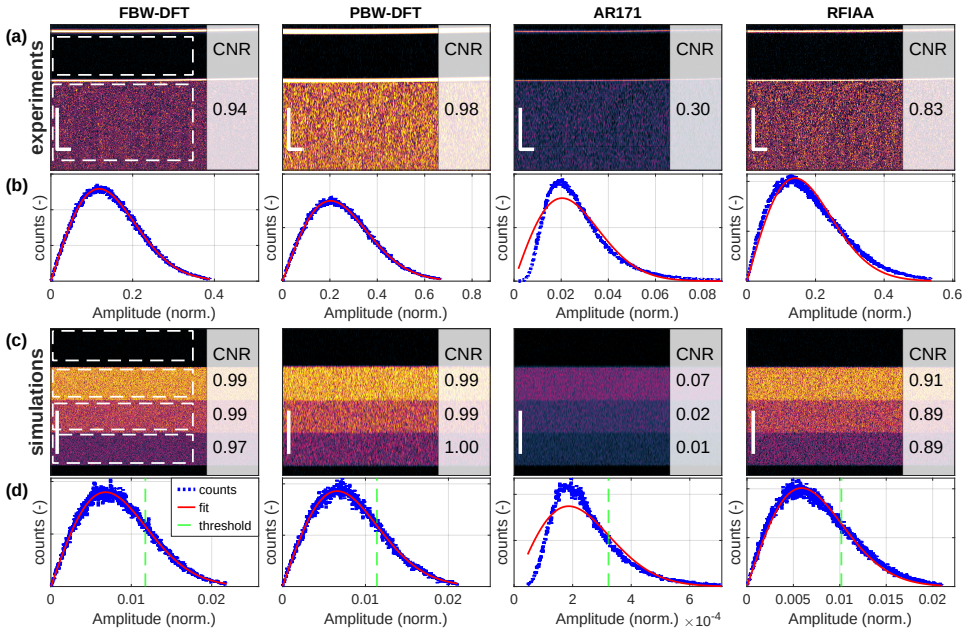

Figure 3.6: Experimental and simulation results on contrast and speckle statistics. (a) Images of an Intralipid suspension with their CNR. (b) Histogram of the OCT amplitudes in the speckle region with a fit of the Rayleigh distribution (red line). (c) Simulation images of 3 regions with different speckle intensities and their CNR. (d) Histograms of the OCT amplitude in the noise region with a fit of the Rayleigh distribution (red line). The green dashed lines indicate the lower dynamic range limit for the images of (c). Scale bars indicate 200 µm, where the lateral size of the images in (c) is undefined. The white dashed rectangles indicate the noise and speckle regions for CNR calculation.

intensities. FBW-DFT, PBW-DFT, and RFIAA give similar image contrast between the regions, with the size of the speckles being the main difference. The speckle size is similar to that in Fig. 3.6(a). The CNR of AR171 is 93% to 99% below the CNR of the DFT methods, while the CNR with RFIAA is only 10% below that of the DFT methods. The simulation results on speckle regions of different intensities correspond to the observations from the experimental data. Figure 3.6(d) shows the histograms of the OCT amplitude in the noise region (top rectangle in Fig. 3.6(c, FBW-DFT)), which have similar shapes as those for the speckle region in Fig. 3.6(b). These results indicate that RFIAA outperforms AR171 in preserving noise and speckle statistics, which is useful for, for example, tissue characterization [43] and automatic thresholding [39]. Moreover, they show that as a non-parametric method, RFIAA describes the underlying physics better than AR spectral estimation that assumes an AR model with a fixed order.

3.4.6. SE-OCT computation time benchmarking

Table 3.1 shows the computation time for the onion slice sample, averaged over 100 realizations, along with a theoretical count of the complex-valued operations

required for processing of a single A-scan by each tested method.

FBW-DFT and PBW-DFT have the same computation time as both are zero-padded to the same length. As expected, DFT reconstruction is the fastest, with a computation time of one to two orders of magnitudes below the other methods. RFIAA with parallel processing on half the useful range ($R = 4$, $N = 128$, $M = 2048$) gives a fast 0.37 s computation time for a 1024-line B-scan. Although this is not yet sufficient for video-rate processing at 20 frames per second, it approaches real-time reconstruction while for post-acquisition viewing the waiting time is negligible. It also allows for fast 3D (see visualization 1 and 2) and time-lapse OCT reconstruction within short time scales without the need for supercomputers.

AR171, with 5.23 s computation time, is significantly slower than RFIAA. Reducing the reconstruction range similar to that used for RFIAA will bring the computation time down to 0.43 s for AR43 (AR with an order of 43), but the resulting lower order may hamper the ability to reconstruct complex sample structures [21]. We note that the AR modified covariance estimator could have been implemented using a fast $\mathcal{O}(p^2)$ algorithm [44] instead of the current implementation. However this is neither available in the MATLAB programming environment, nor is it supported as

Table 3.1: Average computation time of a 1024-line B-scan for the studied methods over 100 realizations. The reduced reconstruction range and parallel processing over 4 CPU cores are optional as indicated. AR43 acts on the same reduced range data as RFIAA with reduced range. For the times in this table, $N = 512$, $M = 8192$ and $R = 4$, as used for the onion and skin sample.

Method	**#Flops/A-scan**	**B-scan reconstruction time (s)** (non-parallel)	**B-scan reconstruction time (s)** (parallel)
DFT	$M \log_2 M$	0.042	n.a.
AR	$pN + \frac{p^3}{3} + 0.5M \log_2(M)$		
AR171	$p = 171$	10.4	5.23
AR43	$p = 43$	1.15	0.43
RFIAA full range	$q_i(N^2 + \gamma N \log_2 N + 1.5M \log_2 M)$	3.47	1.63
RFIAA reduced range	$\frac{q_i}{R}\left(\frac{N^2}{R} + \gamma N \log_2 \frac{N}{R} + 1.5M \log_2 \frac{M}{R}\right)$	0.74	0.37

sharing code in [21].

Parallel processing over 4 CPU cores improves the computation speed only by about a factor two for AR171 and both RFIAA implementations. Though the improvement with parallel processing is limited, probably due to overhead with handling large matrices, it still helps to bring the computation time down and allows for fast spectral estimation OCT. These results show that our efficient RFIAA implementation of SE-OCT gives fast OCT reconstruction; it is faster than standard AR spectral estimation implementation, especially for full depth range reconstruction.

3.5. Discussion

We developed RFIAA, an optimized implementation of IAA, to successfully address three problems that arise in SE-OCT:

- the dependency of the reconstruction result on subjective user-set parameters,
- the occurrence of reconstruction artifacts, and
- the large computational load of SE methods.

We have shown that RFIAA improves the resolution over DFT methods, is non-parametric, and showed consistency in both reconstructed intensity and speckle statistics. The computation load is reduced to sub-second times for B-scan reconstruction.

In this discussion, we first compare our method with other SE-OCT methods and explore limitations of our method and potential improvements.

Comparing our method quantitatively with other SE-OCT methods is not straightforward. The obtained image quality depends on variables like bandwidth, SNR, imaged sample, and dynamic range of visualization, which differs between publications. In addition, the computation time depends on computer hardware and software implementation. As a way forward, the algorithms should be tested on the same data set, as was done with AR in the current work. To allow for comparison of future work, our data is available in a repository [45].

Still, a cautious and more qualitative comparison with earlier published methods can be made based on the results they report. The iterative re-weighted approach, as proposed by Mousavi et al. [22] is similar to RFIAA, with the main difference that it uses a different weighting matrix, which depends on user-optimized parameters. Moreover, it needs up to 50 iterations, does not adopt a recursive scheme, and uses brute force matrix inversion, leading to A-scan processing times between 1.7 and 18.2 s (29 min to 5 hours for a 1024-line B-scan). Ling et al. [23] used a $\ell 1$-norm minimization, to promote sparsity of the solution, together with a non-weighted minimum least square solver. This method needs a user-chosen Lagrange multiplier and has a large computation load with processing times of 4 s per A-scan (1 h for a 1024-line B-scan) on a high-performance computer. The resolution improvement is similar to what was obtained with RFIAA, though comparison is again not straightforward because they do not mention SNR levels for the wedge experiment

and use a different resolution criterion. Both methods allow for faster implementation, but that would need significant extra work and alteration of the algorithm. In conclusion, RFIAA obtains similar results to two recently published state-of-the-art methods without the need for parameter optimization and with orders of magnitude less computation time.

Further improvement in computation time is possible using improved computation hardware with a higher level of parallelization. Data-parallel testing of the proposed RFIAA approach on a 10-core workstation (Intel core i9-9900X) provided significant speedup, giving a fast 0.0607 s computation time for a 1024-line B-scan, in the case where RFIAA with parallel processing on half the useful range ($R = 4$, $N = 128$, $M = 2048$) is considered. These timing results indicate that the proposed RFIAA approach is suitable for parallel implementation on multi-core CPUs, even when fast prototyping, using high-level programming is considered. In terms of a possible future direction, the above results are indicators that a lower-level programming implementation (e.g. C/C++), along with parallel processing pragmas (e.g. OpenMP, OpenACC) deployed on multi-core CPUs and/or accelerators (GPUs) may be the way towards a real-time operating end application.

In this context, it should be highlighted that the most time-consuming part of the proposed RFIAA approach is the linear system solver, which, due to the Toeplitz structure of the underlying linear system, is tackled here using the $\mathcal{O}\left(p^2\right)$ Levinson's algorithm available in MATLAB. However, several other alternative algorithms can be used instead, offering either further computational reduction or being suitable for parallel implementation. Among them, are the so-called superfast $\mathcal{O}\left(p\log_2(p)^2\right)$ methods [46–49], the $\mathcal{O}\left(p\log_2(p)\right)$ techniques based on iterative linear solvers such as the conjugate gradient method [50, 51], and finally the fully parallelizable Schur-type algorithms, amenable for implementation on massively parallel hardware,[44, 47]

SE-OCT works especially well for samples that have a high level of sparsity and clear interfaces with a high SNR. RFIAA is however more robust to high noise levels than AR spectral estimation, as it gives a better resolution for SNR < 25 dB. It also obtains a reliable reconstruction with good contrast of non-sparse regions in a sample, though image quality improvement with respect to DFT based on the same bandwidth is disputable in these areas. However, for a partially sparse sample, RFIAA is able to sharpen the high-SNR features while retaining a good contrast reconstruction of non-sparse areas. As the resolution is SNR dependent, the SNR could be enhanced by spectral averaging, enabling higher resolution at the cost of longer acquisition times.

In this work, we assumed equal variance for all the spectral noise components. This is implemented in Eq. 3.12, where $\sigma^2(n)$ is averaged and multiplied with the identity matrix to obtain a diagonal with constant values. However, IAA also can use a wavenumber-dependent noise variance $\sigma^2(n)$. The implementation of this would allow for accurately incorporating the higher noise at lower intensity edges of the spectrum while reducing the influence of the higher noise level for these parts. However, implementation of this makes the data-covariance matrix $\mathbf{R}$ non-Toeplitz. Consequently, the fast implementation of IAA needs to be adapted leading

to an increase in computational load. Thus wavenumber dependent noise variance is most valuable when computation speed is less important than precision.

Contrary to AR spectral estimation, RFIAA obtains both the amplitude and phase of the signal. This would allow for the RFIAA also in the domains of Doppler OCT imaging and sub-resolution phase-resolved OCT motion imaging [52].

3.6. Conclusions

This paper presented RFIAA, a fast implementation of the non-parametric iterative adaptive approach, for the reconstruction of OCT images with significantly better axial resolution than conventional DFT reconstruction. This SE-OCT method successfully addresses three problems of previously developed SE-OCT, namely the dependency of the reconstruction result on subjective user-set parameters, the occurrence of reconstruction artifacts, and the large computational load. Contrary to AR spectral estimation, the non-parametric RFIAA is consistent in reconstructed intensity, yields a high contrast, and shows less spurious peaks. With a reconstruction time of 0.37 s for a 1024-line B-scan, RFIAA is significantly faster than other SE-OCT presented in literature. This brings SE-OCT a significant step closer to application.

Data availability

Data and code underlying the results presented in this chapter are available in Ref. [45].

3.7. Appendix A. Brute force IAA implementation

Below is an overview of classical, brute force IAA. The initialization of $a(m)$ and σ^2 are identical to applying weighting matrix $\mathbf{R} = \mathbf{I}_n$, being the $N \times N$ identity matrix. The brute force implementation yields identical results as with the fast algorithm.

Initialization

$$
\begin{aligned}
a(m) &= \frac{1}{N}\mathbf{f}_m^H\mathbf{y}, \quad m = 0, 1, \ldots, M-1 \\
\sigma^2(n) &= |y(n)|^2, \quad n = 0, 1, \ldots, N \\
\sigma^2 &= \frac{1}{N}\sum_{n=1}^{N}\sigma^2(n) \\
\Sigma &= \sigma^2\mathbf{I_n}
\end{aligned}
$$

Iterate Until Convergence

$$
\begin{aligned}
\mathbf{R} &= \sum_{m=0}^{M-1} |a(m)|^2 \mathbf{f}_m \mathbf{f}_m^H + \Sigma \\
a(m) &= \frac{\mathbf{f}_m^H \mathbf{R}^{-1} \mathbf{y}}{\mathbf{f}_m^H \mathbf{R}^{-1} \mathbf{f}_m}, \quad m = 0, 1, \ldots, M-1 \\
\sigma^2(n) &= \left| \frac{\mathbf{e}_n^T \mathbf{R}^{-1} \mathbf{y}}{\mathbf{e}_n^T \mathbf{R}^{-1} \mathbf{e}_n} \right|^2, \quad n = 1, \ldots, N \\
\sigma^2 &= \frac{1}{N} \sum_{n=1}^{N} \sigma^2(n) \\
\Sigma &= \sigma^2 \mathbf{I}
\end{aligned}
$$

References

[1] D. Huang, E. A. Swanson, C. P. Lin, J. S. Schuman, W. G. Stinson, W. Chang, M. R. Hee, T. Flotte, K. Gregory, C. A. Puliafito, *et al.*, *Optical coherence tomography,* Science **254**, 1178 (1991).

[2] J. Fujimoto and E. Swanson, *The development, commercialization, and impact of optical coherence tomography,* Investigative Opthalmology & Visual Science **57**, OCT1 (2016).

[3] X. Shao, X. Chen, X. Yu, Y. Hu, L. Liu, F. Shi, W. Shao, and J. Mo, *Non-destructive measurement of conformal coating thickness on printed circuit board with ultra-high resolution optical coherence tomography,* IEEE Access **7**, 18138 (2019).

[4] M. F. Shirazi, M. Jeon, and J. Kim, *Structural analysis of polymer composites using spectral domain optical coherence tomography,* Sensors **17**, 1155 (2017).

[5] T. Callewaert, J. Guo, G. Harteveld, A. Vandivere, E. Eisemann, J. Dik, and J. Kalkman, *Multi-scale optical coherence tomography imaging and visualization of Vermeer's Girl with a Pearl Earring,* Optics Express **28**, 26239 (2020).

[6] M. Iwanicka, M. Sylwestrzak, and P. Targowski, *Optical coherence tomography (OCT) for examination of artworks,* in *Advanced Characterization Techniques, Diagnostic Tools and Evaluation Methods in Heritage Science* (Springer, 2018) pp. 49–59.

[7] J. de Wit, S. Tonn, G. Van den Ackerveken, and J. Kalkman, *Quantification of plant morphology and leaf thickness with optical coherence tomography,* Applied Optics **59**, 10304 (2020).

[8] R. M. Werkmeister, S. Sapeta, D. Schmidl, G. Garhöfer, G. Schmidinger, V. A. Dos Santos, G. C. Aschinger, I. Baumgartner, N. Pircher, F. Schwarzhans, A. Pantalon, H. Dua, and L. Schmetterer, *Ultrahigh-resolution OCT imaging of the human cornea,* Biomedical Opt. Express **8**, 1221 (2017).

[9] K. Bizheva, B. Tan, B. MacLelan, O. Kralj, M. Hajialamdari, D. Hileeto, and L. Sorbara, *Sub-micrometer axial resolution OCT for in-vivo imaging of the cellular structure of healthy and keratoconic human corneas,* Biomedical Optics Express **8**, 800 (2017).

[10] S. H. Kassani, M. Villiger, N. Uribe-Patarroyo, C. Jun, R. Khazaeinezhad, N. Lippok, and B. E. Bouma, *Extended bandwidth wavelength swept laser source for high resolution optical frequency domain imaging,* Optics Express **25**, 8255 (2017).

[11] X. Shu, L. Beckmann, and H. F. Zhang, *Visible-light optical coherence tomography: a review,* Journal of Biomedical Optics **22**, 121707 (2017).

[12] C. R. Vogel, *Computational methods for inverse problems* (SIAM, 2002).

[13] P. C. Hansen, J. G. Nagy, and D. P. O'Leary, *Deblurring images: matrices, spectra, and filtering* (SIAM, 2006).

[14] M. Kulkarni, C. Thomas, and J. Izatt, *Image enhancement in optical coherence tomography using deconvolution,* Electronics Letters **33**, 1365 (1997).

[15] Y. Liu, Y. Liang, G. Mu, and X. Zhu, *Deconvolution methods for image deblurring in optical coherence tomography,* Journal of the Optical Society of America A **26**, 72 (2009).

[16] P. D. Woolliams, R. A. Ferguson, C. Hart, A. Grimwood, and P. H. Tomlins, *Spatially deconvolved optical coherence tomography,* Applied Optics **49**, 2014 (2010).

[17] S. Hojjatoleslami, M. Avanaki, and A. G. Podoleanu, *Image quality improvement in optical coherence tomography using Lucy–Richardson deconvolution algorithm,* Applied Optics **52**, 5663 (2013).

[18] E. Bousi and C. Pitris, *Axial resolution improvement by modulated deconvolution in Fourier domain optical coherence tomography,* Journal of Biomedical Optics **17**, 071307 (2012).

[19] Y. Takahashi, Y. Watanabe, and M. Sato, *Application of the maximum entropy method to spectral-domain optical coherence tomography for enhancing axial resolution,* Applied Optics **46**, 5228 (2007).

[20] C. S. Seelamantula and S. Mulleti, *Super-resolution reconstruction in frequency-domain optical-coherence tomography using the finite-rate-of-innovation principle,* IEEE Transactions on Signal Processessing **62**, 5020 (2014).

[21] X. Liu, S. Chen, D. Cui, X. Yu, and L. Liu, *Spectral estimation optical coherence tomography for axial super-resolution,* Optics Express **23**, 26521 (2015).

[22] M. Mousavi, L. Duan, T. Javidi, and A. K. E. Bowden, *Iterative re-weighted approach to high-resolution optical coherence tomography with narrow-band sources,* Optics Express **24**, 1781 (2016).

[23] Y. Ling, M. Wang, Y. Gan, X. Yao, L. Schmetterer, C. Zhou, and Y. Su, *Beyond Fourier transform: super-resolving optical coherence tomography,* arXiv preprint arXiv:2001.03129 (2020).

[24] J. Capon, *High-resolution frequency-wavenumber spectrum analysis,* Proceedings of the IEEE **57**, 1408 (1969).

[25] J. Li and P. Stoica, *Adaptive filtering approach to spectral estimation and SAR imaging,* in *Algorithms for Synthetic Aperture Radar Imagery II*, Vol. 2487 (International Society for Optics and Photonics, 1995) pp. 153–164.

[26] T. Yardibi, J. Li, P. Stoica, M. Xue, and A. B. Baggeroer, *Source localization and sensing: A nonparametric iterative adaptive approach based on weighted least squares,* IEEE Transactions on Aerospace and Electronic Systems **46**, 425 (2010).

[27] P. Stoica and R. L. Moses, *Spectral analysis of signals* (Pearson Prentice Hall Upper Saddle River, NJ, 2005).

[28] G.-O. Glentis and A. Jakobsson, *Efficient implementation of iterative adaptive approach spectral estimation techniques,* IEEE Transactions on Signal Processing **59**, 4154 (2011).

[29] M. Xue, L. Xu, and J. Li, *IAA spectral estimation: fast implementation using the Gohberg–Semencul factorization,* IEEE Transactions on Signal Processing **59**, 3251 (2011).

[30] G.-O. Glentis and A. Jakobsson, *Time-recursive IAA spectral estimation,* IEEE Signal Processing Letters **18**, 111 (2010).

[31] J. Kalkman, *Fourier-domain optical coherence tomography signal analysis and numerical modeling,* International Journal of Optics **2017** (2017).

[32] W. Roberts, P. Stoica, J. Li, T. Yardibi, and F. A. Sadjadi, *Iterative adaptive approaches to MIMO radar imaging,* IEEE Journal of Selected Topics in Signal Processing **4**, 5 (2010).

[33] P. Stoica, D. Zachariah, and J. Li, *Weighted SPICE: A unifying approach for hyperparameter-free sparse estimation,* Digital Signal Processing **33**, 1 (2014).

[34] G.-O. Glentis, *A fast algorithm for APES and Capon spectral estimation,* IEEE Transactions on Signal Processing **56**, 4207 (2008).

[35] D. J. Faber, F. J. Van Der Meer, M. C. Aalders, and T. G. van Leeuwen, *Quantitative measurement of attenuation coefficients of weakly scattering media using optical coherence tomography,* Optics Express **12**, 4353 (2004).

[36] M. Wojtkowski, V. J. Srinivasan, T. H. Ko, J. G. Fujimoto, A. Kowalczyk, and J. S. Duker, *Ultrahigh-resolution, high-speed, Fourier domain optical coherence tomography and methods for dispersion compensation,* Optics Express **12**, 2404 (2004).

[37] R. Tripathi, N. Nassif, J. S. Nelson, B. H. Park, and J. F. de Boer, *Spectral shaping for non-Gaussian source spectra in optical coherence tomography,* Optics Letters **27**, 406 (2002).

[38] S. Jiao and M. Ruggeri, *Polarization effect on the depth resolution of optical coherence tomography,* Journal of Biomedical Optics **13**, 060503 (2008).

[39] P. Steiner, J. H. Kowal, B. Považay, C. Meier, and R. Sznitman, *Automatic estimation of noise parameters in Fourier-domain optical coherence tomography cross sectional images using statistical information,* Applied Optics **54**, 3650 (2015).

[40] Y. Ling, M. Wang, X. Yao, Y. Gan, L. Schmetterer, C. Zhou, and Y. Su, *Effect of spectral leakage on the image formation of Fourier-domain optical coherence tomography,* Optics Letters **45**, 6394 (2020).

[41] B. Baumann, C. W. Merkle, R. A. Leitgeb, M. Augustin, A. Wartak, M. Pircher, and C. K. Hitzenberger, *Signal averaging improves signal-to-noise in OCT images: But which approach works best, and when?* Biomedical Optics Express **10**, 5755 (2019).

[42] J. M. Schmitt, S. Xiang, and K. M. Yung, *Speckle in optical coherence tomography,* Journal of Biomedical Optics **4**, 95 (1999).

[43] A. A. Lindenmaier, L. Conroy, G. Farhat, R. S. DaCosta, C. Flueraru, and I. A. Vitkin, *Texture analysis of optical coherence tomography speckle for characterizing biological tissues in vivo,* Optics Letters **38**, 1280 (2013).

[44] S. Theodoridis and N. Kalouptsidis, *Spectral Analysis, in Adaptive system identification and signal processing algorithms, N. Kalouptsidis and S. Theodoridis (Eds.)* (Prentice-Hall, Inc., 1993).

[45] J. de Wit, K. Angelopoulos, J. Kalkman, and G.-O. Glentis, *Fast and accurate spectral-estimation axial super-resolution optical coherence tomography,* https://doi.org/10.5281/zenodo.5482794 (2021).

[46] I. Gohberg, I. Koltracht, A. Averbuch, and B. Shoham, *Timing analysis of a parallel algorithm for toeplitz matrices on a MIMD parallel machine,* Parallel Computing **17**, 563 (1991).

[47] T. Kailath and A. H. Sayed, *Fast reliable algorithms for matrices with structure* (Society for Industrial and Applied Mathematics, 1999).

[48] M. Van Barel, G. Heinig, and P. Kravanja, *A superfast method for solving Toeplitz linear least squares problems,* Linear algebra and its applications **366**, 441 (2003).

[49] M. O. Bernabeu, P. Alonso, and A. M. Vidal, *A multilevel parallel algorithm to solve symmetric Toeplitz linear systems,* The Journal of Supercomputing **44**, 237 (2008).

[50] M. K. Ng, *Iterative methods for Toeplitz systems* (Numerical Mathematics and Science, 2004).

[51] R. H.-F. Chan and X.-Q. Jin, *An introduction to iterative Toeplitz solvers* (Society for Industrial and Applied Mathematics, 2007).

[52] R. K. Wang and A. L. Nuttall, *Phase-sensitive optical coherence tomography imaging of the tissue motion within the organ of Corti at a subnanometer scale: a preliminary study,* Journal of Biomedical Optics **15**, 056005 (2010).

4

Computational 3D resolution enhancement for optical coherence tomography with a narrowband visible light source

Phase-preserving spectral estimation optical coherence tomography (SE-OCT) enables combining axial resolution improvement with computational depth of field (DOF) extension. We show that the combination of SE-OCT with interferometric synthetic aperture microscopy (ISAM) and computational adaptive optics (CAO) results in high 3D resolution over a large depth range for an OCT system with a narrow bandwidth visible light super-luminescent diode (SLD). SE-OCT results in up to five times axial resolution improvement from 8 µm to 1.5 µm. The combination with ISAM gives a sub-micron lateral resolution over a 400 µm axial range, which is at least 16 times the conventional depth of field. CAO can be successfully applied after SE and ISAM and removes residual aberrations, resulting in high quality images. The results show that phase-preserving SE-OCT is sufficiently accurate for coherent post-processing, enabling the use of cost-effective SLDs in the visible light range for high spatial resolution OCT.

This chapter has been published as: **Jos de Wit**, George-Othon Glentis, and Jeroen Kalkman, *Computational 3D resolution enhancement for optical coherence tomography with a narrowband visible light source*, Biomedical Optics Express 14, 3532-3554 (2023)

4.1. Introduction

The spatial resolution in optical coherence tomography (OCT) determines the size of the smallest details in the sample that can be visualized. In OCT, the axial and lateral resolution can be considered to be decoupled [1]. The axial resolution is determined by the coherence length of the light source, which scales with the center wavelength λ_c and source bandwidth $\Delta\lambda$ as $\lambda_c^2/\Delta\lambda$ [2]. The lateral resolution is proportional to the center wavelength and inversely proportional to the numerical aperture (NA) of the optics that focuses the light onto the sample. To image fine details of the sample, a high resolution is needed in both the axial and the lateral direction.

The lateral resolution can be improved by using light with a shorter wavelength or increasing the NA [2]. OCT with a high NA objective lens has also been called optical coherence microscopy [3, 4]. With lateral resolutions reaching the micrometer level, sub-cellular structures could be visualized [3]. However, the use of a large NA leads to a limited range where the light is tightly focused, the depth of field (DOF), which is inversely proportional to the square of the NA. The limited DOF is especially problematic for Fourier domain OCT (FD-OCT) where the signal from the full axial range is acquired at once. Thus, most OCT setups use a low NA to capture data that is well-focused over a large depth range. However, these low NA systems cannot reach micrometer-level lateral resolutions.

Fortunately, there are several methods to extend the depth of field. Most hardware-based methods engineer beams with a large DOF, such as Bessel beams [5], or obtain images with different focus depths and combine them after acquisition [6]. Computational DOF extension methods use the overlap between the out-of-focus fields to correct for the defocus [1]. Digital refocusing corrects each en face plane for the defocus by propagating the complex field [1, 7]. Interferometric synthetic aperture microscopy (ISAM) uses an inverse scattering model to refocus the whole volume by interpolating in the 3D spatial frequency domain [1, 8, 9]. These methods can extend the DOF to over an order of magnitude (e.g. 24 times [10]), with the DOF extension being mainly limited by the signal-to-noise ratio (SNR) and the lateral extent of the phase stability.

The lateral resolution can also be improved by reducing the wavelength, with a shorter wavelength leading to a linear reduction of the DOF. As the axial resolution scales quadratically with the center wavelength, reducing the wavelength also improves the axial resolution. Therefore, many high-resolution OCT systems use light sources in the visible (VIS) wavelength range [11, 12]. While in the infrared region, the superluminescent diode (SLD) has become the standard light source for spectral domain OCT (SD-OCT), these are not readily available in the visible range. The vast majority of the reported visible wavelength range SD-OCT setups use supercontinuum (SC) lasers [11–13] whose broad spectrum can create a very high axial resolution. However, SC lasers are expensive and the more affordable lasers suffer from high intensity noise. Moreover, the high operating power of the SC laser complicates laser safety requirements and its ultra-broad bandwidth makes the optic design of spectrometers and single mode fiber architecture more complicated.

Superluminescent diodes in the VIS spectrum are available, but the currently

available SLDs have a relatively narrow bandwidth. Lichtenegger et al. used a combination of a green (510 nm) and a red (635 nm) SLD together with deep learning and supercontinuum-generated training images on the same system to obtain high-resolution OCT images [14]. However, this still needs a spectrometer to cover the full spectral range, as well as an SC laser to create training data on relevant samples. Khan et al. used an SLD in the blue range (450 nm) for optical coherence microscopy (OCM), but their axial resolution of 12 µm is an order of magnitude above the lateral resolution, strongly limiting the sectioning capability [15]. Thus obtaining both a high axial and lateral resolution is hard with the available VIS SLDs.

Computational improvement of the axial resolution, using deconvolution [16] or spectral estimation methods [17], can be an alternative to using sources with a large bandwidth. Spectral estimation methods can computationally improve the axial resolution in OCT beyond the bandwidth limitation [17, 18]. Recently, we presented a fast version of the iterative adaptive approach (IAA) using a recursive scheme and a fast algorithm [18]. Contrary to, for example, the auto-regressive (AR) method [17], IAA is parameter free and is able to estimate both the amplitude and the phase of the object. This makes it possible to combine SE-OCT with complex field-based computational methods, such as refocusing [7], inverse scattering algorithms [8] and computational aberration correction (CAO) [9, 19].

Here we demonstrate combined high axial and lateral resolution OCT imaging over an extended DOF with a narrow band visible SLD light source. To achieve this, we combine the previously developed IAA-based spectral estimation OCT (SE-OCT) with depth of field extension by ISAM.

First, we apply SE-OCT to improve the axial resolution. The improved axial resolution corresponds to an extrapolation of the interference spectra in the k-direction. Instead of using the DFT of the z-domain IAA data, the extrapolation in k-domain is implemented by using the missing-data IAA (MIAA) [20]. Rather than providing an image in the z-domain, MIAA gives the extrapolated data in k-domain corresponding to the high axial resolution image. Second, we apply ISAM to extend the DOF. ISAM is a resampling of the OCT spectra in the spatial frequency domain. Third, we apply CAO to correct any remaining aberrations. To test the algorithms and to get insight into the origin of the obtained improvements we have simulated the entire SE-ISAM processing pipeline. The simulations are compared to the experimental data. With MIAA we demonstrate the use of the cost-effective SLDs in the VIS range for high axial resolution OCT while, with the combination with ISAM and CAO, a high resolution is obtained in the lateral direction over a depth range that is much larger than the conventional DOF.

4.2. Theory

Figure 4.1 gives a schematic overview of the proposed method, combining spectral estimation and ISAM, applied on the spatial-domain OCT data that is obtained after conventional DFT-based processing. The axial region of interest of the complex-valued OCT image is Fourier transformed into the k direction (a) to obtain input spectra for the recursive fast IAA (RFIAA). RFIAA (blue arrow) first normalizes the interference signal and selects the high SNR part (b), after which the actual RFIAA

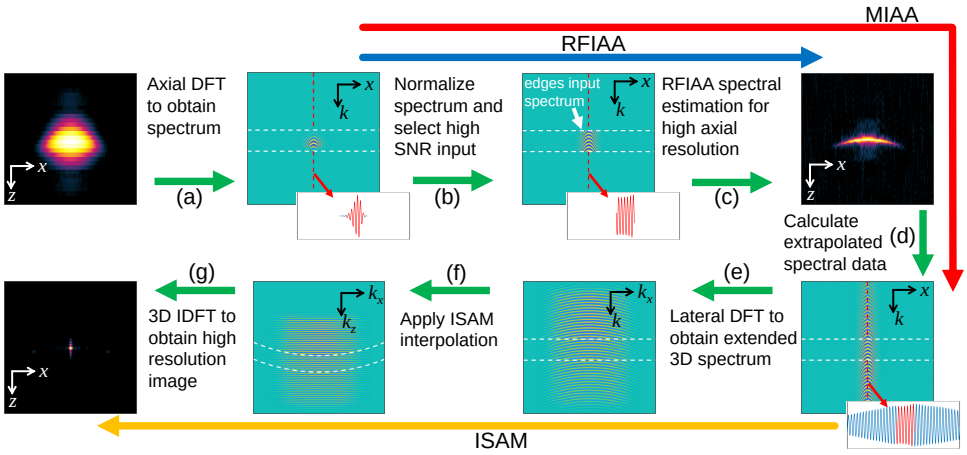

Figure 4.1: Schematic overview of the combined SE ISAM processing pipeline. In step (a), the interference spectra are obtained from the low-resolution OCT image. Steps (b-c) show the RFIAA spectral estimation to obtain the complex-valued OCT image with axial resolution improvement. Step (d) added to RFIAA completes MIAA, resulting in the extrapolated interference spectra. Steps (e-g) perform ISAM inverse scattering. The combination of SE and ISAM results in an image with a high resolution in both the axial and the lateral direction. The white dashed lines indicate the edges of the input spectrum for RFIAA spectral estimation OCT. The line plots are illustrations of the spectrum at the center (red-dashed line), with the RFIAA input spectrum in red.

algorithm is applied (c). Missing-data IAA (MIAA) (red arrow) not only estimates the spatial domain signal as RFIAA does, but extrapolates the input spectrum (d). Then, ISAM is applied (orange arrow) to refocus the image outside the depth of field, resulting in a high resolution in both the lateral and the axial direction. ISAM is implemented via a lateral spatial Fourier transform (e), interpolation in k-space (f), and a 3D DFT (g).

In Figure 4.1 we propose to first use SE and then ISAM. The opposite order could have an obvious advantage of an improved SNR with ISAM, leading to a higher axial resolution with the application of SE. However, first applying ISAM and then SE has some significant problems on which we will elaborate in section 4.5.

In the next sections, we first discuss MIAA, including a summary of the previously published RFIAA method. Then we briefly summarize the ISAM theory.

4.2.1. Spectrum extrapolation with missing-data IAA

The spectral-domain OCT signal

The one-dimensional interference signal in Fourier-domain OCT (in our case SD-OCT) can be described as [21]

$$I(k) = S_0(k) \int_{-\infty}^{\infty} \tilde{a}(z) \mathrm{e}^{-i2kz} dz, \tag{4.1}$$

where $S_0(k)$ is the source spectral density as a function of wavenumber k, $\tilde{a}(z) = a(z) + a^*(-z)$ is the combined reflectivity and conjugate reflectivity as a function

of propagation distance z in optical path length (OPL). Equation (4.1) shows that the interference signal, measured as a function of k is the product of the source spectrum and the Fourier transform (FT) of the reflectivity $\tilde{a}(z)$. The reflectivity $\tilde{a}(z)$ is usually estimated with an inverse FT resulting in an OCT reflectivity that is the convolution of the reflectivity with the inverse FT of the source spectrum, the latter of which acts as the axial PSF.

In OCT, the interference signal is measured on a discrete grid and can be approximated as [18]

$$\mathbf{y}_g \approx \sum_{l=0}^{L-1} a(z_l)\mathbf{f}_g(z_l) + \eta, \tag{4.2}$$

where $\mathbf{y}_g$ is an $N_g \times 1$ vector containing the given normalized interference signal $I(k_n)/S(k_n)$ at discrete wavenumber k_n and $a(z_l)$ is the discretized reflectivity. The vector

$$\mathbf{f}_g(z_l) \triangleq \left[\begin{array}{ccc} \mathrm{e}^{-2iz_l k_0} & \dots & \mathrm{e}^{-2iz_l k_{N_g}} \end{array} \right]^T, \tag{4.3}$$

is an $N_g \times 1$ vector with the Fourier components, and η is an $N_g \times 1$ noise vector. Note that here the subscript $\bullet_g$ will be used for measured or given spectral data.

The iterative adaptive approach

Obtaining the reflectivity $a(z_l)$ from the measured spectrum is equivalent to a spectral estimation problem [17, 18], which can be solved with a variety of methods. Recently, we showed that the non-parametric iterative adaptive approach (IAA) [22] can significantly improve the axial resolution with respect to the conventional discrete Fourier transform (DFT) reconstruction [18].

In brief, IAA estimates the reflectivity $a(z_l)$ with a weighted least squares solution of equation (4.2) as

$$a(z_l) = \mathrm{argmin}_{a(z_l)} \left| \mathbf{y}_g - a(z_l)\mathbf{f}_g(z_l) \right|^2_{\mathbf{Q}_g^{-1}(z_l)}, \quad l = 0, 1, \dots, L-1, \tag{4.4}$$

where the weighting matrix $\mathbf{Q}_g(z_l)$ is the interference covariance matrix of the data excluding the contribution for z_l. This matrix suppresses the contribution of high-intensity signals that are located at depths different from the estimated depth location z_l, thus suppressing side lobes and edges of the main lobe of strong reflectors. Solving Eq. (4.4) results in an estimated reflectivity with an improved axial resolution. In view of the expected resolution improvement, L is usually chosen to be several times the input spectrum length N_g. In practice, this means that the $a(z_l)$ is calculated on a denser sampled grid with the same axial depth range as the DFT-based reconstruction.

The solution of Eq. (4.4) can be written as

$$a(z_l) = \frac{\mathbf{f}_g(z_l)^H \mathbf{R}_g^{-1} \mathbf{y}_g}{\mathbf{f}_g^H(z_l) \mathbf{R}_g^{-1} \mathbf{f}_g(z_l)}, \quad l = 0, 1, \dots, L-1, \tag{4.5}$$

where

$$\mathbf{R}_g = \sum_{l=0}^{L-1} |a(z_l)|^2 \mathbf{f}_g(z_l)\mathbf{f}_g^H(z_l) + \Sigma \tag{4.6}$$

is the estimate of the data covariance matrix, which is estimated based on the estimated reflectivity $a(z_l)$. The variable Σ is the covariance matrix of the noise η, which is a diagonal matrix that can be estimated from the data and $\mathbf{R}_g$ [18].

The sample reflectivity $a(z_l)$ is initialized as the DFT of $\mathbf{y}_g$ with zero-padding, which is equivalent to initializing the data covariance matrix with the identity matrix, $\mathbf{R}_g = \mathbf{I}$. By iterating between equations (4.5) and (4.6), the estimate for the (complex) reflectivity $a(z_l)$ is refined. Usually, 10 iterations are sufficient for convergence [22].

4

Missing-data IAA

IAA estimates the spatial-domain reflectivity $a(z_l)$, however, for the application of ISAM, the spectral data corresponding to the high axial resolution image needs to be estimated. This is an extrapolation of the interference spectrum outside the range where it is measured, i.e. this data is missing from the measured data.

When missing data problems occur, the IAA algorithm can be used for missing data recovery following a two step procedure as described in [20]. MIAA can cope with arbitrary missing data patterns, for uniform or nonuniform sampling, interpolation as well as extrapolation of data sequences. In our case, we consider the interference spectrum at wavenumbers k where it is measured (to be more precise, the high SNR part of the measured interference spectrum) as the given data. For the application of ISAM, we aim to estimate the interference spectrum at wavenumbers outside the given spectral range (left-hand side and right-hand side data extrapolation). This data is not physically measured and will be indicated as missing data. First, IAA is applied on the given data set for the estimation of the z-domain reflectivity parameters and the computation of the relevant covariance matrices. Then, extrapolated data (missing data) are estimated using a linear minimum mean squared error (MMSE) estimator.

The MMSE MIAA data extrapolation considers the data sequence of the interference spectrum of the form

$$\mathbf{y} = \begin{bmatrix} \mathbf{y}_g \\ \mathbf{y}_m \end{bmatrix}, \quad \mathbf{y}_m \triangleq \begin{bmatrix} \mathbf{y}_{mL} \\ \mathbf{y}_{mR} \end{bmatrix} \tag{4.7}$$

where the subscript $\bullet_m$ indicates the missing data, $\bullet_{mL}$, the left hand side missing data, and $\bullet_{mR}$ the right hand side missing data. Vector $\mathbf{y}_g$ of size $N_g \times 1$ contains the given data, while vector $\mathbf{y}_m$ of size $N_m \times 1$ represents the missing data. The Fourier vector of Eq. (4.3) follows a compatible representation, i.e.,

$$\mathbf{f}(z_l) = \begin{bmatrix} \mathbf{f}_g(z_l) \\ \mathbf{f}_m(z_l) \end{bmatrix}. \tag{4.8}$$

In the first step of MIAA, the reflectivity $a(z_l)$, $l = 0, 1, \ldots, L-1$ has been estimated using IAA on the given data, iterating equations (4.5) and (4.6). At the missing data recovery step, a general linear estimator of $\mathbf{y}_m$ is considered, [20],

$$\mathbf{y}_m = \mathbf{T}\mathbf{y}_g \,. \tag{4.9}$$

The matrix $\mathbf{T}$ that gives MMSE estimation of $\mathbf{y}_m$ is given by

$$\hat{\mathbf{T}} = \mathbf{R}_{mg}\mathbf{R}_g^{-1} \,, \tag{4.10}$$

where $\mathbf{R}_{mg}$ is the $N_m \times N_g$ cross-covariance matrix between the missing or extrapolated data and the given data. $\mathbf{R}_{mg}$ can be estimated using known quantities in a similar way to the autocovariance matrix in IAA as

$$\mathbf{R}_{mg} = \sum_{l=0}^{L-1} \left|a(z_l)\right|^2 \mathbf{f}_m(z_l)\mathbf{f}_g^H(z_l) \,, \tag{4.11}$$

where $\mathbf{f}_m(z_l)$ is the $N_m \times 1$ vector with Fourier components at z_l corresponding to the missing wavenumbers k_n equivalent to Eq. (4.3). Combining eqs. (4.9) to (4.11), we obtain the estimation of the missing data

$$\mathbf{y}_m = \sum_{l=0}^{L-1} \left[\left|a(z_l)\right|^2 \mathbf{f}_g^H(z_l)\mathbf{R}_g^{-1}\mathbf{y}_g\right] \mathbf{f}_m(z_l) \,. \tag{4.12}$$

Computational implementation of MIAA

Here, we consider the application of MIAA on OCT spectral data that is uniformly sampled in the k-domain. Moreover, the reflectivity coefficients $a(z_l)$ in Eq. (4.5) are estimated on a uniformly sampled z-domain grid. As a result, the components of the Fourier vector in Eq. (4.3) are of the form

$$\mathrm{e}^{-2iz_l k_n} = \mathrm{e}^{-2\pi i \frac{l}{L} n} \,, \tag{4.13}$$

with l and n integers that go from 0 to $L-1$ and $N_g - 1$ respectively, implying a discrete space Fourier representation for the Fourier vector.

The specific structure of the given data as well as the Fourier vector, Eqs. (4.7) and (4.8) respectively, are such that the given data consists of a continuous data segment $\mathbf{y}_g$. This allows for the use of the fast IAA (FIAA) method for the estimation of the reflectivity coefficients $a(z_l)$. Thus Eqs. (4.5) and (4.6) are actually implemented in a computationally efficient way using fast Toeplitz matrix algebra and the Fast Fourier Transform (FFT) [18, 23]. The computational complexity of a single iteration of the FIAA algorithm is given by

$$\mathcal{C}_1\left(N_g, L\right) \approx N_g^2 + 12N_g \log_2 N_g + 1.5L \log_2 L \,, \tag{4.14}$$

which compares favorably against the $\mathcal{O}\left(N_g^3 + N_g^2 L\right)$ complexity required by the brute force approach.

Moreover, the missing data consist of continuous data segments $\mathbf{y}_{mL}$ and $\mathbf{y}_{mR}$ which are actually on the left-hand side and the right-hand side of the interpolated

spectral data, respectively. Thus, we implement Eq. (4.12) using fast Toeplitz matrix operations and the FFT, resulting in an additional computational cost of

$$\mathcal{C}_2\left(N_g, L\right) \approx N_g^2 + 6N_g \log_2 N_g + L \log_2 L\,. \tag{4.15}$$

Consequently, the overall computational cost of the proposed fast MIAA for the recovery of the missing OCT data is given by

$$\mathcal{C}\left(N_g, L\right) = q_{FIAA}\mathcal{C}_1\left(N_g, L\right) + \mathcal{C}_2\left(N_g, L\right)\,, \tag{4.16}$$

where q_{FIAA} is the number of FIAA iterations. Usually, 10 iterations are sufficient for convergence [18, 22, 23].

B-scan OCT imaging is performed by processing consecutive A-scans as columns in an image matrix. Although these columns can be processed independently to produce the corresponding sequence of depth profiles, a warm start initialization procedure can be applied that drastically reduces the required amount of iterations. We use the data covariance matrix of the previously processed A-scan for the initialization of the currently processed A-scan as it is expected that successive A-lines have only a slight variation to each other as they partially probe the same sample structure. We called this method the recursive fast IAA (RFIAA) [18, 24] and this approach generates results without any substantial loss in performance using only 2 iterations. When RFIAA is used in place of FIAA, the computational complexity of the proposed fast recursive MIAA for the recovery of the missing OCT data is given on the average (per A-scan) by

$$\begin{aligned}\mathcal{C}\left(N_g, L\right) &= 2\mathcal{C}_1\left(N_g, L\right) + \mathcal{C}_2\left(N_g, L\right) \\ &\approx 3N_g^2 + 18N_g \log_2 N_g + 2.5L \log_2 L\,.\end{aligned} \tag{4.17}$$

Finally, we note that the proposed fast MIAA OCT missing data recovery approach requires the use of a grid size L at least as large as the desired target (given and missing) spectrum length, i.e. $L \geq (N_g + N_m)$. The use of grid size of length $L = 2(N_g + N_m)$ proved to be adequate in our application.

4.2.2. Interferometric synthetic aperture microscopy

The 3D measured signal in point-scanning OCT can be described as the convolution of a space-variant complex PSF $h(x, y, z; k)$ with the scattering potential $f(x, y, z)$ of the sample [1] as

$$S(x, y; k) = \iiint h(x - x', y - y', z - z'; k) f(x', y', z') dx' dy' dz', \tag{4.18}$$

where x and y are the lateral coordinates of the beam location, $z = 0$ is the focus depth, and k is the measured wavenumber corrected for the refractive index of the sample.

By taking the lateral Fourier transform and using asymptotic approximations for near-focus and far-from-focus cases, Eq. (4.18) can be rewritten as [1, 25]

$$S(k_x, k_y; k) = H(k_x, k_y; k) \int f(k_x, k_y, z') \mathrm{e}^{i\sqrt{4k^2 - k_x^2 - k_y^2} z'} dz', \tag{4.19}$$

where $H(k_x, k_y; k)$ is the space-invariant optical transfer function, and the integral is the Fourier transform in the z-direction of $f(k_x, k_y, z)$ with wavenumber

$$k_z = \sqrt{4k^2 - k_x^2 - k_y^2}. \tag{4.20}$$

For Gaussian beams $H(k_x, k_y; k)$ is relatively smooth and acts as an amplitude optical transfer function. Thus, the scattering potential in k-space can be approximated as

$$f(k_x, k_y, k_z) \approx \frac{k_z}{\sqrt{k_z^2 + k_x^2 + k_y^2}} S(k_x, k_y; k)\Big|_{k=\frac{1}{2}\sqrt{k_x^2+k_y^2+k_z^2}}, \tag{4.21}$$

where the resampling from k to k_z, based on the lateral component of the measured k, corrects for the depth-dependent defocus and the pre-factor provides the scaling for the change in coordinates.

Interpreting ISAM in the k-space description, the OCT signal for a wavenumber k is obtained along the Ewald sphere in the (k_x, k_y, k_z)-space with its center in the origin and a radius of $2k$, the factor 2 accounting for the backscattering geometry [26]. Rather than assuming that $k_z = 2k$, which is done when the axial reconstruction is considered independent from the lateral spatial frequency, ISAM places the data at its true k_z coordinate as given by Eq. (4.20). After interpolation to a linear grid in k_z, see Fig. 4.1(f), the refocused image with depth-invariant resolution can be obtained by taking a 3D inverse DFT of $f(k_x, k_y, k_z)$, see Fig. 4.1(g).

4.3. Methods

4.3.1. Experimental setup

Figure 4.2 shows a schematic overview of the custom build high-resolution OCT setup. Light from the fiber-coupled green superluminescent diode (EXS210118-01, Exalos) is coupled into a 50:50 wideband fiber coupler (TW560R5A2, Thorlabs), that distributes the light to the reference and sample arm. The reference arm consists of a collimator lens (AC256-050-A, Thorlabs), a mirror, and an iris to control the reference arm light power. A fiber-based polarization controller (FPC560, Thorlabs) in the reference arm is used to align the reference arm polarization with that from the sample arm, thus optimizing the interference signal. In the sample arm, a collimator lens (AC080-020-A, Thorlabs) gives a Gaussian beam with a waist of 3.28 mm. Two galvo mirrors (RTA-AR180, Newson, Belgium) are placed around the back focal plane of a scan lens (CLS-SL, Thorlabs) that is followed by a matched tube lens (ITL200, Thorlabs) for telecentric scanning and an objective lens (10x Plan Apochromat, Mitutoyo) with an NA of 0.28 and a working distance of 34.0 mm. The 11.2 mm diameter aperture of the objective lens is almost completely filled with the beam (expanded by the scan lens and tube lens) that has a waist diameter of 9.4 mm. The ratio between the scan angle and lateral displacement of the focus was experimentally calibrated using a resolution test target (R1DS1N, Thorlabs) as a sample. The obtained values give a lateral FOV of 1.28 mm × 1.35 mm for the $\pm 5^\circ$ scan range of the galvo mirrors, which is close to the theoretical FOV of 1.22×1.22

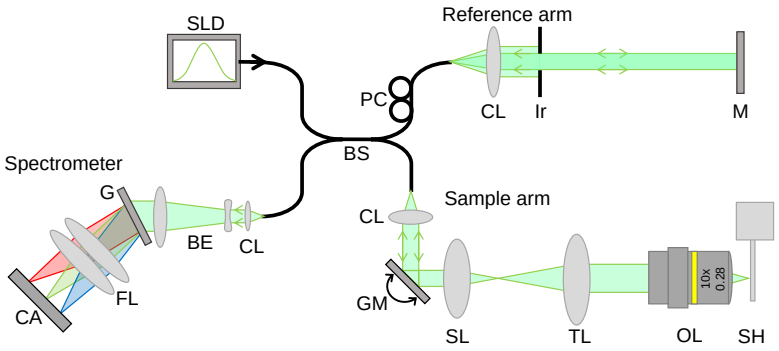

Figure 4.2: Schematic drawing of the experimental setup. SLD: superluminescent diode, BS: fiber beamsplitter, PC: polarization control, CL: collimator lens, Ir: Iris, M: mirror, GM: galvo scan mirrors, SL: scan lens, TL: tube lens, OL: objective lens, SH: sample holder, BE: beam expander, G: grating, FL: focusing lens, CA: Line-scan camera.

mm^2. The light from the reference and sample arm is recombined with the fiber coupler and guided to the spectrometer.

In the custom-build spectrometer, the light from the fiber is collimated with a collimator lens (F220APC-532, Thorlabs), expanded by a beam expander (ACN-127-A and AC508-300-A), and projected on a 50.8 mm diameter volume phase holographic grating with 1800 lines/mm (Wasatch Photonics, USA). The dispersed beam is imaged on a 6144-pixel line-scan camera (raL6144-80km, Basler, Germany) with a focusing lens consisting of two identical achromatic doublets (AC508-750-A, Thorlabs). The large beam diameter on the grating combined with the optics design based on simulations with Zemax ensured a good spectral resolution.

The chirp values for k-linearization were obtained from the difference in the unwrapped phase from two averaged A-scans with a mirror on either side of the zero-delay in the sample arm [27]. The dispersion mismatch was determined from a measurement of a single mirror with the phase fitted with an 8-order polynomial. The fitted phase deviation was used for dispersion compensation by multiplying the interference signal with a complex exponential of the phase difference [28]. To obtain sufficient SNR over the entire spectral width of the spectrometer, the k-linearization and dispersion mismatch calibration was performed using light from a fiber-coupled supercontinuum light source (NKT EUL-10, NKT photonics). The depth sampling density was determined from a linear fit on the peak locations of 32 averaged A-scans with a mirror position translated over a total range of 4.4 mm. The maximum imaging depth of 8.27 mm in air was then used to determine the linearized k-sampling density at 190 m^{-1}. A diode laser at 532 nm (CPS532, Thorlabs) was used as a reference wavelength to obtain the physical k-values for the linearized spectrum. The full spectrometer range is 48.7 nm (from 488.3 nm to 537.0 nm) with a sampling density of 7.9 pm per pixel. Using a fit on the sensitivity decay [29], the effective spectral resolution was determined to be 13.4 pm. The sensitivity decay is 6 dB at 4.1 mm ($z_{max}/2$) and 13 dB at 6.2 mm ($3z_{max}/4$). For the OCT measurements with the SLD, only 3072 of the 6144 pixels were used

between 501.3 nm and 525.6 nm as the intensity is insignificant outside this region. The measured FWHM of the light source intensity spectrum is 6.5 nm. The FWHM of the axial PSF in air was measured to be 11 µm.

The camera was triggered per B-scan on the framegrabber (PCIe-1433, National Instruments) by the galvo mirrors, the angular sweep speed being adapted to the line rate of the camera. The data acquisition was done with a custom script in Python 3.7, operated with Anaconda Spyder on a desktop computer. Also, all simulations and pre-processing of the data was done in Python 3.7.

Samples and acquisition settings

Two samples were used to evaluate the performance of the proposed method. The first test sample consisted of TiO_2 powder (Sigma Aldrich) in gelatin (Dr. Oetker, the Netherlands). A droplet of a diluted suspension of TiO_2 particles in water was added to the heated water-gelatin mixture. The mixture was poured into a custom mount, covered by a coverslip to create a flat top surface, and cooled down to room temperature. The sub-resolution particles were used to characterize the 3D resolution.

The second sample was a leaf disc that was punched out of a lettuce leaf. The leaf disc was water infiltrated by putting it in a syringe with water and lowering the pressure. When the pressure is released, the gas-exchange cavities are filled with water, reducing the refractive index contrast [30]. The leaf disc was mounted in water between two coverslips, at a sufficient distance from the coverslip to avoid saturation artifacts from the coverslip reflection.

From each sample a volume of 512×512 scan lines was obtained over a lateral area of 0.225×0.225 mm^2, giving a lateral sampling of 0.44 µm. The exposure time was set to 80 µs, at a line acquisition rate of 11.8 kHz. The large exposure time was needed because the power on the sample was measured to be only 170 µW, probably due to a limited coupling efficiency between the source and the fiber coupler/splitter.

4.3.2. OCT signal simulations

Three-dimensional OCT data was simulated by combining 1D OCT spectrum simulations [18, 21] with the intensity and phase of a Gaussian beam. The waist in the focus of the Gaussian beam was chosen based on the experimental beam width in the back-focal plane of the objective and the propagation to the relevant depth. The aperture edge is chosen where the Gaussian beam intensity is $1/e^2$, giving an effective NA of 0.235 with the 9.4 mm waist diameter. Then the waist in focus can be calculated as

$$\omega_0 = \frac{\lambda_c}{\pi \mathrm{NA}}, \tag{4.22}$$

where λ_c is the center wavelength. The OCT interference signal for a discrete set of reflectors is

$$E_s(x,y,k) = \sqrt{S_0(k)} \sum_j a_j \left(\frac{\omega_0}{\omega_{z_j}}\right)^2 \mathrm{e}^{-2\frac{(x-x_j)^2+(y-y_i)^2}{\omega_{z_j}^2}} \mathrm{e}^{i2k\zeta_j(x,y)}, \tag{4.23}$$

where x and y are the lateral coordinates of the scan beam. The scatterer j has lateral coordinates x_j, y_j and scattering amplitude a_j. The variable

$$\omega_{z_j} = \omega_0 \sqrt{1 + \left(\frac{\Delta z_j}{z_R}\right)^2} \tag{4.24}$$

is the beam waist at the scatterer depth z_j, in which $\Delta z_j = z_j - z_f$ is the distance from focus,

$$z_R = \frac{\pi \omega_0^2}{\lambda_c} \tag{4.25}$$

is the Rayleigh length of the Gaussian beam, and $S_0(k)$ is the source spectral density, which is obtained from the experimental data. The travel distance $\zeta_j(x,y)$ to the scatterer is determined from the phase of a Gaussian beam:

$$\zeta_j(x,y) = z_f + \Delta z_j + \frac{\lambda_c}{2\pi} \arctan\left(\frac{\Delta z_j}{z_R}\right) + \frac{(x-x_j)^2 + (y-y_j)^2}{2\Delta z_j \left(1 + \left(\frac{z_R}{\Delta z_j}\right)^2\right)}, \tag{4.26}$$

where the first two terms add up to the depth of the scatterer, the third term is the Gouy phase, and the last term accounts for the curvature of the Gaussian beam.

The OCT interference spectrum for each lateral position (x,y) is then calculated as

$$I(x,y,k) = \left|E_s(x,y,k) + E_r(k)\right|^2 - \left|E_r(k)\right|^2 - \left|E_s(x,y,k)\right|^2, \tag{4.27}$$

where $E_r(k) = \sqrt{S_0(k)}$ is the reference beam field. The simulated OCT image is obtained by taking the inverse DFT of $I(x,y,k)$ from k to z. Subsequently, complex Gaussian white noise is added with a standard deviation that depends on the intensity of the scatterers and the desired SNR.

4.3.3. Data processing

Conventional OCT processing and phase correction

The OCT spectral data was first processed in the conventional way by subtracting the reference spectrum, interpolating to a linear grid in k-domain, multiplying with a dispersion correction vector, and performing an inverse DFT. The reference spectra were obtained by laterally averaging the interference signal of a B-scan, excluding the spectra with saturation.

As ISAM requires lateral phase stability, the experimental data was corrected for phase drift during the measurement using a coverslip interface as a reference. The phase of the coverslip was determined by putting the image outside the signal of the coverslip at the positive depth, everywhere to 0, taking the DFT of the complex-valued OCT data in the axial direction, unwrapping the phase, and applying a linear fit to the unwrapped phase. The difference between the fit and a reference slope was corrected for by multiplying the entire spectrum with a complex exponential, such that after correction, the coverslip became a flat, horizontal plane with a constant phase.

To reduce memory requirements and computational complexity, the complex-valued image over an axial region of interest of 200 pixels (0.81 mm in water) was selected for further processing.

RFIAA and MIAA processing

The axial DFT of the phase-corrected image was used as input for the RFIAA spectral estimation algorithm. The interference signal was normalized using the reference spectrum. For the experimental data, this was obtained from the lateral average of the absolute value of the interference signal of the volume. Subsequently, RFIAA was applied on a 128-pixel-long central part of the spectrum with the highest intensity. The RFIAA reconstruction grid length L was 800 pixels, four times the original 200-pixel grid length, giving an increase in spatial sampling by a factor of 4 with respect to the original image. The number of iterations for RFIAA was set to 10 for the first line and 2 for subsequent A-lines that were initialized with the covariance matrix of the previous A-line. For MIAA, the RFIAA reconstruction grid length L was chosen eight times longer than the original grid length, such that number of samples $N_m + N_g$ is four times the length of the 200-pixel long original image. After RFIAA, the MAP estimation was applied, followed by an FFT, a circular shift, and the selection of N_m values to obtain the extrapolated spectra.

To reduce side lobes in the axial PSF, the edges of the MIAA extrapolated spectrum were tapered with a 200-pixel-long squared cosine window on both sides, bringing the intensity smoothly to 0. After the lateral Fourier transform, the high lateral frequencies, mainly containing side lobes and noise, were apodized with a circular window with a squared cosine-shaped edge with an inner radius of 110 pixels (3.1 μm^{-1}) and an outer radius of 210 pixels (5.9 μm^{-1}). While the side-lobes were significantly suppressed, the effect on the main lobe width for the experimental data was barely noticeable, while the effect on the simulation data was moderate.

RFIAA and MIAA were implemented in MATLAB (R2020a). The processing was done on a Dell Precision 5820 desktop computer with an Intel Xeon W-2223 CPU and 32 GB RAM. The processing time for the volume with 512×512 A-lines was around 113 s for RFIAA and 181 s for MIAA, 0.22 s and 0.35 s per B-scan respectively.

ISAM data processing

ISAM requires the focal plane depth and the sample refractive index as input parameters. The focal plane depth index was obtained by visually inspecting where the image appeared most sharp. The used refractive index was set to $n = 1.33$, the refractive index of water at 900 nm wavelength and room temperature [31]. The sampling period of k_z was twice that of k, such that $k_x = k_y = 0$, $k_z = 2k$ coincides with the original grid. The grid of k_z was extended such that the k-space contained all the interpolated data. After MIAA and ISAM the z grid had a length of 1029 pixels in depth, resulting in an axial sampling density of 0.79 µm per pixel.

ISAM processing was implemented in MATLAB and took around 60 s per volume of 512×512 A-lines. The processing time for the conventional DFT reconstruction with ISAM was the same, as zero-padded data was used to obtain the same axial sampling density as with MIAA.

OCT resolution analysis

The 3D resolution was quantified from the images of the simulated and measured point scatterer objects. The positions of the scatterers were automatically determined using a 2D local maximum detection algorithm [32] in the xy-plane and the xz-plane. For the local maximum detection, the image is first divided by the square root of the laterally averaged intensity, that is axially smoothed with a 40-pixel standard deviation Gaussian kernel. This reduces the intensity difference between the in-focus and out-of-focus regions and enables the use of a global threshold in the final scatterer selection. Then, the difference between two local average filters with a small (4-pixel diameter) and a large (8-pixel diameter) kernel is calculated. The local maximum position is obtained where the value of this difference is the maximum over a 12-pixel-diameter kernel region. A global threshold of 1/2000 of the maximum intensity in the image excludes noise from the detected local maxima. The 3D location of the scatterers is where the 2D local maxima of the orthogonal planes overlap.

For each 3D scatterer position a $21{\times}21{\times}21$ pixel ($16.6{\times}9.2{\times}9.2$ μm^3) subvolume is selected. If the maximum intensity inside the volume lies outside the $3 \times 3 \times 3$ center pixels, the volume is excluded as it contains another scatterer with a higher intensity that would contaminate the fit. For DFT and RFIAA without ISAM, the locations from the ISAM images were used with a $31 \times 201 \times 201$ pixels ($24 \times 88 \times 88$ μm^3) subvolume, to capture the full defocused PSF.

To quantify the resolution, a 3D Gaussian function was fitted to the intensity distribution in the selected subvolumes using the least square curve fitting function `lsqcurvefit`. The standard deviation in every direction was then used to calculate the full width at half maximum (FWHM) which serves as a resolution measure. The SNR for each scatter was determined by dividing the peak intensity of the Gaussian fit by the variance of the noise amplitude in a manually selected area of the image without signal.

Computational adaptive optics

Computational adaptive optics (CAO) was implemented using the sub-aperture correlation method [33] implemented on en face planes of the OCT data. The complex-valued OCT en face images were Fourier transformed in the lateral direction to obtain the field in the pupil plane. The field in the pupil plane was shifted such that the lateral center of mass was in the center [34], after which it was transformed back to the spatial domain. These en face images were divided into four square areas, each of which was independently corrected to also address shift-variant aberrations. The image from each area was lateral Fourier transformed to obtain the field in the pupil plane. In the pupil plane field, 45 circular sub-apertures were defined on a 7×7 grid (with the four corners excluded) within a circular aperture with a radius of 1 μm^{-1}. With sub-aperture radii equal to the lateral spacing between the sub-aperture centers, the sub-apertures were partially overlapping. After inverse Fourier transformation, the magnitude images of each sub-aperture were cross-correlated with the magnitude image of two randomly chosen sub-apertures. The obtained lateral shift between the images is proportional to the difference in the local slope of the aberration between both sub-aperture positions. The obtained slope

differences were fitted with the x and y gradient of 12 Zernike polynomials (from second to fourth order) [33]. By using two randomly chosen sub-apertures instead of the center aperture as reference, the sensitivity to speckle was reduced [34, 35]. Magnitude OCT images were used rather than intensity OCT images to increase the sensitivity to the entire object structure rather than a few high-intensity peaks.

As the speckle pattern from non-overlapping sub-apertures is independent, images with strong speckle structures can give erroneous shift estimates, even when using the more robust correlation with multiple randomly chosen apertures [35]. As the aberrations are expected to change smoothly over depth, the robustness was further increased by using a weighted moving average in the depth direction over the Zernike coefficients. A 10-pixel sigma Gaussian kernel, combined with the inverse of the least squares fit error for weighting, ensured both smoothness and a lower weight for unreliable coefficients. The CAO was completed by phase conjugation in the pupil plane using multiplication by a complex exponential to obtain a flat phase profile. The aberration-corrected en face OCT image was then obtained by inverse Fourier transformation. As ISAM removes most of the defocus, the magnitude of the aberrations was limited and it was not needed to iterate the procedure.

CAO was implemented in Python 3.7 and took around 4 s per en face image (1 s per sub-image).

4.4. Results

4.4.1. Point scatterer sample OCT imaging

Figure 4.3 shows the OCT images of the gelatin phantom filled with TiO_2 particles. The TiO_2 particles are well visible in the OCT images as they have a high intensity. The B-scans show a band of high-intensity background near the focal plane. They come from impurities in the gelatin that appear in the focal plane depth range because of the high light intensity.

The DFT method shows vertical stripes near the focus in the xz-plane, Fig. 4.3(a) due to the mismatch between the axial and the lateral resolution. The en face image in the focal plane, Fig. 4.3(b), shows many spots at a resolution around the diffraction limit. Outside the small focal region, Fig. 4.3(c), large blurred spots are visible in the xz-plane and the out-of-focus en face image.

RFIAA enhances the axial resolution, giving almost isotropic-shaped spots in the focal plane. The in-focus en face image (b) shows fewer scatterers as the optical depth sectioning due to the spectral estimation is improved. However, as RFIAA does not account for the defocus, there is still a large lateral blur outside the focal range as seen in (a) and (c).

With DFT+ISAM, the signal outside the focal region is effectively refocused, giving narrow vertical stripes (a) or points in the en face image (c). The out-of-focus lateral resolution is similar to that in focus, as expected from the correct implementation of ISAM. Due to the poor axial resolution, the en face image shows many scatterers and the B-scan image has limited quality.

Combining MIAA and ISAM both improves the axial resolution and extents the

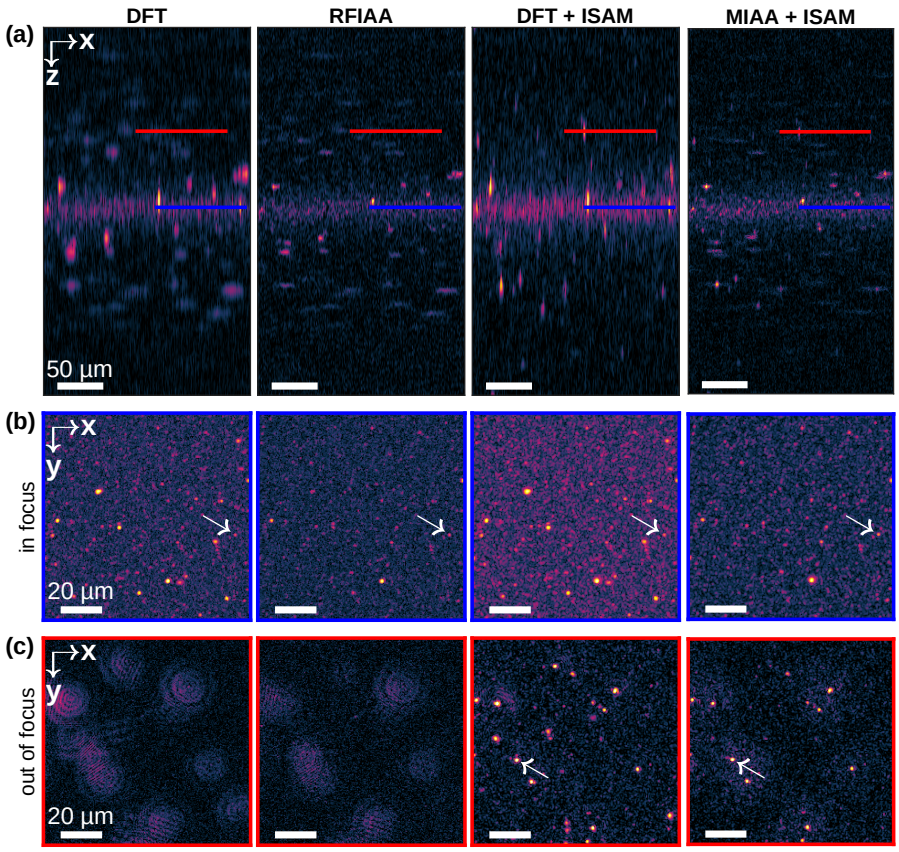

Figure 4.3: OCT images of the TiO_2 sample processed with the different methods: (a) Shows B-scans. (b) Shows sections of the en face image in focus (blue line in (a)). (c) Shows the en face image 82 µm above focus (red line in (a)). The white arrows indicate the scatterers that are shown in Figure 4.4(a-f) in more detail.

depth of field. The axial resolution and optical sectioning in focus are similar to that of RFIAA. Outside the focal depth range, ISAM refocuses the signal, which is visible in the narrow spots in the xz-plane (a) and the small dots in (c). In the en face images with MIAA+ISAM, fewer scatterers are visible than with DFT+ISAM due to the improved axial resolution. Some background signal is visible around the scatterers at the location of the original defocused spot, which we attribute to residual phase noise in the MIAA reconstruction at low SNR, giving incoherent signals that cannot be refocused with ISAM. As the intensity is much lower than that of the scatterer, the impact on the image quality is limited.

The imaging results in Figure 4.3 qualitatively show that MIAA+ISAM successfully combines the axial resolution improvement of IAA-based SE-OCT with DOF extension using ISAM. The next section analyzes these results quantitatively.

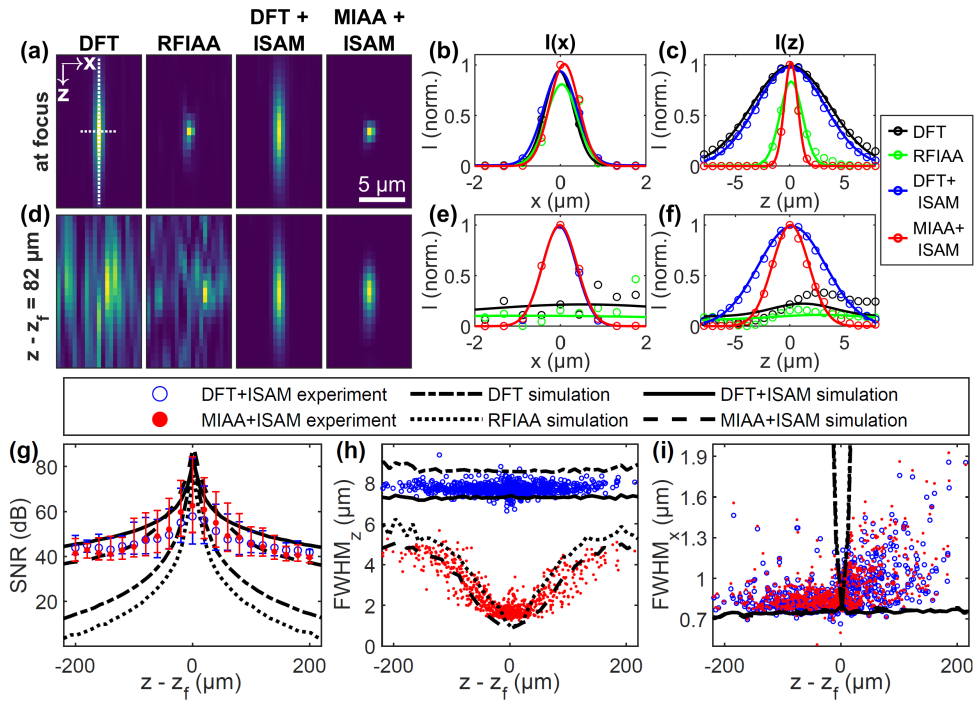

Figure 4.4: The lateral and axial OCT resolution for the various computational methods. The top and middle row show an example point scatterer at focus (white arrow in Fig. 4.3(b)) and 82 μm above focus (white arrow in Fig. 4.3(c)). (a,d) Show the xz cross sections, (b,e) the lateral and (c,f) axial line cross sections at the white dotted line. The circles indicate the OCT intensity and the solid line is the corresponding 3D Gaussian fit. (g) Shows the SNR as a function of depth from focus, the experimental data being grouped per 20 μm depth range. (h-i) Show the resolution in the axial and the lateral direction for experimental and simulated data. In (i) the lines for the simulated data without (DFT and RFIAA) and with ISAM (DFT+ISAM and MIAA+ISAM) overlap.

4.4.2. OCT resolution analysis

Figure 4.4 shows the results from the resolution analysis of the OCT images of the TiO_2 sample. Figure 4.4(a-f) shows two exemplary point scatterers reconstructed with the four different methods and fitted with a 3D Gaussian function. The in-focus scatterer (a-c) is imaged with relatively high resolution for all four methods and the line plots indicate that the PSF is well described by the Gaussian model. The axial resolution improvement with MIAA+ISAM is, with an axial resolution of 1.45 μm, a factor 5 better than without MIAA. Outside focus (d-f) DFT and RFIAA without ISAM give very blurry spots because of interference between the signals of several defocused scatterers and because the PSF width is larger than the chosen small volume. This also gives unreliable Gaussian fitting, see (e-f), thus we excluded these methods from the further data analysis. MIAA+ISAM is, with a resolution of 4.0 μm, a factor 1.8 better than without MIAA. The smaller improvement in axial resolution compared to in focus is caused by the lower SNR in the out-of-focus region.

The 809 automatically detected points that were at the same position (± 1 pixel in the axial direction) for both DFT+ISAM and MIAA+ISAM were used for the analysis. Simulations of 48 point scatterers divided over 4 vertical columns that span a 450 µm depth range were used to further interpret the experimental results. Here, also DFT and RFIAA without ISAM were included as the simulated scatterers were well-separated.

Figure 4.4(g) shows how, for all methods, the SNR peaks in focus and decreases further away from focus. For the experimental DFT/MIAA + ISAM data, the SNR in focus is on average around 60 dB with peaks to 80 dB, from where the SNR decreases to 40 dB at 150 µm from focus. The error bars indicate the lowest and highest SNR within each 20 µm depth interval. The large variation, especially in focus can be attributed to variation in the scattering amplitude of the TiO_2 particles. Both DFT and MIAA with ISAM are in good agreement with the simulations and have a high SNR outside of focus due to the ISAM refocusing. MIAA+ISAM has a slightly lower SNR at the edges. The simulations for DFT and RFIAA show that in focus, the SNR is similar, outside focus it drops strongly because the signal is smeared out over a large lateral range and not refocused with ISAM. The SNR with RFIAA is a bit lower due to a bit higher noise variance. The SNR of the DFT simulation drops to 10 dB at 200 µm from focus. The coherence of the low-intensity signals remains however sufficient for applying ISAM, which then improves the SNR outside focus with 15 to 30 dB.

Figure 4.4(h) shows the axial resolution as a function of the depth from focus. As expected, DFT+ISAM gives a depth-independent axial resolution of around 8 µm, slightly below the bandwidth-limited resolution of 8.1 µm. Simulations show a similar depth-independent axial resolution. ISAM improves the axial resolution with about 1 µm because it maps high lateral frequencies to lower axial wavenumbers k_z, giving an effective broadening of the spectrum (see Fig. 4.1(g)). This effect is especially significant for sources with a narrow bandwidth as the relative curvature in k space is large.

MIAA+ISAM gives a significant improvement in the axial resolution to around 1.4 to 2 µm in focus and increasing to 4.5 µm at 150 µm distance from the focus. The variation in axial resolution with depth can be explained by the variation of the SNR with depth. An SNR before MIAA above 50 dB gives a factor 5 improvement, an SNR of 30 dB gives a factor 3 improvement and an SNR of 10 dB reduces the improvement to a factor 1.5. The improvement in axial resolution, especially for SNR above 30 dB, brings it closer to being similar to the lateral resolution. The simulations show that for RFIAA and MIAA the in-focus axial resolution of 0.95 µm is slightly better than the experimental resolution. The poorer experimental axial resolution could be attributed to the background scattering of the gelatin, which reduces the local SNR. The 0.95 µm is close to the theoretical resolution of 0.85 µm, assuming a uniform SE bandwidth extension. Outside focus, RFIAA without ISAM gives a slightly worse axial resolution than MIAA+ISAM, because of the spectrum broadening with ISAM.

Figure 4.4(i) shows the OCT lateral resolution analysis. Both DFT and MIAA in combination with ISAM give a depth-independent resolution of around the diffrac-

tion limited value of 0.85 µm. This shows that MIAA sufficiently preserves coherent phase information for applying ISAM. The variation in resolution can be caused by a variation in scatterer size or by wavefront aberrations. These aberrations, which are also the cause of the large deviation at depths below focus, can be computationally corrected [9, 35], as we will show in section 4.4.4. As the deviation is similar for DFT and MIAA, it is not caused by MIAA. Simulations show that without ISAM, the nominal DOF is only about 25 µm. DFT and MIAA in combination with ISAM give a strong improvement in the resolution outside the focal region. Their depth-independent lateral resolution is around 0.74 µm over the full simulated depth range of 450 µm. The simulated resolution is at the lower limit of the experimental results because the simulations do not include the physical aperture of the objective lens. However, due to the lateral apodization during processing, the difference is limited.

The results on the lateral resolution clearly show the effectiveness of ISAM to extend the depth of field, also after spectral estimation. The shown extended DOF is around 400 µm (a factor 16 extension) for experimental data, and at least 450 µm (a factor 18 extension) for the simulation data. Note that the DOF with ISAM is more constrained by the SNR limiting the axial resolution than the remaining lateral blurring.

4.4.3. Plant leaf computational OCT imaging

Figure 4.5 shows the results for a more realistic object, a lettuce leaf. The comparison between DFT and MIAA, both in combination with ISAM clearly shows the improvement in axial resolution and image quality that our method achieves. While the plant cells in Fig. 4.5(a) barely can be distinguished with DFT+ISAM, they are clearly visible with MIAA+ISAM. The improved optical sectioning ability is also clear from the en face images, Fig. 4.5 (c), where MIAA+ISAM better visualizes the open leaf structure. This allows for clearer visualization of the plant cells and subcellular structures. An example of the improved visualization of open structure with MIAA+ISAM is shown in the zoom-in. The object has a better contrast between the water-filled intra-cellular space and the cell walls. The cell walls also appear narrower with MIAA+ISAM, probably because a tilted cell wall is laterally smeared out due to the poor axial resolution of DFT+ISAM.

Figure 4.5(b) shows a close-up of the OCT B-scan (a) for all four methods. The large asymmetry between axial and lateral resolution makes it hard to distinguish the cell walls in both DFT-based methods. RFIAA already makes the structure much clearer. However, the lateral blurring and intensity fluctuations caused by the interference of blurred signal significantly decrease the image quality, especially at the top half. By combining the axial resolution improvement of spectral estimation with the out-of-focus lateral resolution enhancement of ISAM, the cellular structures are also clearly imaged in the top half of the inset.

The effect of ISAM is even clearer from the en face images in Fig. 4.5(d), which are located around the bottom of the epidermal cell layer, the green dashed line in Fig. 4.5(a). Without ISAM, the image is significantly blurred and does not reveal any plant structure. ISAM refocuses that into a clear image of the plant tissue structure.

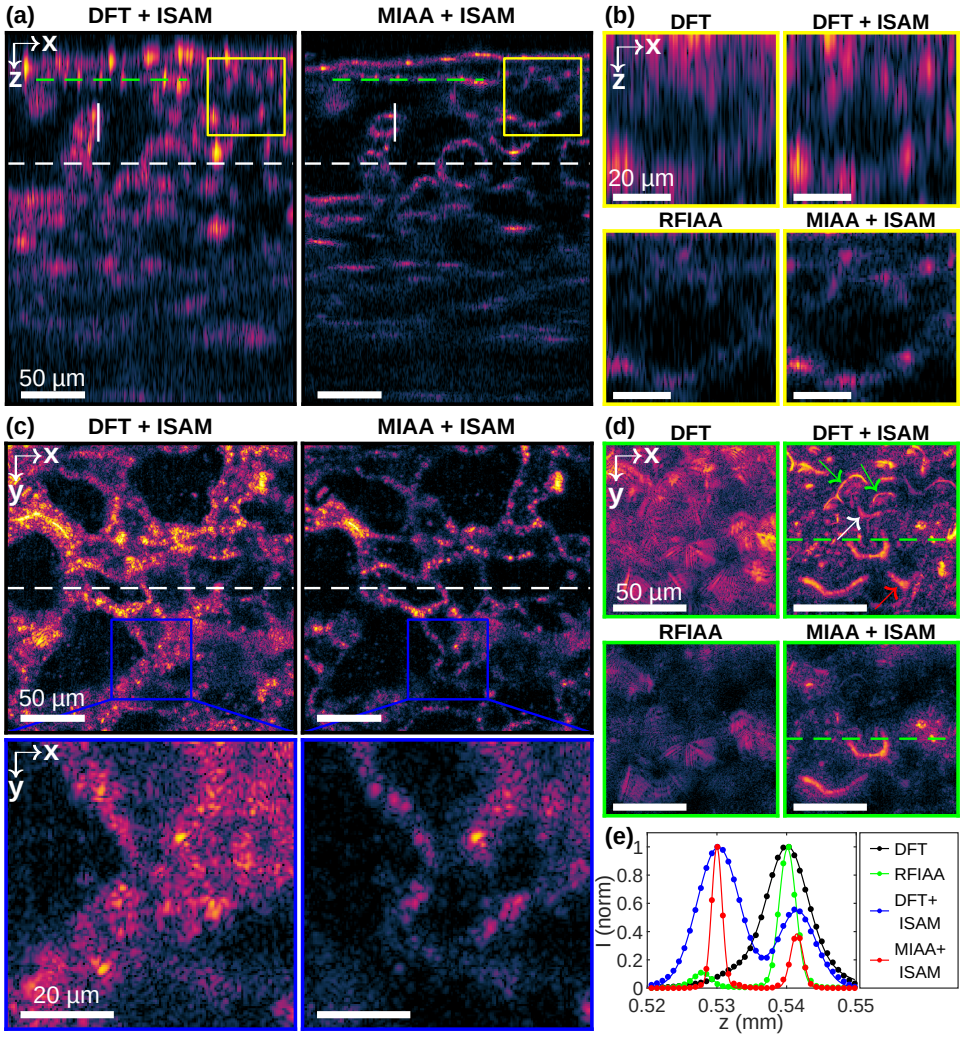

Figure 4.5: OCT imaging of the lettuce leaf. (a) An xz-cross section of the 3D leaf reconstruction, with (b) the zoom-in at the yellow square for all four methods. (c) The en face image at the white dashed line in (a), the white dashed line indicates the intersection between (a) and (c). The bottom images show the zoom-in at the blue square. (d) The en face image at the bottom of the epidermal cell layer indicated by the green dashed line in (a), for all four methods. The green dashed line indicates the intersection between the images of (a) and (d). (e) The A-scan at the vertical white line in (a) for all four methods, the points indicate OCT intensity, while the solid line is a 2-peak Gaussian fit through the intensities.

However, with DFT+ISAM the structures of different depth layers are merged. For example, the structures indicated with the green arrows have their peak intensity in a plane 6 µm higher up, the structure at the red arrow shows up in the MIAA+ISAM image 2.5 µm up and the structure indicated with the white arrow is located 4 µm

lower. MIAA+ISAM successfully sections out the signal from a narrow depth region and refocuses it with a good lateral resolution.

Figure 4.5(e) shows the A-line profiles at the vertical white line in (a). With DFT+ISAM in (a) the shape of the cell is not clear because of the poor axial resolution, while MIAA+ISAM gives a clear image. The solid lines in (e) correspond to a 2-peak Gaussian fit of the A-line segments. MIAA+ISAM gives an FWHM of the peaks of 1.8 µm and 2.1 µm respectively, compared to 7.2 µm and 6.4 µm for DFT+ISAM, a factor 3 to 4 improvement. Without ISAM, the top layer is not clearly visible, probably because of destructive interference of defocused signal. The small shift in peak location with respect to the ISAM methods could be the result of focusing the curved structure.

The lettuce leaf OCT imaging clearly shows that MIAA+ISAM does not only work for ideal point scatterers, but also for relevant biological samples with a medium level of sparsity. This proposed method gives a clear improvement in axial resolution and image quality, resulting in good-quality images with the cost-effective green SLD light source that has a bandwidth (FWHM) of only 6.5 nm.

4.4.4. Computational adaptive optics OCT

Though ISAM refocuses the signal outside the focal plane, there can be other aberrations and residual defocus. As MIAA+ISAM preserves the phase of the (complex) signal, computational adaptive optics (CAO) can be applied after MIAA+ISAM reconstruction. Figure 4.6(a-c) shows the results with CAO for the sample with the TiO_2 particles. The most significant Zernike coefficients, for defocus Z_0^2 and primary spherical aberration Z_0^4, are displayed in (a) as a function of depth. Most of the other Zernike coefficients varied around 0. Especially the defocus aberration is significant with a coefficient up to 2 radians below the focus. Note that the residual defocus is not due to wrong ISAM implementation as the aberration above focus is close to 0 for a large depth range. In absence of speckle, the error in the estimated coefficients is limited. Still, a few outliers of the estimations (blue dots) are visible, which the weighed moving average (red line) removes.

The en face plane 190 µm below focus (Fig. 4.6(b)) clearly shows the improved resolution or sharpness of the image after CAO. The improvement is quantified using 3D Gaussian fits on 983 and 1075 particles, respectively. The histogram of the lateral FWHM (Fig. 4.6(c)) shows that the aberrated spots with an FWHM above 1.2 µm are corrected, while the peak value remains at the diffraction-limited resolution. This correction improves the mean lateral FWHM with 8% to 0.87 µm, but the improvement for the aberrated spots is of course much more significant. Most improvement is obtained for depths below focus, pushing the large spot sizes that were seen in Figure 4.4(i) back to diffraction-limited values.

The lettuce leaf sample has more severe aberrations than the sample with the TiO_2 particles. The large defocus aberration, shown in (d), could potentially be reduced by optimizing ISAM settings, but that effect would never fully compensate for the defocus as the aberration is not fully linear as a function of depth. Moreover, manual optimization of the focus depth for ISAM did not give a better image over the full depth range. For the plant leaf, the variation in estimated Zernike coefficients

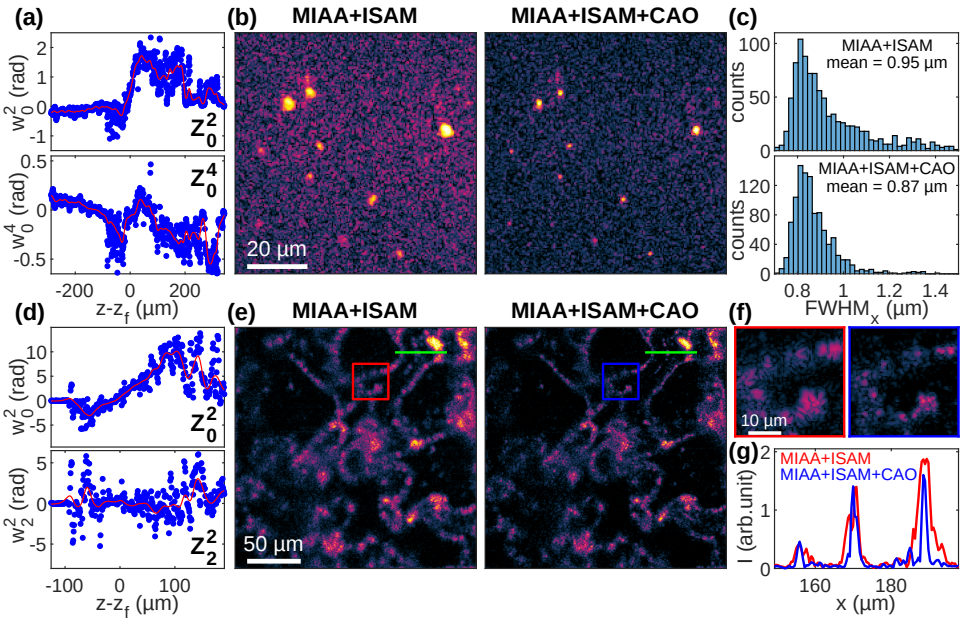

Figure 4.6: OCT imaging results for computational adaptive optics (CAO) applied after MIAA+ISAM processing. (a) and (d) show two Zernike coefficients for the top right corner of the FOV as a function of depth, the blue dots being the estimates per plane and the red line the weighed moving average. (b) Shows an en face image 190 µm below the focus of the TiO_2 particles in gelatin sample before and after CAO. (c) Shows the histogram of the lateral resolution before and after CAO. (e) Shows an en face image of the leaf at 24 µm below focus before and after CAO, (f) the inset from (e), and (g) the line-plot along the green line in (e).

from plane to plane is much larger than with the TiO_2 sample due to the presence of speckle (note the different scale in (a)). The weighed moving average (red line) reduces the variations and increases the robustness of the CAO. At depths of >100 µm below focus, the image quality was too poor for reliable aberration estimates, and even with manually optimized defocus the image quality remained poor. This may be caused by the accumulation of phase errors in the heterogeneous medium.

CAO clearly improves the sharpness and quality of the en face image (Fig. 4.6(e)). The cell walls are imaged much sharper and subtle structures are much clearer visible, as shown in the inset (f). The line plot (g) shows three peaks corresponding to cell walls, whose FWHMs improve with a factor 2 from 3.5 µm to 1.6 µm on average.

The results in Fig. 4.6 show that the data after MIAA+ISAM is of sufficient quality to apply CAO for further optimization of the resolution.

4.5. Discussion

In this work, we combined axial resolution improvement using SE-OCT with ISAM for depth of field extension.

In this discussion, we first consider our motivation for our data processing by first applying MIAA followed by ISAM. Next, we discuss some limitations of our approach and explore future opportunities.

Instead of applying spectral estimation on the original spectra (in the k-direction), applying it to the ISAM-processed data (in k_z-direction) could have an important advantage. ISAM improves the SNR of the out-of-focus signal, which would then result in a better axial resolution with SE-OCT. There are several ways in which ISAM and SE can be combined. We discuss here two combinations:

1. First applying ISAM, then applying SE from the (x, y, k_z)-domain to the (x, y, z)-domain.
2. First applying ISAM interpolation, leaving the interpolated data in the (k_x, k_y, k_z)-domain, then applying SE from (k_x, k_y, k_z)-domain to the (k_x, k_y, z)-domain, followed by a lateral inverse DFT to the (x, y, z)-domain.

The first option would be the most obvious way, but there is a significant complication with performing the image enhancement in this order. As ISAM maps the signal at higher lateral spatial frequencies k_x, k_y to lower k_z, the spectrum in k_z will be broader than the spectrum in k. The amount of broadening and the resulting shape is, however, dependent on the lateral frequency content of the object.

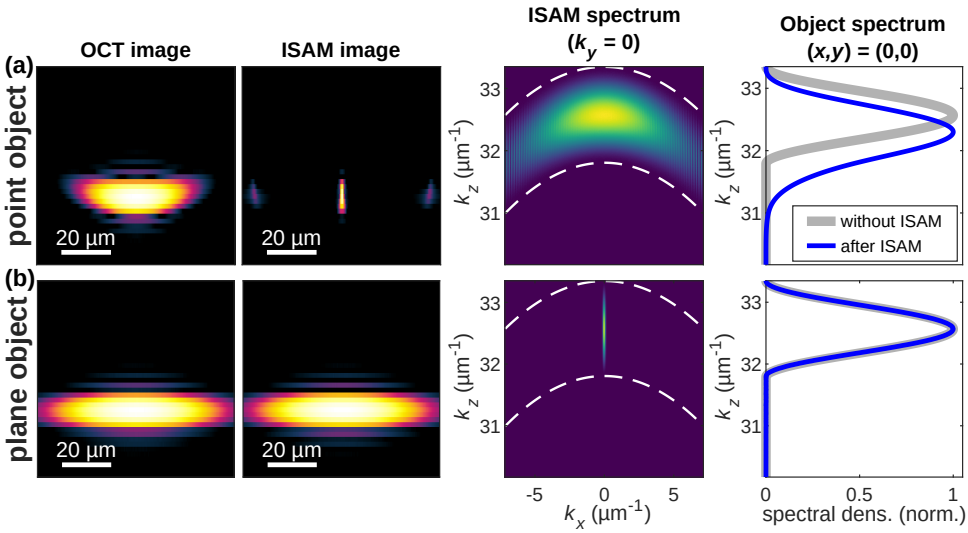

Figure 4.7: Dependence of the axial object spectrum after ISAM on the object shape. (a) OCT point object intensity before and after ISAM. After ISAM the spectrum bends downward at high lateral frequencies. The spectrum evaluated along k_z is shifted towards lower k_z and broadened. A horizontal plane (b), however, has a narrow lateral spectrum, giving a nearly unaltered axial object spectrum after ISAM. The white dashed lines in the ISAM spectrum indicate the boundaries of the measured OCT data.

Figure 4.7 illustrates this with two extreme examples: a point object, in (a), and a horizontal plane object, in (b). The point object contains many high lateral spatial frequencies, which ISAM maps to lower k_z values. After the lateral inverse DFT, this results in a downshifted and broadened spectrum in the k_z direction. In contrast, a plane object contains a narrow lateral spatial frequency spectrum, see Fig. 4.7(b). ISAM leaves this axial spectrum unaltered as ISAM remapping occurs at lateral frequencies where there is negligible signal. The dependence of the spectral shape on the local object structure is problematic for SE-OCT as it requires a well-defined spectral shape for spectral normalization. We observed that applying the processing in this order resulted in strong side lobes and a poor axial resolution, especially for structures that had a different spectral content than the used reference spectrum.

The second option does not suffer from axial spectrum ambiguity, but as the signal of small scatterers in the object is smeared out over a large lateral frequency range, the SNR will be low and the spectral estimation not effective. Simulations with this approach showed a lot of artifacts and were thus not satisfactory.

In the proposed method of first applying MIAA followed by ISAM, the data can be uniformly reshaped using the shape of the source spectrum, which is independent of the lateral spectral content of the sample. Even though the axial resolution improvement worsens with the decreasing SNR outside the focal plane, for a large axial range the improvement is still significant, as shown in the current work.

SE-OCT works best in combination with sparse, high-SNR samples [17, 18, 36]. Thus, the performance of the proposed method to non-sparse samples with low SNR will probably give less resolution improvement. However, RFIAA showed a faithful reconstruction of a non-sparse skin sample [18], sharpening the high SNR features while maintaining a good contrast in the non-sparse tissue. Thus the proposed MIAA+ISAM, though less effective, may still be advantageous also for less sparse objects.

A potential disadvantage of MIAA+ISAM is the SNR-caused depth-dependent axial resolution. However, the variation in axial resolution is not as large as the lateral blurring without defocus correction. Moreover, the resolution is still better than the DFT approach over the full depth range.

Using a narrow-band light source greatly simplifies the optical design, especially of the spectrometer. In this work, we used a custom-built OCT setup, with a custom high-resolution spectrometer. However, the optical design can be largely simplified while maintaining similar results. As only 13% of the maximum imaging depth z_{max} was used, a reduction by a factor 6 of the spectral resolution or the number of spectrometer pixels (from 3072 to 512 pixels) could be done without significantly compromising the imaging results. Moreover, by optimizing the coupling of the fiber source power or increasing the SLD power, the exposure time could be reduced allowing for a faster acquisition with a similar SNR. These adaptions would enhance the applicability of our method.

Another promising hardware adaption could be to add a second SLD and interpolate the signal between the two SLDs using MIAA. If, for example, the blue SLD at 450 nm (EXS210099-03, Exalos) would be added, the 60 nm in between the two spectra could be interpolated and the 70 nm wide spectrum would yield an

axial resolution of 1 µm. This would however require a larger spectrometer which complicates the design, like with the green-red combination [14].

The presented results demonstrated that the phase accuracy of IAA-based SE-OCT is sufficient to allow for coherent post-processing using ISAM and CAO. This opens the door to its application to other coherent or phase-based processing methods, such as OCT vibrometry [37], polarization-sensitive OCT, and phase-resolved Doppler OCT imaging at high resolution. CAO could also be combined with induced astigmatism, to improve the SNR outside the focal plane for a better axial resolution without compromising the lateral resolution [9].

4.6. Conclusion

In this work, we developed a combined spectral data extrapolation using MIAA with interferometric synthetic aperture microscopy (ISAM) and computational adaptive optics (CAO). We applied this method to data from an OCT setup with a narrow, 6.5 nm, bandwidth SLD source at 510 nm and a high numerical aperture. We obtained a factor 1.8 to 5 axial resolution improvement reaching close to a single µm axial resolution. We obtained a lateral resolution of 0.8 µm over a depth range of 16 (experimental) or 18 (simulations) the nominal depth of field. The close to isotropic resolution resulted in a clear improvement of image quality and optical sectioning on a relevant biological sample. The results show that the accuracy of RFIAA spectral estimation OCT is sufficient for coherent post-processing. Using a computationally efficient implementation of MIAA, the volume image processing time was in the order of minutes. Our findings pave the way for a wider application of cost-effective visible range SLD sources with a narrow bandwidth, as well as for the application of SE-OCT in combination with phase-sensitive OCT imaging.

Data availability

Data and code underlying the results presented in this chapter are available in Ref. [38].

References

[1] Y.-Z. Liu, F. A. South, Y. Xu, P. S. Carney, and S. A. Boppart, *Computational optical coherence tomography,* Biomedical Optics Express **8**, 1549 (2017).

[2] J. A. Izatt and M. A. Choma, *Theory of optical coherence tomography,* in *Optical coherence tomography* (Springer, 2008) pp. 47–72.

[3] A. D. Aguirre and J. G. Fujimoto, *Optical coherence microscopy,* in *Optical coherence tomography* (Springer, 2008) pp. 505–542.

[4] A. Lichtenegger, J. Gesperger, B. Kiesel, M. Muck, P. Eugui, D. J. Harper, M. Salas, M. Augustin, C. W. Merkle, C. K. Hitzenberger, *et al.*, *Revealing brain pathologies with multimodal visible light optical coherence microscopy and fluorescence imaging,* Journal of Biomedical Optics **24**, 066010 (2019).

[5] R. Leitgeb, M. Villiger, A. Bachmann, L. Steinmann, and T. Lasser, *Extended focus depth for Fourier domain optical coherence microscopy,* Optics Letters **31**, 2450 (2006).

[6] I. Grulkowski, K. Szulzycki, and M. Wojtkowski, *Microscopic OCT imaging with focus extension by ultrahigh-speed acousto-optic tunable lens and stroboscopic illumination,* Optics Express **22**, 31746 (2014).

[7] L. Yu, B. Rao, J. Zhang, J. Su, Q. Wang, S. Guo, and Z. Chen, *Improved lateral resolution in optical coherence tomography by digital focusing using two-dimensional numerical diffraction method,* Optics Express **15**, 7634 (2007).

[8] T. S. Ralston, D. L. Marks, P. Scott Carney, and S. A. Boppart, *Interferometric synthetic aperture microscopy,* Nature Physics **3**, 129 (2007).

[9] S. G. Adie, B. W. Graf, A. Ahmad, P. S. Carney, and S. A. Boppart, *Computational adaptive optics for broadband optical interferometric tomography of biological tissue,* Proceedings of the National Academy of Sciences **109**, 7175 (2012).

[10] A. Ahmad, N. D. Shemonski, S. G. Adie, H.-S. Kim, W.-M. W. Hwu, P. S. Carney, and S. A. Boppart, *Real-time in vivo computed optical interferometric tomography,* Nature Photonics **7**, 444 (2013).

[11] A. Lichtenegger, D. J. Harper, M. Augustin, P. Eugui, M. Muck, J. Gesperger, C. K. Hitzenberger, A. Woehrer, and B. Baumann, *Spectroscopic imaging with spectral domain visible light optical coherence microscopy in Alzheimer's disease brain samples,* Biomedical Optics Express **8**, 4007 (2017).

[12] M. Münter, M. Pieper, T. Kohlfaerber, E. Bodenstorfer, M. Ahrens, C. Winter, R. Huber, P. König, G. Hüttmann, and H. Schulz-Hildebrandt, *Microscopic optical coherence tomography (mOCT) at 600 kHz for 4D volumetric imaging and dynamic contrast,* Biomedical Optics Express **12**, 6024 (2021).

[13] X. Shu, L. Beckmann, and H. F. Zhang, *Visible-light optical coherence tomography: a review,* Journal of Biomedical Optics **22**, 121707 (2017).

[14] A. Lichtenegger, M. Salas, A. Sing, M. Duelk, R. Licandro, J. Gesperger, B. Baumann, W. Drexler, and R. A. Leitgeb, *Reconstruction of visible light optical coherence tomography images retrieved from discontinuous spectral data using a conditional generative adversarial network,* Biomedical Optics Express **12**, 6780 (2021).

[15] S. Khan, K. Neuhaus, O. Thaware, S. Ni, M. J. Ju, T. Redd, D. Huang, and Y. Jian, *Corneal imaging with blue-light optical coherence microscopy,* Biomedical Optics Express **13**, 5004 (2022).

[16] P. D. Woolliams, R. A. Ferguson, C. Hart, A. Grimwood, and P. H. Tomlins, *Spatially deconvolved optical coherence tomography,* Applied Optics **49**, 2014 (2010).

[17] X. Liu, S. Chen, D. Cui, X. Yu, and L. Liu, *Spectral estimation optical coherence tomography for axial super-resolution,* Optics Express **23**, 26521 (2015).

[18] J. De Wit, K. Angelopoulos, J. Kalkman, and G.-O. Glentis, *Fast and accurate spectral-estimation axial super-resolution optical coherence tomography,* Optics Express **29**, 39946 (2021).

[19] A. Kumar, W. Drexler, and R. A. Leitgeb, *Subaperture correlation based digital adaptive optics for full field optical coherence tomography,* Optics Express **21**, 10850 (2013).

[20] P. Stoica, J. Li, and J. Ling, *Missing data recovery via a nonparametric iterative adaptive approach,* IEEE Signal Processing Letters **16**, 241 (2009).

[21] J. Kalkman, *Fourier-domain optical coherence tomography signal analysis and numerical modeling,* International Journal of Optics **2017** (2017).

[22] T. Yardibi, J. Li, P. Stoica, M. Xue, and A. B. Baggeroer, *Source localization and sensing: A nonparametric iterative adaptive approach based on weighted least squares,* IEEE Transactions on Aerospace and Electronic Systems **46**, 425 (2010).

[23] G.-O. Glentis and A. Jakobsson, *Efficient implementation of iterative adaptive approach spectral estimation techniques,* IEEE Transactions on Signal Processing **59**, 4154 (2011).

[24] G.-O. Glentis and A. Jakobsson, *Time-recursive IAA spectral estimation,* IEEE Signal Processing Letters **18**, 111 (2010).

[25] T. S. Ralston, D. L. Marks, P. S. Carney, and S. A. Boppart, *Inverse scattering for optical coherence tomography,* Journal of the Optical Society of America A **23**, 1027 (2006).

[26] K. C. Zhou, R. Qian, A.-H. Dhalla, S. Farsiu, and J. A. Izatt, *Unified k-space theory of optical coherence tomography,* Advances in Optics and Photonics **13**, 462 (2021).

[27] X. Attendu, R. M. Ruis, C. Boudoux, T. G. Van Leeuwen, and D. J. Faber, *Simple and robust calibration procedure for k-linearization and dispersion compensation in optical coherence tomography,* Journal of Biomedical Optics **24**, 056001 (2019).

[28] M. Wojtkowski, V. J. Srinivasan, T. H. Ko, J. G. Fujimoto, A. Kowalczyk, and J. S. Duker, *Ultrahigh-resolution, high-speed, Fourier domain optical coherence tomography and methods for dispersion compensation,* Optics Express **12**, 2404 (2004).

[29] N. Nassif, B. Cense, B. Park, M. Pierce, S. Yun, B. Bouma, G. Tearney, T. Chen, and J. De Boer, *In vivo high-resolution video-rate spectral-domain optical coherence tomography of the human retina and optic nerve,* Optics Express **12**, 367 (2004).

[30] J. de Wit, S. Tonn, G. Van den Ackerveken, and J. Kalkman, *Quantification of plant morphology and leaf thickness with optical coherence tomography,* Applied Optics **59**, 10304 (2020).

[31] G. M. Hale and M. R. Querry, *Optical constants of water in the 200-nm to 200-µm wavelength region,* Applied Optics **12**, 555 (1973).

[32] F. Huang, S. L. Schwartz, J. M. Byars, and K. A. Lidke, *Simultaneous multiple-emitter fitting for single molecule super-resolution imaging,* Biomedical Optics Express **2**, 1377 (2011).

[33] A. Kumar, T. Kamali, R. Platzer, A. Unterhuber, W. Drexler, and R. A. Leitgeb, *Anisotropic aberration correction using region of interest based digital adaptive optics in Fourier domain OCT,* Biomedical Optics Express **6**, 1124 (2015).

[34] L. Glandorf, P.-J. Marchand, T. Lasser, and D. Razansky, *Digital aberration correction enhances field of view in visible-light optical coherence microscopy,* Optics Letters **47**, 5088 (2022).

[35] D. Hillmann, C. Pfäffle, H. Spahr, S. Burhan, L. Kutzner, F. Hilge, and G. Hüttmann, *Computational adaptive optics for optical coherence tomography using multiple randomized subaperture correlations,* Optics Letters **44**, 3905 (2019).

[36] Y. Ling, M. Wang, Y. Gan, X. Yao, L. Schmetterer, C. Zhou, and Y. Su, *Beyond Fourier transform: super-resolving optical coherence tomography,* arXiv preprint arXiv:2001.03129 (2020).

[37] S. S. Gao, P. D. Raphael, R. Wang, J. Park, A. Xia, B. E. Applegate, and J. S. Oghalai, *In vivo vibrometry inside the apex of the mouse cochlea using spectral domain optical coherence tomography,* Biomedical Optics Express **4**, 230 (2013).

[38] J. de Wit, G.-O. Glentis, , and J. Kalkman, *Computational 3D resolution enhancement for optical coherence tomography with a narrowband visible light source,* https://doi.org/10.5281/zenodo.7870795 (2023).

5

In-vivo label-free 3D OCT imaging of downy mildew in plant leaves

Microscopic imaging is a powerful tool to study plant-pathogen interactions. However, it often relies on invasive histological techniques like tissue clearing and staining or, for in-vivo imaging, on transgenic pathogen strains expressing fluorescent markers. Optical coherence tomography (OCT) can perform microscopic in-vivo imaging without requiring fluorescent markers. However, conventional OCT lacks specificity to distinguish plant tissue from pathogen tissue. Here, we demonstrate dynamic OCT (dOCT) to create in-vivo functional 3D contrast for Bremia lactucae hyphae. The downy mildew pathogen in lettuce displays a high signal in dOCT amplitude fluctuation frequencies between 0.7 and 4.8 Hz and less in other frequency bands. We use this dynamic contrast to image B. lactucae in 3D in live lettuce leaf tissue with limited sample preparation. Comparison with brightfield microscopy images of the sample ex-vivo validates the imaging results. The 3D images are segmented to quantify B. lactucae hyphae volume and length in different lettuce genotypes. A longitudinal study shows the growth of B. lactucae over the course of several days. These results demonstrate the potential of dOCT for studying plant-pathogen interactions.

This chapter is in preparation to be submitted: **Jos de Wit**, Sebastian Tonn, Mon-Ray Shao, Guido Van den Ackerveken, and Jeroen Kalkman, *In-vivo label-free 3D OCT imaging of downy mildew in plant leaves*

5.1. Introduction

Plant pathogens are a severe problem in agriculture as they can destroy crops or significantly reduce their yield [1]. Thus plant resistance against common pathogens, such as oomycetes, viruses, bacteria, and nematodes, is an essential trait that growers require for their crops. As pathogens evolve to break plant resistance, plant breeders seek to develop crops with more robust and quantitative resistance based on a combination of different plant immune responses [2–4]. Understanding the interaction between the plant and the pathogen is essential to develop crops with a higher disease resistance. Imaging is one of the most important tools for gaining insights into the plant's resistance mechanisms.

As pathogens interact with the plant at microscopic level, direct imaging of the plant-pathogen interaction requires a microscopic resolution. Fluorescence microscopy with transgenic plants or pathogens expressing fluorescent marker proteins for contrast is widely used in plant imaging, particularly *in vivo*. This approach is limited by the availability of such transgenic organisms, and therefore excludes non-model organisms that are not amenable to genetic modification or are very difficult to genetically transform. One of such non-model plant-pathogen systems is infection of the oomycete *Bremia lactucae*, a biotrophic downy mildew pathogen, in lettuce plant leaves. Lettuce is an important crop and resistance to *B. lactucae* is important for growers. The lack of fluorescent markers for *B. lactucae* requires non-fluorescent imaging techniques, which are currently not available for *in-vivo* imaging. Therefore, the microscopic interaction of *B. lactucae* with lettuce can only be studied with destructive histological techniques that do not allow *in vivo* imaging. Thus there is a need for label-free and *in-vivo* microscopic imaging that could visualize the plant-pathogen interaction.

Optical coherence tomography (OCT) is such a label-free *in-vivo* imaging method that can image plant tissue at resolutions of pathogen structures. Spectral domain OCT (SD-OCT) has a large penetration depth inside the scattering plant tissue, especially when combined with water-infiltration of the plant leaf [5]. However, conventional OCT imaging based on scattering contrast cannot distinguish between plant and pathogen tissue.

Here, we propose the use of functional tissue contrast based on biospeckle intensity fluctuations or dynamic light scattering to enhance the specificity of OCT imaging. Biospeckle can be used to observe activity of sub-resolution scatterers in biological tissue and can be implemented with a variety of coherent optical imaging methods [6, 7]. Biospeckle variance OCT has been applied to detect the response of plants to stress [8, 9]. However, these studies use the average biospeckle signal over a large region to distinguish between plants, rather than to create contrast in 3D within the tissue. Instead of biospeckle variance, which does not directly incorporate the time scale of the dynamics, we propose to use the time-frequency amplitude spectrum (AS) of the fluctuations in the OCT amplitude of the scattered signal. In this method a color is assigned to the average AS in a frequency band. This allows to create functional contrast at voxel level that, for example, can be used to distinguish different cell types [10]. This method, also called dynamic OCT (dOCT), could create or increase contrast between pathogen tissue and plant tissue,

as they have a different sub-cellular activity.

Here we apply dOCT to visualize *B. lactucae* colonization in lettuce plant leaves. First, we demonstrate dOCT imaging of *B. lactucae* in living lettuce leaves. This consists of contrast optimization by choosing appropriate frequency bands, proof of principle dOCT imaging validated by *ex-vivo* microscopic imaging of the same sample, and investigating the origin of the contrast with *B. lactucae* spores.

Second, we apply this method in a quantitative study comparing the *B. lactucae* colonization of three lettuce varieties with varying levels of resistance. This quantification includes developing a method to segment and analyze the 3D structure of the *B. lactucae* hyphae.

Third, we follow the growth of *B. lactucae* inside the leaf over the course of a few days. These experiments show the potential of longitudinal dOCT for label-free imaging of plant-pathogen interaction and disease severity quantification.

5.2. *B. lactucae* imaging with dynamic OCT

Figure 5.1(a) shows the dOCT imaging and processing pipeline. First, a series of B-scans is obtained at the same location over a time of 1.5 seconds. The fluctuations of the amplitude in time contains information about the small scale dynamics in the tissue, which characterizes the type of tissue. Static structures give a stationary signal, while structures with strong sub-cellular motion, such as *B. lactucae* hyphae, give a fluctuating signal. Second, the time-scale of the motion is captured in the AS, which is obtained by applying a Fourier transform. The AS is divided in three bands: low, medium and high frequency content. The average amplitude in each band gives the color intensity value for the blue, green and red channel respectively in a false colour image. Third, this process is repeated at multiple B-scans resulting in a 3D image with dOCT contrast.

The frequency bands are chosen such that we obtain a strong contrast between *B. lactucae* and plant cell walls. Figure 5.1(b) shows the contrast optimization process. From a 2D dOCT image *B. lactucae* was manually segmented and plant cells above a threshold outside the *B. lactucae* region were selected as plant cells. Their amplitude spectra (AS) were obtained and compared. The AS shows that plant cells have a large amplitude at 0 Hz and the AS decays almost fully at 0.7 Hz, the first non-zero frequency. In contrast, *B. lactucae* has a slowly decaying AS, while having fewer signal than plant tissue at 0 Hz, the stationary component. Thus *B. lactucae* gives a relatively high signal for intermediate frequencies, which we attribute to their sub-cellular motion. Plant cells give a relatively high signal at 0 Hz, which corresponds to a stationary object. Note that the sharp peaks around 16 and 27 Hz are due to fixed pattern noise and are not consistently present in the plant tissue pixels.

The difference in the AS between *B. lactucae* and plant cells is even more clear from analyzing their ratio in the middle right panel. At 0 Hz, the ratio is low, indicating that it correlates more strongly with plant cells. The 0 Hz signal was chosen as the blue color band, highlighting stationary tissue structures. The AS ratio is high for frequencies between 0.7 Hz and 4.8 Hz, which we chose as the green color band. The signal at these intermediate frequencies highlights sub-resolution motion

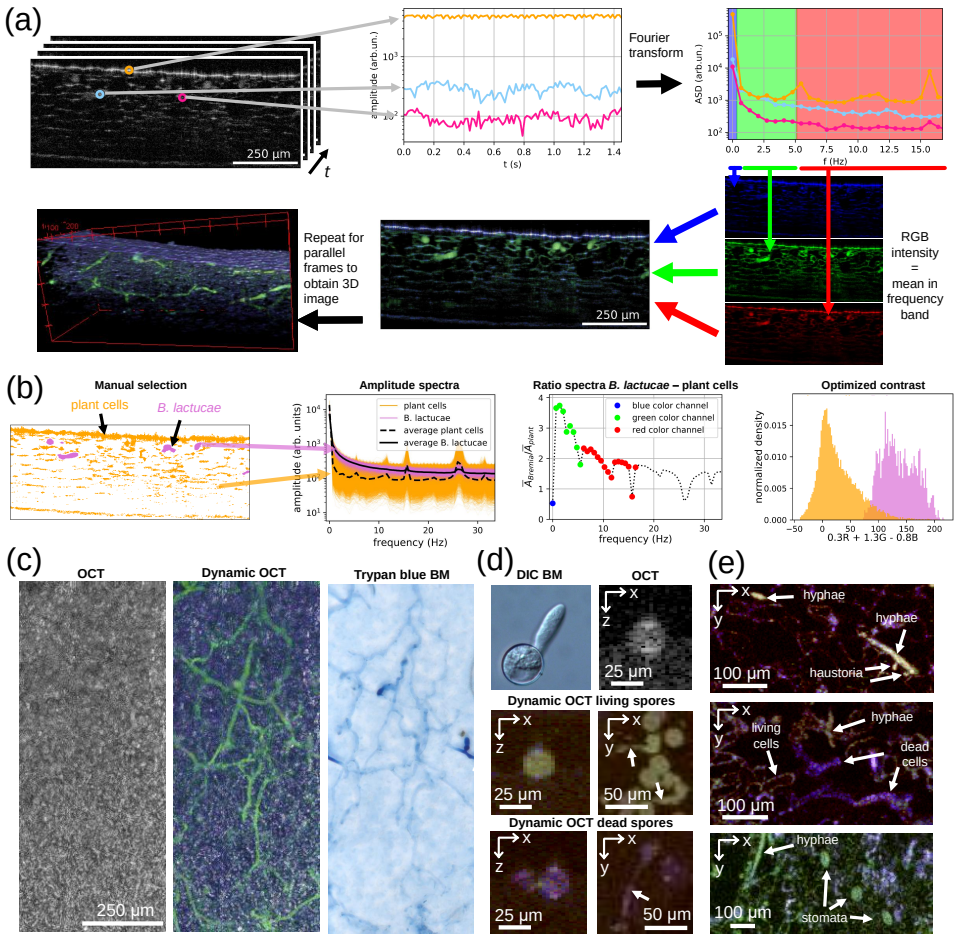

Figure 5.1: (a) Overview of dynamic OCT processing: a series of B-scans are acquired and for each pixel the amplitude over time is Fourier transformed to obtain the amplitude spectrum (AS). The log of the mean AS in three frequency bands provide the intensity for the three colors, resulting in a (false colored) RGB dynamic OCT image. Repeating this for each B-scan gives a 3D dOCT image. (b) Dynamic OCT contrast analysis between between *B. lactucae* and plant cell walls. The ratio between the average AS of *B. lactucae* and plant cell walls spectrum gives a values below 1 for 0 Hz frequency (blue), high values for 0.7-4.8 Hz (green) and medium values for 5.5-16.4 Hz (red). Combining the color channels as $0.3R + 1.3G - 0.8B$ gives good separation between *B. lactucae* and plant tissue (right). (c) The maximum intensity projection of the normal OCT image, the dynamic OCT image and the tryphan blues stained brightfield microscopy (BM) image of the same sample. (d) Comparison of DIC microscopy and dOCT on alive and dead spores. (e) Example en face images of infected lettuce leaves with different features indicated.

at a low speed, such as in *B. lactucae* hyphae. The high frequencies (5.5-16.4 Hz), chosen as the red color band, show a lower AS ratio than intermediate frequencies, but as the value is higher than 1 it still correlates more with *B. lactucae* than with plant cells. Note that in the shown dOCT images plant cells also have green and

red components, which we attribute to dynamic processes inside the cell, such as cytoplasmic streaming. The false-colored dynamic OCT images do not give a binary contrast between plant cells and *B. lactucae*, but while giving good contrast between plant tissue and *B. lactucae*, it also reveals distinct biological activity of different tissue types. For segmentation and quantification of *B. lactucae* colonization, a binary contrast is needed, which is obtained by combining the signals from the color channels. The optimized contrast is found to be 0.3R+1.3G+0.8B that gives a good separation between plant cells and *B. lactucae* as shown in the histogram.

To validate that the bright green structures in the images are indeed *B. lactucae* hyphae, multiple leaf discs were imaged with dOCT, and subsequently stained with Trypan blue, cleared, and imaged with brightfield microscopy (BM) (see Methods). Figure 5.1(c) shows the convincing correspondence between the green structures in the dOCT image and the trypan blue-stained hyphae in a BM image. Note that the conventional OCT does not provide distinctive contrast between *B. lactucae* hyphae and plant cells. This clearly shows the contrast enhancement of dOCT.

The origin of the dynamic contrast was further verified using *B. lactucae* spores in Fig 5.1(d). Using BM with differential interference contrast (DIC) (see Methods), the motion of the scattering cellular content in the (germinating) spores could be visualized (Visualization 1). Real time OCT B-scan imaging shows this motion as fluctuating speckle inside the spore, similar to the speckle fluctuation in hyphae growing inside a leaf. The dynamic OCT image of living spores shows the bright green color of the spores and germ tubes (see arrows). Note that the static top and bottom interface of the spore have a blueish color. Killing the spores with a short exposure to heat from a flame stopped the biological activity inside the (germinating) spores. This was immediately visible in the OCT images where speckle became static, resulting in a a purple (red and blue combined) colored dOCT image of the spores. These imaging results of germinating *B. lactucae* spores confirm that the dOCT contrast of hyphae comes from the biological activity inside the living *B. lactucae* structures. While BM with DIC contrast only visualizes the sub-cellular motion of spores in a transparent medium, dOCT can also sense and localize this dynamic signal in 3D within a living leaf and thus visualize *B. lactucae* hyphae *in-vivo*.

Figure 5.1(e) shows examples of *in-vivo* en face images of *B. lactucae* infected leaves. The top image shows a clear hyphae with two haustoria (a specialized structure that penetrate the plant cell to suppress its immune system and extract nutrients). Note that the plant cell walls are red-green colored due to small scale cellular activity of plant cells. The blue accents correspond to the strong reflection of the horizontally oriented cell wall surfaces that are more static. The middle image shows an infection in a resistant lettuce genotype, whose immune response triggers cell death. Dead plant cells give a strong static signal, which is blue in the dOCT image. Here the exact color of the *B. lactucae* is less distinct from that of living plant cells, but combined with their structure they can still be distinguished, especially when using the full stack of en face images. The bottom image shows the epidermal layer, where the epidermal cells are clearly visible, with blue-colored patches for the strongly reflecting top interface of the leaf. Three stomata are visible in a bright green color, indicating that they exhibit a lot of sub-cellular activity. This

could be a response to the near-infrared OCT imaging light (820-980 nm) or an inherent property of these cells. As we also observed this in non-infiltrated leaves, this activity is not caused by leaf infiltration. These three images illustrate different functional information that can be obtained from dOCT images beside the clear *B. lactucae* contrast and indicate the potential of dOCT to not only image pathogens, but also distinguish different plant cells.

5.3. Quantification of *Bremia lactucae* in three lettuce genotypes

Accurate imaging of the length or volume of *B. lactucae* hyphae can be an objective and precise method to quantify the susceptibility of a lettuce genotype to disease. To test this, two experimental replicates, each of 12 inoculated leaf discs (24 in total) of three lettuce varieties with different levels of resistance to *B. lactucae* were imaged five days post inoculation (dpi) (Fig. 5.2(a)). Imaging was performed at two random areas per leaf disc to give a total of 48 volumetric images, which were then segmented with the pipeline visualized in Fig. 5.2(b). First, the optimum *B. lactucae* contrast, as displayed in the histogram in Fig. 5.1(b), was calculated. Second, a 3D

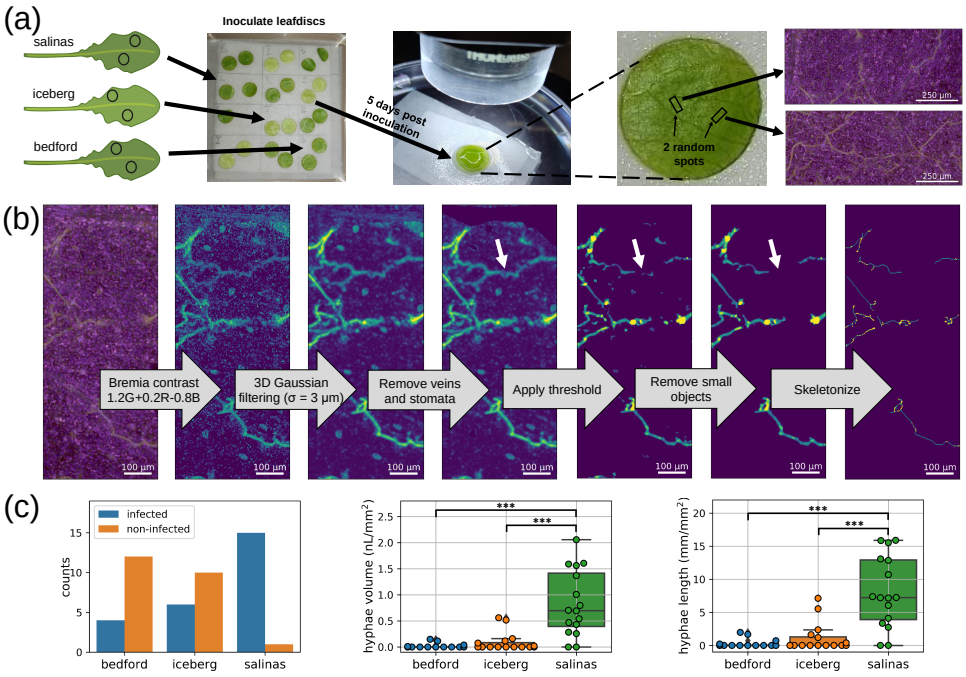

Figure 5.2: (a) Overview over the dOCT imaging process for *B. lactucae* resistance quantification. (b) *B. lactucae* segmentation pipeline for dynamic OCT volumes. The images are a maximum intensity projection (before threshold) or an axial sum of the non-zero pixels (after threshold). (c) Different dOCT-based measures for degree of *B. lactucae* infection per volume for each genotype.

Gaussian filtering with a small ($\sigma = 3$ µm) kernel enhanced the signal of the dense hyphae, with respect to that of thin plant cell walls. Third, leaf veins and stomata that appeared bright in the *B. lactucae* contrast image due to their sub-cellular activity were manually segmented out. Fourth, a global intensity threshold was applied. The threshold value was identical for all volume images and was chosen such that most noise was removed. Fifth, small objects were removed with a filter, resulting in the segmented *B. lactucae* hyphae. Sixth, the *B. lactucae* voxels were summed to obtain their volume, while the amount of voxels after skeletonization was summed as a measure of hyphae length. In our processing, some less intense hyphae (e.g. indicated by the white arrow) were lost, but the majority of the hyphae was accurately detected, making the segmented volume or length still a good measure of the degree of colonization.

Each of the 48 3D dOCT images was also manually investigated on the presence of *B. lactucae* hyphae, which results are shown in the histogram in Fig. 5.2(c). The resistant Bedford variety had 4/16 volumes colonized. Within these few infected Bedford samples, the amount of hyphea was small, with a volume below 0.2 nl/mm^2 and length below 3 mm/mm^2. This shows Bedford does not get infected easily and that, when infected, the immune response in Bedford limits the hyphae growth. The intermediate-resistant Iceberg variety had 6/16 colonized volumes. This are only a few more than Bedford, but the *B. lactucae* hyphae had spread wider indicated by the larger hyphae volume and length. Iceberg has a few samples which are more heavily infected (volume >0.5 nl/mm^2 and length >5 mm/mm^2), but the difference between Bedford and Iceberg is not significant (Mann-Whitney test $p = 0.16$ and $p = 0.17$ for volume and length respectively), likely due to the limited number of infected samples. The susceptible Salinas variety had 15/16 colonized volumes, and the *B. lactucae* hyphae were present throughout the whole volume. This is also reflected in the quantified volume up to 2 nL/mm^2 and length up to 17 mm/mm^2. The difference with both Iceberg and Bedford are significant (respectively $p = 9.3 \cdot 10^{-5}$ and $p = 1.2 \cdot 10^{-5}$ for volume and $p = 6.8 \cdot 10^{-5}$ and $p = 1.2 \cdot 10^{-5}$ for length). The results show the potential of dOCT to quantify infection and distinguish between genotypes with different degrees of susceptibility.

5.4. Longitudinal imaging of *B. lactucae* growth

The strength of OCT to image label-free and *in-vivo* enables imaging the progress of the pathogen infection over time. To demonstrate this ability, we imaged infected leaf discs from the susceptible salinas variety twice a day from 3 to 7 dpi (see methods). Figure 5.3(a) gives an example of a dOCT imaging sequence where the progress of the infection over the course of the experiment is clearly visible. Next, the hyphae were segmented in the 3D dOCT images of the last time points (where the network is complete), manually cleaned up (see methods), and divided into smaller point clouds based on the moment of first appearance. Figure 5.3(b) shows the point cloud, colored by the time period in which the hyphae have grown. Interesting to observe is that within a single time interval of 12 hours often complete, long hyphae are formed, which then either stop growing or deviate into a deeper layer that is not imaged due to the limited depth of field. The 3D informa-

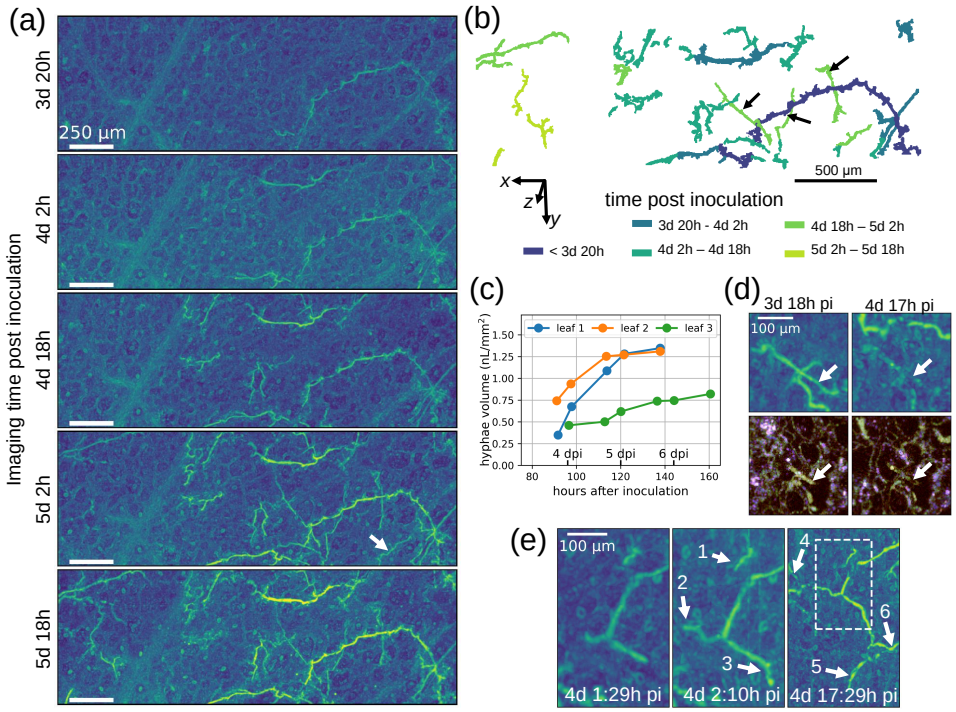

Figure 5.3: (a) Progression of *B. lactucae* infection over time visualized by the maximum intensity projection of Gaussian filtered *B. lactucae* contrast images. (b) The segmented point cloud of *B. lactucae* hyphae, colored by the time period of growth. (c) *B. lactucae* hyphae volume over time for several samples. (d) A close up of hyphea that loose their activity while new active hyphae develop. (e) A close up of two images taken with 40 minutes in between, and a zoom-out image 15 hours later. The arrows indicate the newly grown hyphae and the white-dashed box the area of the first two images.

tion that is obtained with OCT is helpful to interpret the origin and growth process of the hyphae. For example, the hyphae indicated by arrows grew at a different depth from the older hyphae, and thus do not originate in this older hyphae as branch. The hyphae volume over time of this and two other samples are plotted in Fig. 5.3(c). While the amount of samples is insufficient to draw biological conclusions from the volume growth over time, the figure shows the potential of measuring disease progression in time in a quantitative way.

An interesting observation during the time-lapse was that sometimes hyphae loose their activity and are not visible in later images. The white arrow in Fig. 5.3(a) indicates such a hyphae. Sometimes this is caused by the focus being at a different depth, but often the cause is biological, namely a change of activity in the hyphae. Figure 5.3(d) shows an image where over the course of a day a hyphae (white arrow) almost disappeared in the *B. lactucae* contrast image (top row). When looking at a single en face dOCT image, the hyphae that was first bright green has become hollow with a more brown edge, a similar color as that of plant cell walls in dOCT. Note that the freshly grown hyphae in the same image proves that

the reduced activity is not the result of a poor image quality. We observed this effect also in other time-lapse images, where, especially after sporulation, many hyphae lost activity. Most likely these hyphae are in the process of dying off, and the scattering content has been pushed to the region where the disease is active now (e.g. the sporangiophores). Though this effect can complicate the precise quantification of all hyphae, it can also provide unique insights in the vitality of *B. lactucae* hyphae, for example in response to disease control measures.

To study *B. lactucae* growth speed in a short time frame, two images were obtained of the same sample with 40 minutes in between while the sample remained infiltrated (see Fig. 5.3(e)). The shown close-up shows three hyphae tips that grew in this 40 minutes period. By measuring the added hyphae length in the 3D dataset (36 µm, 70 µm, and 75 µm for tip 1-3 respectively), we could estimate the hyphae growth speed at 54 µm/h, 105 µm/h, and 115 µm/h. The next image visualizes the same area 15 h later and shows that the hyphae of tip 2 and 3 have grown over a significant distance and branched out, while the hyphae at tip 1 barely grew further. The extra distance the hyphae grew over this 15 hour is about 0.4 mm for branch 4, 0.5 mm for branch 5 and at least 0.5 mm for branch 6, which grew out of the imaged area. This corresponds with lower grow speeds of 25-35 µm/h. However, the active growth speed is probably higher, as the growth stopped or the hyphae grew out of focus, during the 15 h period as the following images (not shown here) showed no further growth.

Summarizing, the time-lapse measurements shows the potential of dOCT imaging to visualize and quantify the progression of *B. lactucae* infection over the course of several days. To our knowledge this is the first time this has been visualized and quantified. It opens up ways to investigate the vitality and to quantify the growth speed of individual *B. lactucae* hyphae and there dependence on resistance.

5.5. Discussion

In this work, we demonstrated that dynamic OCT can image the presence and growth of *Bremia lactucae* in lettuce *in-vivo* in 3D, *in-vivo*, and over time. Using segmentation, we could quantify the volume and length of *B. lactucae* hyphae in the imaged sample and estimate the rate of growth. This imaging method has a great potential to yield new insights in the interaction of plant and pathogens.

Further research could deepen the understanding of the dynamic OCT signal and its relation to biological processes. Some insight already was obtained from imaging germinating spores using DIC brightfield microscopy. However, better understanding of the contrast and expected variation in contrast could yield more functional biological information about, for example the vitality or activity of the pathogen. Also, the correlation of AS at different frequencies with biological activity could be further investigated. The frequency content of the AS may be specific enough to distinguish between different biological processes such as nutrient transport and plant growth and thus identify where they take place. The examples of dead plant cells and reduced activity in previously active hyphae show that more biological information is contained in the dynamic signal which can be explored in future studies.

Infiltrating the leaves, necessary to obtain sufficient imaging depth, could affect the plant cells and the plant-pathogen interaction. PFD, used for the longitudinal study, does not require pressure and is believed to have minimal physiological impact on the plant [11]. The longitudinal study showed that *B. lactucae* growth was not stopped due to the infiltration cycles, and even the water-infiltrated leaves of experiment 1 showed sporulation the day after imaging. These results show that infiltration, especially with PFD is compatible with *in-vivo* imaging and does not disrupt *B. lactucae* infection.

Dynamic OCT generates a large amount of data for imaging a small volume with high resolution. This can be reduced after calculating the AS and selecting the region of interest but is still a limiting factor for large scale application. Non-linear sampling in time could reduce the required amount of frames while still obtaining a reasonable contrast [12]. Note that the hyphae can be seen in real time by the fluctuating speckle in the normal OCT B-scan imaging mode (Visualization 1). Using real-time image processing with AI methods, trained by dOCT images, real-time B-scan dOCT imaging could be possible as well. Also for improving the accuracy and speed of segmentation, recent development in AI-based segmentation methods could be deployed [13].

The dOCT imaging can also be used to image pathogens other than *B. lactucae*. Similar contrast was obtained for downy mildew infection in radish and *Arabidopsis* leaves. Also for imaging roots infected with root-knot nematodes (Meloidogyne incognita), dOCT gave an enhanced contrast compared to normal OCT. For imaging bacteria, the resolution of OCT is not sufficient, though the activity of a bacterial colony or the plant-stress response may still give a dynamic OCT contrast that can be helpful in studying these diseases.

Concluding, this work shows the great potential of dOCT imaging for label-free *in-vivo* 3D imaging of plants. By quantifying the volume and length of the pathogen structures, we obtained quantitative data that relates to the susceptibility of the plant variety. The longitudinal study demonstrated that the imaging is compatible with the pathogen growth. Moreover, it enabled quantification of hyphae growth speed, as well as disease progression over the course of days. This opens the door to a new understanding of plant-pathogen interaction.

5.6. Methods

5.6.1. Imaging setup and dOCT processing

The OCT measurements were done with a Ganymede II HR spectral domain OCT setup (Thorlabs, Germany), also used in previous work [5]. The system has a 36 Hz A-scan rate and a center wavelength of 900 nm and a 160-nm bandwidth, resulting in a 2.1 µm axial resolution in tissue. The OCT system is used with a scan lens (OCT-LK2-BB, Thorlabs, Germany) and yields a lateral resolution of about 3 µm. Single B-scan data were acquired using ThorImage (version 5.4.1, Thorlabs), and 3D dynamic OCT data was acquired using a Python wrapper around a C++ module that was included in the ThorImage package. 3D scans were automatically divided into blocks of around 40 dynamic B-scans that were saved before starting

the next block. The B-scan repetition time (including overhead for scan mirror flight-back) was 14.6 ms and 29.3 ms for dynamic OCT with 100 and 50 frames, respectively, giving a total acquisition time of 1.46 s per dynamic B-scan. With a lateral sampling of 3 µm and a lateral scan width of 360 and 887 A-lines, the B-scan width was 1.08 mm and 2.66 mm respectively. The width on the slow axis was 600 µm for experiment 1 and 900 µm for experiment 2. The volume acquisition time was 4.9 minutes and 7.3 minutes for experiment 1 and experiment 2 respectively, excluding a few minutes per C-scan for saving the raw data in between the acquisition blocks.

The raw OCT data per B-scan was processed in the conventional way, consisting of subtracting the reference spectrum, linearization in wavenumber domain, spectral reshaping with a Hanning window, dispersion correction, an inverse discrete Fourier transform (DFT), and taking the absolute value. For the 50 or 100 B-scans at the same location, a DFT of the OCT amplitude data was taken in the time direction and the amplitude spectrum (AS) was obtained by taking the absolute value of the temporal DFT. The logarithm of the average value of the AS in the three frequency bands of 0 Hz (blue), 0.7 Hz to 4.8 Hz (green) and 5.5-16.4 Hz (red) was taken as intensity for the color channels. The dynamic range of the intensity that was mapped to the RGB value (0-255) was determined for each color channel separately. The top limit was the global maximum value of the average AS within the color band over all the data within the experiment (excluding coverslip interfaces). To obtain the lower limit of the dynamic range, the histogram was calculated over the voxels of the value before taking the logarithm. The peak location of the histogram is a measure for the noise intensity level, as most voxels only contain noise. The lower dynamic range limit was then the average histogram peak location over all volume images within the experiment. For displaying purposes (not for segmentation), the contrast of the dOCT images in the figures is enhanced by saturating the higher values. Sometimes there occurred a small drift in the axial position of the sample while saving raw data between acquisition blocks. This drift was corrected by an axial shift of the next block, with a value that was automatically determined based on the correlation of the neighboring frames.

5.6.2. dOCT image segmentation

The segmentation for experiment 1, the quantification of infection, was done in Python 3.7 according to the pipeline shown in Fig. 5.2(b). The standard deviation of the Gaussian filter kernel was chosen to be 1 pixel in lateral direction and 3/1.37 pixels in the axial direction, corresponding to 3 µm isotropically.

Masks to filter out veins and stomata were obtained in imageJ based on the maximum intensity projection (MIP) of the Gaussian filtered *B. lactucae* contrast. When the to be filtered out objects were close to hyphae, the mask was carefully made not to remove hyphae. If, based on the MIP image, there was doubt of what to remove, the dOCT image depth stack was investigated on the presence and location of hyphae close to the structures that had to be removed by the mask.

The global threshold was chosen at 40 (based on color values ranging from 0-255 and top and bottom reference values as discussed above). Small objects

were removed that had a size below 256 voxels with a connectivity of 4 voxels. The total hyphae volume then was obtained by counting the voxels after filtering, multiplying this number with the voxel volume and dividing it through the imaged surface area to get the volume per imaged area. The hyphae length was obtained by skeletonizing the segmented structures and multiplying it with the lateral pixel width (3 µm). This is an approximation as on a diagonal, the length could be $\sqrt{2}$ larger and vertically the distance between pixels is more than a factor 2 lower. The potential error is probably limited as most hyphae grow in the horizontal direction. Moreover, a potential bias would be similar for different genotypes making the comparison of colonization still trustworthy.

For the time-lapses the step of removing veins and stomata was first omitted, and the threshold was adapted per volume to obtain a good amount of hyphae while avoiding noise that could not be easily segmented out. The raw point clouds were further processed in using CloudCompare (V2.13.alpha). The point cloud of the last image of a time-series was manually cleaned up by removing stomata, veins and noise that was no *B. lactucae*. Disappeared hyphae or hyphae that were more clear in earlier images were added and aligned to obtain a pointcloud that was as complete as possible. Then the point cloud was divided based on the period that the hyphae grew, see Fig. 5.3(b). For cleaning up the point cloud, adding hyphae and determining the time of growth, the 3D dOCT image stack was used as guide to check for the presence of hyphae. This segmented point cloud is then used to quantify the *B. lactucae* colonization over time, by multiplying the amount of points in the point cloud with the voxel volume and dividing through the total imaged leaf area.

Growth speed between the images in Fig. 5.3(e) was estimated manually based on the image stack in ImageJ.

5.6.3. Sample preparation and experimental design

Lettuce plants were cultivated at 21°C under long-day conditions (16 h light, 100 µmol/m^2/s, 70% humidity). Leaf discs (10 mm diameter) from four-week-old plants were placed, with the abaxial side up, in petri dishes on moist filter paper and inoculated with *Bremia lactucae* (race Bl:33EU) by spraying them with sporangia suspension (40 sporangia/µL, experiment 1) or by dabbing with B. lactucae-infected lettuce cotyledons that were covered with sporangiophores (experiment 2). Inoculated discs were incubated at 16°C under short-day conditions (9 h light, 100 µmol/m^2/s). For experiment 1, leaf discs from three cultivars (Bedford, Iceberg, Salinas) were sampled at 5 dpi, vacuum infiltrated with tap water, and imaged with a water droplet on the surface to reduce the surface reflections. In experiment 2, discs of cultivar Salinas were imaged twice daily, at the beginning and end of the light period, between 3 and 7 dpi. For imaging, discs were submerged in perfluorodecalin (PFD, Sigma-Aldrich) in a custom mount, and covered with a cover slip. PFD infiltrates the air spaces in plant leaves without applying vacuum because of its low surface tension. After imaging, discs were rinsed with tap water and returned to the growth chamber. PFD infiltration had no visible damaging effects and disappeared within 30 minutes after rinsing. To visualize *B. lactucae* coloniza-

tion with brightfield microscopy (BM) for validation, the leaf discs were fixed in an ethanol-acetic acid solution (2:1, v/v) directly after dOCT imaging. Afterwards they were stained with trypan blue and cleared [14]. Germinating *B. lactucae* spores for imaging (Fig. 5.1(d) were prepared by dabbing lettuce seedlings covered in sporangiophores onto water agarose pads (1.5% agarose) to deposit spores and incubation at 16 °C in the dark for 2 h. For OCT imaging, the spores were submersed in water to reduce deformation and surface reflection intensity. For BM imaging, the spores were deposited on a wet microscope glass.

References

[1] S. Savary, L. Willocquet, S. J. Pethybridge, P. Esker, N. McRoberts, and A. Nelson, *The global burden of pathogens and pests on major food crops,* Nature Ecology & Evolution **3**, 430 (2019).

[2] R. Nelson, T. Wiesner-Hanks, R. Wisser, and P. Balint-Kurti, *Navigating complexity to breed disease-resistant crops,* Nature Reviews Genetics **19**, 21 (2018).

[3] M. Gou, P. Balint-Kurti, M. Xu, and Q. Yang, *Quantitative disease resistance: Multifaceted players in plant defense,* Journal of Integrative Plant Biology **65**, 594 (2023).

[4] J. A. Corwin and D. J. Kliebenstein, *Quantitative resistance: more than just perception of a pathogen,* The Plant Cell **29**, 655 (2017).

[5] J. de Wit, S. Tonn, G. Van den Ackerveken, and J. Kalkman, *Quantification of plant morphology and leaf thickness with optical coherence tomography,* Applied Optics **59**, 10304 (2020).

[6] P. Pieczywek, J. Cybulska, M. Szymańska-Chargot, A. Siedliska, A. Zdunek, A. Nosalewicz, P. Baranowski, and A. Kurenda, *Early detection of fungal infection of stored apple fruit with optical sensors–Comparison of biospeckle, hyperspectral imaging and chlorophyll fluorescence,* Food Control **85**, 327 (2018).

[7] F. E. O'Callaghan, R. A. Braga, R. Neilson, S. A. MacFarlane, and L. X. Dupuy, *New live screening of plant-nematode interactions in the rhizosphere,* Scientific Reports **8**, 1440 (2018).

[8] L. Srimal, U. Rajagopalan, and H. Kadono, *Functional optical coherence tomography (fOCT) biospeckle imaging to investigate response of plant leaves to ultra-short term exposure of ozone,* Journal of Physics: Conference Series **605**, 012013 (2015).

[9] D. Li, U. M. Rajagopalan, Y. S. K. De Silva, F. Liu, and H. Kadono, *Biospeckle optical coherence tomography (BOCT) in the speedy assessment of the responses of the seeds of Raphanus sativus l.(Kaiware Daikon) to acid mine drainage (AMD),* Applied Sciences **12**, 355 (2021).

[10] M. Münter, M. Vom Endt, M. Pieper, M. Casper, M. Ahrens, T. Kohlfaerber, R. Rahmanzadeh, P. König, G. Hüttmann, and H. Schulz-Hildebrandt, *Dynamic contrast in scanning microscopic OCT,* Optics Letters **45**, 4766 (2020).

[11] G. R. Littlejohn, J. C. Mansfield, J. T. Christmas, E. Witterick, M. D. Fricker, M. R. Grant, N. Smirnoff, R. M. Everson, J. Moger, and J. Love, *An update: improvements in imaging perfluorocarbon-mounted plant leaves with implications for studies of plant pathology, physiology, development and cell biology,* Frontiers in Plant Science **5**, 140 (2014).

[12] A. Oldenburg, P. Ji, X. Yu, and L. Yang, *Temporal non-uniform compressive sampling for dynamic optical coherence tomography,* Optica Open Preprint opticaopen.21983354.v1 (2023).

[13] J. Alle, R. Gruber, N. Wöhrlein, N. Uhlmann, J. Claußen, T. Wittenberg, and S. Gerth, *3D segmentation of plant root systems using spatial pyramid pooling and locally adaptive field-of-view inference,* Frontiers in Plant Science **14**, 1055 (2023).

[14] S. van Wees *et al.*, *Phenotypic analysis of Arabidopsis mutants: trypan blue stain for fungi, oomycetes, and dead plant cells,* Cold Spring Harbor Protocols [E] **3** (2008).

6

Conclusion and outlook

This chapter first concludes this thesis, summarizing the contributions of this thesis to OCT plant imaging and identifying the role that OCT can take in the field of plant imaging. Then it gives an outlook on promising research directions that can be derived from the work in this thesis. First an outlook on OCT plant imaging and prospects for further application is given, followed by an outlook on OCT resolution enhancement, which was the major topic of two thesis chapters.

6.1. Conclusions

The application of optical coherence tomography to plant imaging and phenotyping has been a clear guideline through the work in this thesis. Three issues have been addressed in this work: the limited OCT imaging depth in scattering plant tissue, the required high resolution to resolve important features inside the plant, and the limited specificity of OCT for plant imaging.

The limited OCT imaging depth in plant tissue, especially in leaves, could largely be attributed to the inter-cellular air spaces that play a role in the gas-exchange of leaves with the atmosphere. The large refractive index contrast between these air spaces and the surrounding tissue causes scattering, refraction, and wavefield aberrations, leading to a poor imaging depth. In chapter 2 of this work, we extended the OCT imaging depth by infiltrated the leaves with water or perfluorodecalin to reduce the refractive index contrast. This allowed to image entire leaf cross sections and quantify laterally resolved leaf thickness.

OCT resolution enhancement was shown in axial and lateral direction. Chapter 3 presented spectral estimation (SE) with the iterative adaptive approach (IAA) for OCT reconstruction with super-resolution. Our SE-OCT method gave, dependent on the SNR, a 2 to 10 times better resolution than conventional reconstructions, with a sub-second B-scan processing time. In chapter 4, SE-OCT was made compatible with computational refocusing based on the coherent OCT signal. This allowed the development of an OCT imaging setup with sub-micrometer lateral resolution over

a large depth range, and an axial resolution below 2 µm, while using a cost-effective narrowband SLD in the visible range. Key in this application was the translation of SE-OCT to an extrapolation of the interference signal in the k-domain using missing-data IAA so that it was compatible with ISAM inverse scattering and computational adaptive optics (CAO). The high 3D resolution enabled visualization of sub-cellular details for plant tissue.

As OCT imaging uses back-scattered light, it does not generate contrast between equally scattering structures. This lack of specificity is a major drawback for the use of OCT to plant imaging, especially when applied to imaging pathogens inside plants. In chapter 5, we addressed this lack of specificity using functional OCT imaging. Because downy mildew hyphae contain scattering structures that are constantly in motion, it gives a dynamic speckle pattern on the OCT images. This is used as contrast to distinguish between the pathogen and the less dynamic plant tissue. With this dynamic OCT (dOCT) we could visualize downy mildew in 3D and *in-vivo* while it was growing inside a lettuce leaf. Moreover, as dOCT is a label-free imaging method, no fluorescent labeling or staining was needed to generate this contrast. In our work, the origin of the dynamic contrast was analyzed, downy mildew hyphae were segmented to quantify differences in pathogen in-growth between plant genotypes, and longitudinal imaging of pathogen growth over several days was demonstrated. These results demonstrated that dynamic OCT is sufficiently specific to image pathogens inside plants with high contrast.

The proposed solutions to improving the imaging depth, resolution and specificity of OCT plant imaging require more sample preparation and lead to larger data sets and longer imaging times. This makes it challenging to apply OCT plant imaging to high-throughput plant phenotyping. However, compared to conventional microscopy, OCT has some significant advantages which have become clear in this thesis. OCT has the unique ability to image plant tissue *in-vivo* with a high resolution in 3D without labels.

The label-free imaging in uncleared tissue reduces the sample preparation time and effort compared to conventional microscopy, and allows for *in-vivo* imaging structures that are hard to label. Functional OCT imaging can give the required specific contrast. Imaging *in-vivo* allows for longitudinal studies and imaging plant processes that take place over time. The high 3D resolution allows for imaging structure and processes at cellular and even sub-cellular level, which reveals fundamental processes that cannot be directly imaged with macroscopic imaging sensors. Thus, though OCT is less suitable for high-throughput phenotyping, it is a promising tool for plant imaging and phenotyping at microscopic level. Complementing conventional microscopy techniques, it is likely to have a major impact in the field of plant science in understanding fundamental plant processes. Some potential areas of impact will be discussed in the next section.

6.2. Outlook on OCT plant imaging

Three promising directions of further study on the application of OCT in plant science can be identified. First, we discuss extending the application range of OCT imaging plant to roots. Second, we present and discuss the application of dOCT to

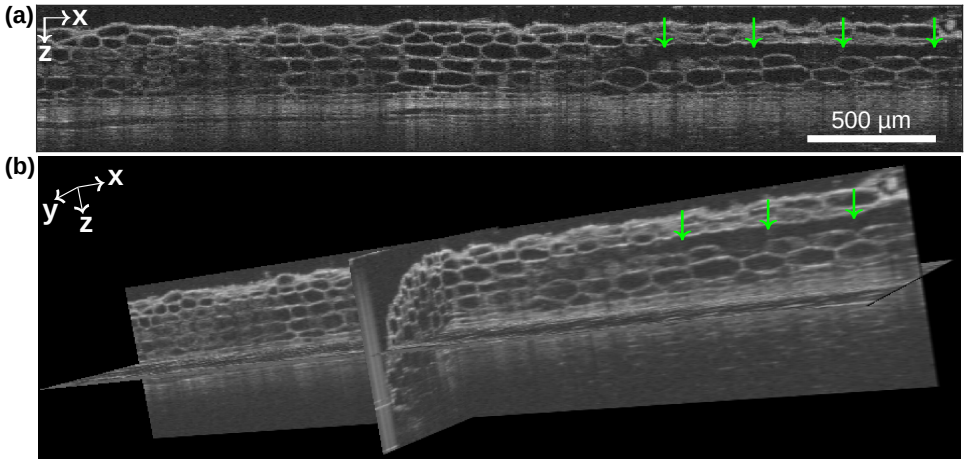

Figure 6.1: OCT image of a basil root with aerenchyma (green arrows). (a) B-scan along the root direction and (b) shows a 3D rendering of the volumetric OCT image of the root section.

other pathogens and processes. Third, other functional OCT imaging could have important applications in plant imaging.

6.2.1. Root imaging with OCT

Plant roots are an important part of plants as they take up water and nutrients. Because roots grow in optically impenetrable soil, root imaging and phenotyping is challenging. However, when growing them in water [1], on transparent substrates [2], in rhizotrons (against a transparent window) [3] or in transparent soil [4, 5], *in-vivo* OCT imaging of roots is possible. As roots do not have gas-exchange pockets like leaves, water infiltration is not needed and roots can be imaged up to large depths without further sample preparation.

Particularly of interest could be the investigation of morphological changes in roots due to cultivation in a hydrophonic system (roots growing in water) [6] or flooding [7]. For example, roots submersed in water form air channels (aerenchyma) to allow for oxygen flow to the roots [7]. This response to flooding stress is currently investigated using physical slicing of root tissue and subsequent imaging with brightfield microscopy [6]. Slicing is labour intensive and typically allows imaging at only a few slices. High resolution OCT cannot only do this faster and non-destructively, but also enables quantification of the 3D structure of aerenchyma and how they take shape over time. Figure 6.1 shows an example image of a root of a basil plant obtained with the Ganymede OCT system that was grown in water with a lack of oxygen. The green arrows indicate an aerenchyma caused by oxygen deficiency.

Using functional OCT imaging, it could be possible to visualize and quantify processes such as sap flow or organ initiation. Quantification of flow is a challenging task, which will be further elaborated on in section 6.2.3. Because of their small

cylindrical structure, plant roots would also be ideal samples to apply high resolution tomography, such as optical coherence refraction tomography [8]. This would enable 3D imaging of the internal root structure and reduce occlusion behind the vascular bundle and reduce speckle.

6.2.2. Dynamic OCT imaging of plants

Chapter 5 presented dOCT for the imaging of downy mildew in lettuce. As this was the first study on dynamic OCT plant imaging, there remain many questions and opportunities that need further research. First, the dOCT acquisition and data processing could be further optimized, to increase robustness and get more information out of the signal. Second, dOCT can be used for imaging other pathogens and plant processes.

Dynamic OCT optimization for plant imaging

Most information in the dOCT images originate from fluctuations with relatively low frequencies up to 8 Hz. Thus, the image repetition rate can be significantly reduced to around 15 to 20 Hz. Using a faster point-scanning OCT or a line-scan or full-field OCT setup [9] while reducing the image repetition rate makes it possible do dOCT on (sub) volume level, rather than B-scan level dOCT that is done in this thesis. This would allow for much faster volumetric imaging while still capturing slow fluctuations that require a long imaging time. Moreover, this would enable computational depth-of-field extension, as the phase information from fluctuating speckle will then be sufficiently correlated along the slow scan direction to do coherent post-processing.

For longer longitudinal studies, we sometimes observed that the intensity of the dynamic OCT signal of the *B. lactucae* hyphae decreases, especially after sporulation. A possible reason for this is that the hyphae die off once the pathogen has released its spores. It could be very interesting to see how pesticides, resistance-stimulating microbes, and varied plant immune responses influence the dynamic activity of the pathogen in the leaf. Thus, the dynamic signal can be used not only to create contrast between pathogen and plant tissue, but can also tell more about the vitality of the pathogen inside the leaf. This could yield very interesting and useful insights in pathogen resistance.

Because dOCT needs a time series for every tomographic scan, dOCT generates a lot of data. By smarter sampling in time based on compressed sensing techniques, dynamic signal at different time-scales could be captured with fewer data [10]. Optimizing the combination of different frequencies for the best contrast between pathogen and plant tissue is another important direction of further study. This is analogous to finding spectral indices in multi spectral imaging to measure for example vegetation cover or plant disease infection [11]. The data sampling could then be tailored to the combination that gives the best contrast. Lastly, deep learning (DL) methods enable easier recognition and segmentation of the pathogen in the plant. During live OCT B-scan imaging, it was often possible to recognize the *B. lactucae* within a shorter time frame than used for the dOCT image acquisition. Applying DL methods could simplify segmentation, reduce the required amount of

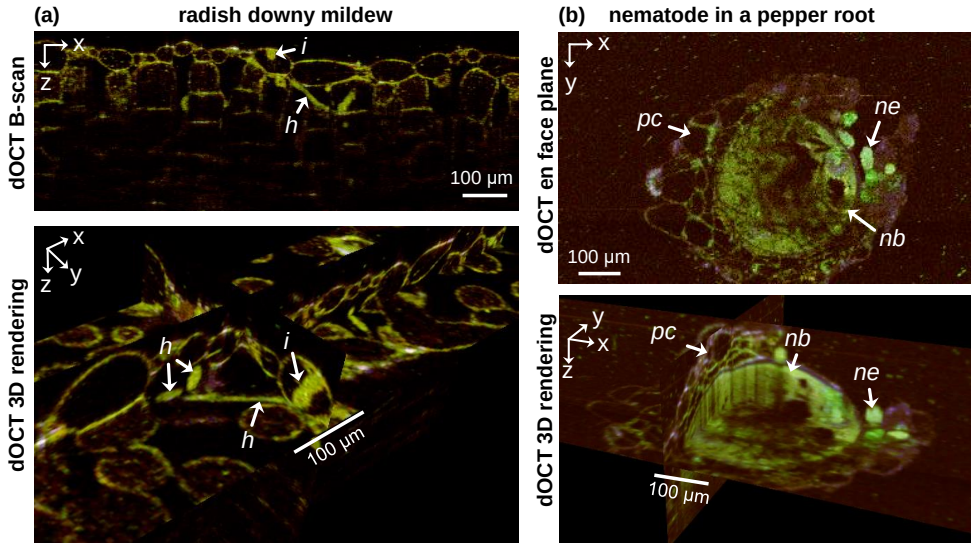

Figure 6.2: Dynamic OCT images of downy mildew a in radish leaf (a) and a root-knot nematode in a pepper root (b). *i*: infection; *h*: hyphae; *pc*: plant cell; *nb*: nematode body; *ne*: nematode egg

data for robust detection, and may even enable real time pathogen imaging.

The dynamic speckle signal that gives dOCT its contrast is also the source of contrast in many other functional OCT imaging methods. For example, biospeckle OCT [12], OCT correlation decay speed imaging [13], optical coherence angiography [14], and logarithmic intensity variance (LIV) [15] also measure the magnitude or time-scale of OCT signal amplitude fluctuations. A major difference within these methods is that some, like dynamic OCT, distinguishes the object of interest based on the time-scale of the fluctuations while others, like LIV only distinguish between static and dynamic. The contrast that is obtained with these various methods is often similar. It is useful to compare the differences between the methods and choose one that suits the application best.

Imaging other pathogens with dynamic OCT

Bremia lactucae infection in lettuce served as a model pathogen-plant system in Chapter 5. Thus, dOCT could also be applied to image other pathogens in plants. Figure 6.2 shows two examples: downy mildew in a radish leaf and a root-knot nematode (Meloidogyne incognita) in a pepper root.

Radish leaves have larger cells than lettuce leaves, resulting in a more open image where the mildew hyphae can clearly be distinguished, see Fig. 6.2(a). Also the place of infection (indicated with i) is clearly visible inside the large epidermal cell. The contrast in color between the cell walls and the hyphae is less strong than with *B. lactucae* in lettuce, but based on the structure the hyphae can be clearly distinguished by a trained eye or a neural network.

Once root-knot nematodes have entered the root and settled, their body becomes spherical and they put all their energy in producing eggs that stick together

in a gel. Root-knot nematodes and their eggs have a strong sub-cellular activity that causes a good contrast with dOCT between them and the plant root cells, as shown in Fig. 6.2(b). The OCT imaging depth is sufficient to see at least half of the body, including some internal structure, as well as the nematode eggs.

Bacterial infections are more challenging to image with dOCT as OCT does not have the resolution to resolve bacteria. For bacteria, dOCT may image the activity of a bacterial colony or the active immune response of the plant, which is less direct than imaging the pathogen itself. Still, the two examples in this section show that dOCT can be applied to visualize more types of plant pathogens than those presented in chapter 5.

6.2.3. Other functional OCT plant imaging

Besides dynamic OCT and biospeckle OCT [12], there are other functional OCT imaging methods that can be applied to obtain functional information from plants. Two promising methods, flow measurement and spectroscopic OCT, will be discussed below.

Flow measurement with OCT

Plants transport nutrients and water between the different organs through vascular bundles in leaf veins, stems and roots. The vascular bundles contain the xylem and the phloem [16]. The xylem transports water and minerals from the roots to the other plant organs, usually in a single direction. The phloem transports nutrients such as sugar and amino acids between the leaves, where photosynthesis takes place, to storage organs and places of plant growth. This flow is bi-directional and more complex.

Quantification of these flow processes yields more insight into the interplay of different plant organs and the plant's responses to various types of stress. It could be especially valuable to study, validate, and improve plant models [17].

OCT can measure flow velocities using Doppler [18] or dynamic light scattering (DLS) [19]. A challenge of measuring xylem flow could be the limited scattering in water with dissolved minerals. Without scattering particles in the flow, there will be no signal to quantify the flow. If the minerals and the surrounding complex do not provide sufficient light scattering, it may be possible to add scattering contrast agents, such as nano-particles, in the fluid to obtain sufficient scattering signal.

The phloem consist of living cells with sieve-like cell walls along the channel direction and microtubules to actively facilitate selective transport of nutrients to the place where they are needed [16]. Because of this simultaneous but selective transport of different molecules within the flow cell, normal Doppler or DLS-OCT cannot be applied as that only works well for bulk motion. However, with DLS-OCT in combination with a good model of the underlying biology it may be feasible to probe the cell activity and determine the amount of (bi-directional) transport that is taking place.

Spectroscopic OCT

Multi-spectral and hyper-spectral imaging is widely applied in plant imaging and phenotyping [20–22]. The spectral dependency of light scattering relates to the

chemical composition of the plant tissue, which changes due to biotic and abiotic stress. Spectroscopic OCT could obtain this functional contrast within the plant tissue at micrometer scale resolution in 3D [23]. With the large bandwidth of a supercontinuum (SC) laser, spectral contrast can be obtained over a large spectral range including the visible light [24]. Due to the inverse relationship between the axial resolution and the source bandwidth, spectroscopic analysis of the spectrum reduces the OCT axial resolution as the source width is divided into smaller spectral windows.

For plant imaging and phenotyping, spectroscopic OCT can be used to study plant processes at microscopic resolution. It can also be used to understand or to identify the origin of the spectral contrast in macroscopic spectral imaging, which can then be used for the high-throughput phenotyping.

6.3. Outlook on computational OCT resolution enhancement

Chapter 3 and 4 of this thesis focused on computational resolution enhancement. Though applicable to OCT plant imaging, it has a much wider scope of applications. First we discuss two extensions of spectral estimation OCT (SE-OCT): phase-sensitive SE-OCT and lateral spectral estimation. Then it discusses the relevant question how SE-OCT relates to resolution improvement using deep learning (DL) methods. Finally, it discusses some ideas to improve the robustness of computational adaptive optics.

6.3.1. Reducing phase leakage in phase-sensitive OCT

Phase sensitive OCT is a powerful method to measure motion with nanometer precision. For example, OCT based vibrometry uses the phase information to quantify the amplitude and frequency of vibrations of, for example, the organ of Corti in the ear [25, 26]. When measuring the vibration of closely separated interfaces, phase leakage may occur between the interfaces, leading to systematic errors [27–29]. This phase leakage, sometimes called signal competition, is especially strong when a low intensity interface is in the vicinity of an interface with a higher intensity.

IAA-based SE-OCT can preserve the phase information in the OCT image, as was shown in Chapter 4. Since the weighting matrix in IAA suppresses the signal from interfaces other than the reconstruction depth, it could also suppress the phase leakage from a (high intensity) interface in the vicinity. To confirm this effect, a short simulation study was performed using the 1D OCT simulation framework discussed in Chapter 3.

Figure 6.3 shows the results of a simulation study on phase leakage reduction with RFIAA. Interfaces 1 and 2 have an SNR of 36 dB and vibrate with 1.2 kHz and amplitude of 20 nm. Interface 3 has 100 times the reflection intensity of interfaces 1 and 2, and thus has a higher SNR of 56 dB. It is located 3.0 µm below interface 2, while it vibrates with a frequency of 0.25 kHz and amplitude of 80 nm. As interfaces 2 and 3 are separated with a distance that is close to the full-bandwidth DFT (FBW-DFT) and that is smaller than the partial bandwidth DFT (PBW-DFT)

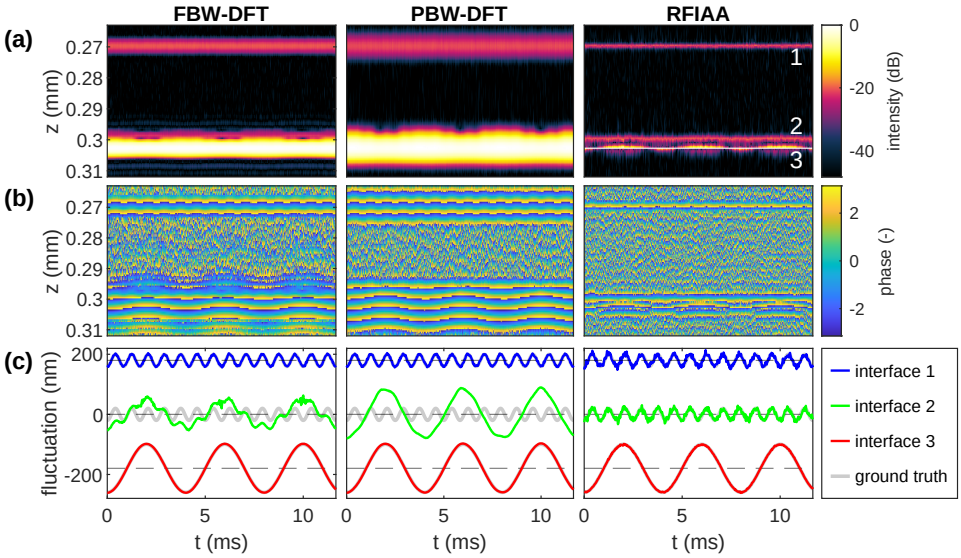

Figure 6.3: Results for a simulation of phase leakage reduction by IAA-based SE-OCT. (a) M-scan intensity, (b) the phase of the M-scan, and (c) the reconstructed displacement of the three simulated interfaces.

6

axial resolution, the phase from interface 3 leaks heavily into interface 2 as seen in (b) and (c). It is also clear that the phase of the the second interface does not resolve the high frequency oscillation, but instead shows the low frequency of the third interface. RFIAA uses only the PBW-DFT bandwidth, and is able to resolve the interfaces in the M-scan (a). Moreover, it faithfully reconstructs the vibration amplitude and frequency of the second interface (c).

The phase reconstruction of interface 1 with RFIAA in (c) is a bit more noisy than the DFT methods. However, the accuracy is sufficient to obtain the amplitude and phase of the vibration and the same accuracy is maintained for interface 2. These results show that RFIAA could be a valuable addition for OCT-based vibrometry. This is especially the case when the axial resolution is compromised with a relatively small bandwidth swept source to obtain the large axial range that is needed for imaging the ear [30]. Moreover, RFIAA could also be useful for other phase sensitive OCT applications (including Doppler OCT) where phase leakage could result in biased reconstructions.

6.3.2. Spectral estimation OCT in multiple dimensions

Potentially, the results from axial spectral estimation (SE) could be extended to the lateral direction to obtain lateral super-resolution. This would be an equivalent to its application on 2D radar imaging [31]. We explored this application and present some preliminary results in this section.

Lateral SE to obtain super resolution can be performed in an equivalent way to the axial SE-OCT as discussed in Chapter 3, but then as a 2D SE problem. The

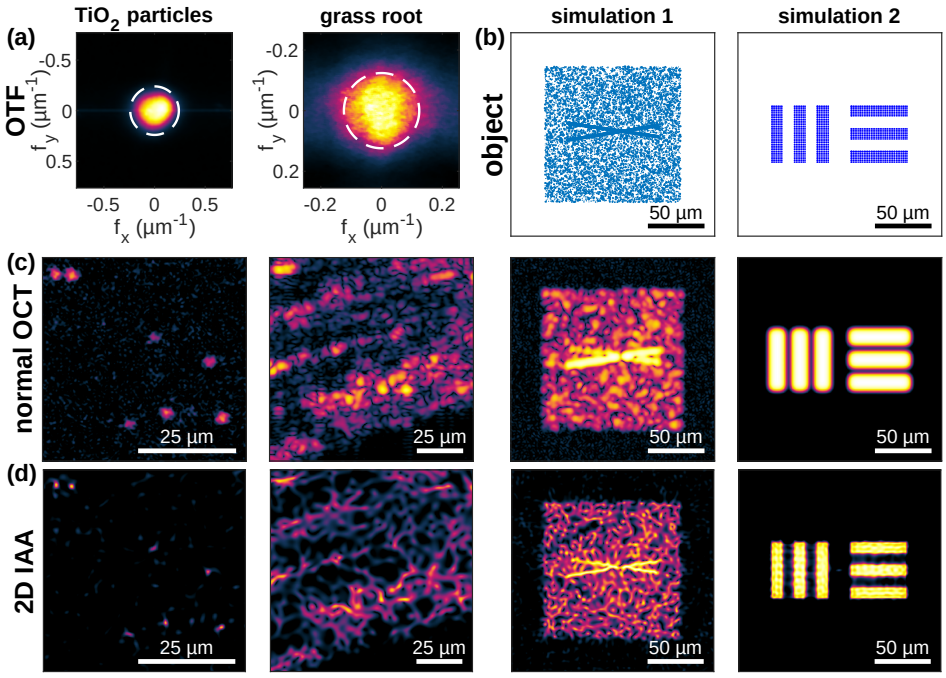

Figure 6.4: Results for lateral SE-OCT with 2D IAA. (a) Estimated OTFs for the experimental samples, with the input area for 2D IAA indicated by the white dashed circles. (b) Simulated objects, consisting of many point scatterers. (c) Normal OCT en face images and (d) the same area estimated with 2D IAA based on a circular input aperture.

equivalent to the interference spectrum is the field in the pupil plane (i.e. the lateral Fourier transform of the complex en face image), which can be uniformly reshaped by the equivalent of the reference spectrum, the optical transfer function (OTF).

Implementation of 2D SE-OCT

There are a few significant differences between the axial SE-OCT and its equivalent in the lateral direction. First, in the axial direction the interference signal is measured in the k-space and transferred to the depth domain in OCT processing, while in the lateral direction the image information is obtained in the spatial domain by physically scanning the beam. Axial SE-OCT avoided some inherent disadvantages of the DFT, but for lateral SE-OCT a DFT needs to be applied to obtain the field in the pupil plane on which the spectral estimation has to be performed. Second, the 2D dimensionality of lateral SE creates the problem of rapidly enlarged datasets and weighting matrices with increasing image size. Moreover, as the OTF in general has a radial symmetry, the high SNR input spectrum for SE is preferably circularly shaped, which is incompatible with the fastest IAA implementations. Choosing a rectangular input spectrum creates low SNR corners, while neglecting some high SNR data at the edges. Third, accurately estimating the OTF can be challenging as the OTF cannot easily be measured by a reference measurement, in contrast to the

reference supplied by the reference arm intensity in 1D SE-OCT.

In a recent work on resolution-enhanced OCT (RE-OCT), the OTF was estimated using an axial average of the absolute value of the pupil field of a stack of en face images [32]. This OTF was then used to computationally broaden the field in the pupil plane, yielding a factor 1.5 lateral resolution improvement. Estimating the OTF in this way requires, however, that the object has a relatively flat lateral frequency spectrum. Another option is calibrating the OTF with a reference measurement on small point particles, but as the shape of the OTF can change due to, for example, a tilted front interface or sample-induced aberrations, this method is less reliable. Obtaining the OTF from a small image feature, used as guide-star, could be another option, but that requires (manual) selection of such a guide-star.

2D spectral estimation results

Figure 6.4 shows results for 2D SE with IAA on an en face OCT image. The first two columns (TiO_2 particles in gelatine and the root of a grass plant) are based on experimental data, while the last two columns are based on simulations. The OTF for the experimental data was estimated by taking the average of the absolute value of the pupil plane field of a stack of en face images, similar as done with RE-OCT [32], and then smoothing the average with a 2D Gaussian kernel. This is analogous to laterally averaging the interference spectral signal to estimate the source spectrum in axial OCT reconstruction. Figure 6.4(a) shows the resulting OTFs, with the white dashed circle indicating the area that is used for 2D IAA, with radii of 40 and 62 pixels. 2D IAA gives a clear resolution improvement for the TiO_2 particles sample, visible in the much smaller dots in (d) compared to (c). However, a close look at the points show that they their shape is not isotropic and contain some tail-like side lobes.

When looking at the medium sparse grass root sample, we see that the speckle signal that makes up the cell walls is reconstructed by 2D IAA as a net-like structure with narrow lines. As this is not the expected microscopic structure of a plant root, it likely is an artefact that 2D IAA creates from the speckle signal to increase its sparsity.

To confirm this, the 3D OCT signal was simulated of two crossing lines in a volume with many sub-resolution scatterers with Gaussian-distributed reflectivity (simulation 1). The used 3D simulation framework is described in chapter 4. Figure 6.4(b) shows the simulated object. While the normal OCT image shows a speckle pattern as can be seen in conventional OCT images, the 2D IAA image shows again a net-like structure formed by narrow lines. The crossing lines in (d) are better resolved than in (c), showing the improved resolution. However, as the background also seems to contain a lot of structure, which does not resemble the true object, the structure in the grass root image is probably also not resembling the sample itself. This makes it problematic to apply 2D IAA in any object that contains significant speckle.

In simulation 2, a resolution target element is made up of 48000 point scatterers with a spacing far below the resolution limit. The normal OCT image shows the slightly blurred lines, which are still clearly distinguishable. 2D IAA images the

elements with much sharper boundaries, resembling the true structure of the object. However, a close look at the elements reveals a pattern of varying intensity on the lines. This effect was also seen, in a more severe way, with experimental data from a resolution target. Thus for smooth reflecting surfaces with laterally constant reflectivity, 2D IAA also creates structure that does not resemble the true object.

Because of the fast increasing input data size in 2D, we limited the spectral estimation input to a radius of 40 to 62 pixels, giving 5025 to 12061 input points, and computation times of 64 s to 699 s respectively on a Dell Precision 5820 with an Intel Xeon W-2223 CPU and 32 GB RAM. Further increasing the input data size will result in a memory overflow and huge computation times. To include higher spatial frequency information as input of the spectral estimation, without increasing the input data size, the en face image can be cropped, or processed per smaller patch.

Discussion on 2D spectral estimation

Based on the results from measurements and simulations, we conclude that lateral SE-OCT using 2D IAA does not give reliable imaging results. For a laterally very sparse object with high contrast, i.e., the lines in simulation 1, 2D IAA could improve the lateral resolution and resolve small structures. However, these situations are scarce and the danger of misinterpreting artefacts for structure would, in most cases, far outweigh the potential resolution improvement.

A potential improvement to lateral 2D IAA would be to measure the object spectrum directly in the pupil plane, using a full-field OCT setup. This could eliminate potential problems arising from the DFT that is used to obtain the field in the pupil plane. However, it is unlikely that this will solve the problem of erroneous reconstructed structures from speckle signal.

A relevant question would be whether SE-OCT in the axial direction could have the same problem of producing non-existing structures from speckle signal. Autoregressive spectral estimation, in fact, produced some erroneous peaks [33]. Here it is good to realize that speckle itself is not the true sample structure, but the coherent addition of signals from structures that are too small to be resolved. The problem in lateral SE-OCT is that the energy is redistributed in 2D in a way that does not look like speckle, but rather like object structure, and is therefore easily misinterpreted. As the axial speckle size in OCT is determined by the axial resolution, SE-OCT images this as narrower peaks. Since, the OCT amplitude is still Rayleigh distributed, this signal could be interpreted in the same way as normal OCT images. Thus, our work on axial SE-OCT is still reliable.

6.3.3. Relationship between deep learning and SE-OCT

Deep learning (DL) methods such as convolutional neural networks (CNN) and generative adversarial networks (GAN) have become an important tool in science for data processing and analysis. Also in optical coherence tomography they have been used for segmentation, denoising [34], reconstruction of undersampled data [35, 36] and obtaining super-resolution [34, 37]. A natural question to ask here is how the used SE techniques relate to DL methods.

SE and DL for OCT reconstruction are similar in that they use prior knowledge to obtain good images with less available data. However, there are also significant differences. While IAA-based SE-OCT assumes moderate sparsity in the OCT image as prior knowledge, DL obtains the prior information through training of a neural network. The prior information with SE-OCT is thus more explicitly included in the (non-parametric) model. It does not require training data, and potential errors in the reconstruction are easier to recognize based on the knowledge of the method. With DL methods the relationship between input and output is less easy to interpret. Moreover, it needs high quality training data from relevant samples with sufficient diversity to faithfully reconstruct samples that deviate from the average sample. Though our SE-OCT algorithm is faster than comparable methods in literature, and could be made faster with GPU implementation, DL-based reconstruction with a well-trained network is likely to be faster than SE-OCT. Moreover, as DL methods do not explicitly use a model, it could combine axial resolution improvement with refocusing, lateral resolution improvement, denoising [34] and even segmentation without the need to model that. Currently, SE-OCT gives a larger resolution improvement than DL-based super-resolution methods [34], but that can change when DL methods become more sophisticated.

SE and DL methods are not only alternatives, they can also complement each other. SE-OCT can deliver high resolution training data for a DL network, such that no expensive hardware is needed for training. DL methods can also be used to improve SE-OCT images, for example by denoising non-sparse image areas, segmenting structures of interest or improving lateral resolution. Moreover, DL methods can be used for real time image reconstruction with enhanced resolution, after which the SE-OCT with higher axial resolution can be applied to a single recorded volume. Thus, even though DL methods become better at OCT image reconstruction and processing, our work on SE-OCT is still a relevant and useful for complementing DL methods.

6.3.4. Robustness of computational adaptive optics

In chapter 4 we implemented computational adaptive optics (CAO), where we estimated the aberrations using the sub-aperture cross-correlation method. For samples with a lot of speckle, this method is not very robust because the speckle pattern is independent for non-overlapping sub-apertures. Correlating independent speckle patterns may lead to a wrong estimation of the aberrations. Correlating each sub-aperture with multiple randomly chosen sub-apertures instead of the center aperture improves the robustness [38]. With multiple sub-apertures, the phase error is over-determined and a least squares (LS) fitting can be performed. In chapter 4, we further increased the robustness by taking the axial moving average of the Zernike coefficients in axial direction. Using the inverse of the LS error, the influence of less accurate estimations was reduced, while a Gaussian kernel ensured smoothness over a small axial range.

This concept could be extended with other ways of regularizing the estimated aberration coefficients. For example, a more optimal relationship between weight and LS fitting error could be used, and estimations that are completely unreliable

could be excluded. Also the accuracy of the correlation itself could be taken into account with the LS fitting. If the peak in the correlation between sub-aperture images is broad, the determined shift is less accurate than with a sharp peak. Weighting these effects and propagating them in the estimation of the aberrations may improve its robustness and enhance the accuracy.

References

[1] H. Massalha, E. Korenblum, S. Malitsky, O. H. Shapiro, and A. Aharoni, *Live imaging of root–bacteria interactions in a microfluidics setup,* Proceedings of the National Academy of Sciences **114**, 4549 (2017).

[2] K. A. Nagel, H. Lenz, B. Kastenholz, F. Gilmer, A. Averesch, A. Putz, K. Heinz, A. Fischbach, H. Scharr, F. Fiorani, *et al.*, *The platform GrowScreen-Agar enables identification of phenotypic diversity in root and shoot growth traits of agar grown plants,* Plant Methods **16**, 1 (2020).

[3] M. O. Yee, P. Kim, Y. Li, A. K. Singh, T. R. Northen, and R. Chakraborty, *Specialized plant growth chamber designs to study complex rhizosphere interactions,* Frontiers in Microbiology **12**, 507 (2021).

[4] H. Downie, N. Holden, W. Otten, A. J. Spiers, T. A. Valentine, and L. X. Dupuy, *Transparent soil for imaging the rhizosphere,* PLOS ONE **7**, 1 (2012).

[5] L. Ma, Y. Shi, O. Siemianowski, B. Yuan, T. K. Egner, S. V. Mirnezami, K. R. Lind, B. Ganapathysubramanian, V. Venditti, and L. Cademartiri, *Hydrogel-based transparent soils for root phenotyping in vivo,* Proceedings of the National Academy of Sciences **116**, 11063 (2019).

[6] M. Tuylu *et al.*, *Examination of anatomical features of tomato (Lycopersicon esculentum Mill.) varieties cultivated under hydroponic system,* Applied Ecology and Environmental Research **16**, 3381 (2018).

[7] M. L. Vidoz, F. Mignolli, H. T. Aispuru, and L. A. Mroginski, *Rapid formation of adventitious roots and partial ethylene sensitivity result in faster adaptation to flooding in the aerial roots (aer) mutant of tomato,* Scientia Horticulturae **201**, 130 (2016).

[8] K. C. Zhou, R. Qian, S. Degan, S. Farsiu, and J. A. Izatt, *Optical coherence refraction tomography,* Nature Photonics **13**, 794 (2019).

[9] L. Ginner, A. Kumar, D. Fechtig, L. M. Wurster, M. Salas, M. Pircher, and R. A. Leitgeb, *Noniterative digital aberration correction for cellular resolution retinal optical coherence tomography in vivo,* Optica **4**, 924 (2017).

[10] A. Oldenburg, P. Ji, X. Yu, and L. Yang, *Temporal non-uniform compressive sampling for dynamic optical coherence tomography,* Optica Open Preprint opticaopen.21983354.v1 (2023).

[11] A.-K. Mahlein, T. Rumpf, P. Welke, H.-W. Dehne, L. Plümer, U. Steiner, and E.-C. Oerke, *Development of spectral indices for detecting and identifying plant diseases,* Remote Sensing of Environment **128**, 21 (2013).

[12] L. Srimal, H. Kadono, and U. Rajagopalan, *Optical coherence tomography biospeckle imaging for fast monitoring varying surface responses of a plant leaf under ozone stress,* in *Sensing Technologies for Biomaterial, Food, and Agriculture 2013*, Vol. 8881 (SPIE, 2013) pp. 96–101.

[13] I. Abd El-Sadek, A. Miyazawa, L. T.-W. Shen, S. Makita, S. Fukuda, T. Yamashita, Y. Oka, P. Mukherjee, S. Matsusaka, T. Oshika, *et al.*, *Optical coherence tomography-based tissue dynamics imaging for longitudinal and drug response evaluation of tumor spheroids,* Biomedical Optics Express **11**, 6231 (2020).

[14] R. F. Spaide, J. G. Fujimoto, N. K. Waheed, S. R. Sadda, and G. Staurenghi, *Optical coherence tomography angiography,* Progress in Retinal and Eye Research **64**, 1 (2018).

[15] S. Kojima, P. Mukherjee, I. Abd El-Sadek, S. Makita, Y. Yasuno, and Y. Lim, *Dynamics imaging of plant maturity by optical coherence tomography,* in *Optical Coherence Tomography* (Optica Publishing Group, 2022) pp. CTu2E–3.

[16] R. Crang, S. Lyons-Sobaski, and R. Wise, *Plant anatomy: a concept-based approach to the structure of seed plants* (Springer, 2018).

[17] F. C. Pascut, V. Couvreur, D. Dietrich, N. Leftley, G. Reyt, Y. Boursiac, M. Calvo-Polanco, I. Casimiro, C. Maurel, D. E. Salt, *et al.*, *Non-invasive hydrodynamic imaging in plant roots at cellular resolution,* Nature Communications **12**, 4682 (2021).

[18] R. A. Leitgeb, R. M. Werkmeister, C. Blatter, and L. Schmetterer, *Doppler optical coherence tomography,* Progress in Retinal and Eye Research **41**, 26 (2014).

[19] N. Weiss, T. G. van Leeuwen, and J. Kalkman, *Localized measurement of longitudinal and transverse flow velocities in colloidal suspensions using optical coherence tomography,* Physical Review E **88**, 042312 (2013).

[20] A.-K. Mahlein, M. T. Kuska, J. Behmann, G. Polder, and A. Walter, *Hyperspectral sensors and imaging technologies in phytopathology: state of the art,* Annual Review of Phytopathology **56**, 535 (2018).

[21] B. Lu, P. D. Dao, J. Liu, Y. He, and J. Shang, *Recent advances of hyperspectral imaging technology and applications in agriculture,* Remote Sensing **12**, 2659 (2020).

[22] R. Sarić, V. D. Nguyen, T. Burge, O. Berkowitz, M. Trtílek, J. Whelan, M. G. Lewsey, and E. Čustović, *Applications of hyperspectral imaging in plant phenotyping,* Trends in Plant Science **27**, 301 (2022).

[23] A. L. Oldenburg, C. Xu, and S. A. Boppart, *Spectroscopic optical coherence tomography and microscopy,* IEEE Journal of Selected Topics in Quantum Electronics **13**, 1629 (2007).

[24] A. Lichtenegger, D. J. Harper, M. Augustin, P. Eugui, M. Muck, J. Gesperger, C. K. Hitzenberger, A. Woehrer, and B. Baumann, *Spectroscopic imaging with spectral domain visible light optical coherence microscopy in Alzheimer's disease brain samples,* Biomedical Optics Express **8**, 4007 (2017).

[25] E. S. Olson and C. E. Strimbu, *Cochlear mechanics: New insights from vibrometry and optical coherence tomography,* Current Opinion in Physiology **18**, 56 (2020).

[26] S. S. Gao, P. D. Raphael, R. Wang, J. Park, A. Xia, B. E. Applegate, and J. S. Oghalai, *In vivo vibrometry inside the apex of the mouse cochlea using spectral domain optical coherence tomography,* Biomedical Optics Express **4**, 230 (2013).

[27] A. K. Ellerbee and J. A. Izatt, *Phase retrieval in low-coherence interferometric microscopy,* Optics Letters **32**, 388 (2007).

[28] N. C. Lin, C. P. Hendon, and E. S. Olson, *Signal competition in optical coherence tomography and its relevance for cochlear vibrometry,* The Journal of the Acoustical Society of America **141**, 395 (2017).

[29] Y. Ling, M. Wang, X. Yao, Y. Gan, L. Schmetterer, C. Zhou, and Y. Su, *Effect of spectral leakage on the image formation of Fourier-domain optical coherence tomography,* Optics Letters **45**, 6394 (2020).

[30] D. MacDougall, J. Farrell, J. Brown, M. Bance, and R. Adamson, *Long-range, wide-field swept-source optical coherence tomography with GPU accelerated digital lock-in Doppler vibrography for real-time, in vivo middle ear diagnostics,* Biomedical Optics Express **7**, 4621 (2016).

[31] G.-O. Glentis and A. Jakobsson, *Efficient implementation of iterative adaptive approach spectral estimation techniques,* IEEE Transactions on Signal Processing **59**, 4154 (2011).

[32] N. Leartprapun and S. G. Adie, *Resolution-enhanced OCT and expanded framework of information capacity and resolution in coherent imaging,* Scientific Reports **11**, 20541 (2021).

[33] X. Liu, S. Chen, D. Cui, X. Yu, and L. Liu, *Spectral estimation optical coherence tomography for axial super-resolution,* Optics Express **23**, 26521 (2015).

[34] Y. Huang, Z. Lu, Z. Shao, M. Ran, J. Zhou, L. Fang, and Y. Zhang, *Simultaneous denoising and super-resolution of optical coherence tomography images based on generative adversarial network,* Optics Express **27**, 12289 (2019).

[35] Y. Zhang, T. Liu, M. Singh, E. Çetintaş, Y. Luo, Y. Rivenson, K. V. Larin, and A. Ozcan, *Neural network-based image reconstruction in swept-source optical coherence tomography using undersampled spectral data,* Light, Science & Applications **10**, 155 (2021).

[36] A. Lichtenegger, M. Salas, A. Sing, M. Duelk, R. Licandro, J. Gesperger, B. Baumann, W. Drexler, and R. A. Leitgeb, *Reconstruction of visible light optical coherence tomography images retrieved from discontinuous spectral data using a conditional generative adversarial network,* Biomedical Optics Express **12**, 6780 (2021).

[37] S. Cao, X. Yao, N. Koirala, B. Brott, S. Litovsky, Y. Ling, and Y. Gan, *Super-resolution technology to simultaneously improve optical & digital resolution of optical coherence tomography via deep learning,* in *2020 42nd Annual International Conference of the IEEE Engineering in Medicine & Biology Society (EMBC)* (IEEE, 2020) pp. 1879–1882.

[38] D. Hillmann, C. Pfäffle, H. Spahr, S. Burhan, L. Kutzner, F. Hilge, and G. Hüttmann, *Computational adaptive optics for optical coherence tomography using multiple randomized subaperture correlations,* Optics Letters **44**, 3905 (2019).

Acknowledgements

My PhD research would not have been possible without the presence of many colleagues, family, and friends during this beautiful but sometimes also challenging time. Maybe more important than the exact topic of the research are the people with whom I got to share my work and live within the past four years. Here I would like to extend my gratitude to you all.

First I would like to thank my supervisor Jeroen. You gave me a lot of confidence and freedom to find my way and choose my research direction, but you were also always available to discuss new findings or give feedback when needed. I thoroughly enjoyed the good discussions about our field and new ideas, and also the shared love for education. I am deeply grateful for your guidance and support as my colleague, friend, and supervisor. Sjoerd, your involvement was more in the background, but still very much appreciated, especially your care for my mental well-being with reminders to regularly go for a bike ride.

I would also like to thank my colleagues and collaborators in the Pathoview project. Sebastian, working with you together on this interdisciplinary project has been a great joy and we have learned a lot from each other's field and had a lot of fun together. The same is true for Ray, who joined later and enhanced the team spirit and collaboration in the join effort projects of UV fluorescence and OCT plant imaging. Also, Guido, your enthusiasm and ideas have been very stimulating for me. Whenever I came to Utrecht and you were there, you took some time to ask how it was going and encouraged me.

Peter-Paul, Adriaan, Frans, Daniël en Tonny from Rijk Zwaan, thank you for your enthusiasm, feedback, and resources. The discussions with you were very motivating and enjoyable.

George Glentis, your contribution to the fast implementation of the spectral estimation methods has led to two chapters that have also been published. Thank you for your hard work, your patience in explaining the theory, and your positive attitude. Here I also want to remember Kostas, who was involved with our first publication, but sadly passed away at the beginning of 2023, a shock for us and more so for his family and close colleagues.

Also my colleagues and office mates have been very important for me during my PhD period. Leon, studying together during the bachelor and master was a great joy for me, and I was very happy that the last half year of your PhD overlapped with my first year. You have given me a strong encouragement when I was dealing with the reverse culture shock and the uncertainties of a pioneering PhD project. Thank you for the great support you have been to me.

Qingru, I have sincerely enjoyed sharing the office with you as a colleague and friend. Thank you for your openness and the good conversations ranging from personal talks to sharing the frustrations and successes of our research. Yan, sharing

the office with you was a great joy as well, with your early schedule there was always someone waiting to welcome me in the office.

My fellow PhD students and postdocs Martijn, Peter, Kote, Huangcheng, Alim, Wenxiu, Christian, Jos, Gyllion, Sobhan, Isabel, Leo, and Ali, thank you all for the great lunches, discussions, and good moments we shared. You helped to create an environment where I felt at home and happy. Jelle, you left already when I started, but the few calls and documentation that you shared with me have helped me a lot to get started with the experimental work.

Annelies en Angela, you were always quick to help with many practical things, but also in for a good talk and interested in our overall well-being. Thank you for that! Also, Ronald, thank you for the support on the ICT side and the positive humor you bring to our group. Ron, thank you for all the custom mounts, your energy to think of the best mechanical solution, and the good discussions. Bernd, Mirjam, Nicolette, and Karin, thanks for the good feedback and the good conversations in the corridor and at the coffee table. Also, those whose names I may have forgotten to mention, but who were part of my life at university I would like to say thank you, not the least the cleaners who provided a clean building and office to work in.

I want to thank so many friends from outside the university who have supported me in my PhD journey. Especially from my life group from church who have been a great support to me during the sometimes challenging PhD period. I cannot mention you all by name, but you have been very important to me.

I am also grateful for the unconditional love and support from my family. Pa en ma, I feel truly blessed to have you as my parents and thank you for the support during the challenging times and shared joy in the times of success. My sisters and brothers Geertje, Martin, Nimrod, Elvira, and Jared, thank you for your interest and encouragement.

My dear Summer, thank you for the support you have been as my wife and soul mate. For you, my PhD period was also a challenging time: moving abroad, studying for a master degree, searching for a job, and dealing with the challenges of an intercultural relationship. Coming from a different background, it was a search for you to find the best way to support me. But with your great love and commitment, you learned quickly and I am so blessed by your love and support. Especially in the last stage of my PhD and of finishing my thesis you have encouraged me to go for it and supported me when I was exhausted by the hard work. I feel so grateful that you have become my dear wife and I look forward to our future ahead.

Last and above all, I want to thank God the creator of the beautiful nature of plants and optics, who gave me the capacity to pursue my PhD degree, and who as a father supported me through the whole process. To Him be the glory!

Curriculum Vitæ

Johannes DE WIT

26-02-1992 Born in Woerden, The Netherlands.

Education

2009-2013 Bachelor of Science in Applied Physics
Delft University of Technology

2013-2016 Master of Science in Applied Physics
Delft University of Technology
Thesis: Sequential beamforming for phased array imaging using stolt migration
Supervisors: dr. M.D. Verweij and Prof. dr. N. de Jong

2019-2023 Ph.D. Applied Physics
Delft University of Technology
Thesis: Microscopic 3D plant imaging with high-resolution optical coherence tomography
Promotors: dr. J. Kalkman and Prof. dr. S. Stallinga

List of Publications

Peer reviewed publications

6. **Jos de Wit**, Sebastian Tonn, Mon-Ray Shao, Guido Van den Ackerveken, and Jeroen Kalkman, *In-vivo label-free 3D OCT imaging of downy mildew in plant leaves*, manuscript in preparation.

5. **Jos de Wit**, George-Othon Glentis, and Jeroen Kalkman, *Computational 3D resolution enhancement for optical coherence tomography with a narrowband visible light source*, Biomedical Optics Express 14, 3532-3554 (2023) doi: 10.1364/BOE.487345.

4. Florian Tanner, Sebastian Tonn, **Jos de Wit**, Guido Van den Ackerveken, Bettina Berger, and Darren Plett. *Sensor-based phenotyping of above-ground plant-pathogen interactions*, Plant Methods 18.1, 35 (2022) doi: 10.1186/s13007-022-00853-7.

3. **Jos de Wit**, Kostas Angelopoulos, Jeroen Kalkman, and George-Othon Glentis, *Fast and accurate spectral-estimation axial super-resolution optical coherence tomography*, Optics Express 29, 39946-39966 (2021) doi: 10.1364/OE.439761.

2. **Jos de Wit**, Sebastian Tonn, Guido Van den Ackerveken, and Jeroen Kalkman, *Quantification of plant morphology and leaf thickness with optical coherence tomography*, Applied Optics 59, 10304-10311 (2020) doi: 10.1364/AO.408384.

1. Fabian Fool, **Jos de Wit**, Hendrik J. Vos, Deep Bera, Nico de Jong and Martin D. Verweij, *Two-Stage Beamforming for Phased Array Imaging Using the Fast Hankel Transform*, IEEE Transactions on Ultrasonics, Ferroelectrics, and Frequency Control, vol. 66, no. 2, pp. 297-308, Feb. 2019, doi: 10.1109/TUFFC.2018.2885870.

Conference contributions

4. **Jos de Wit**, Mon-Ray Shao, Sebastian Tonn, Guido Van den Ackerveken, and Jeroen Kalkman. Poster presentation: *Non-invasive microscopic 3D imaging of internal plant morphology with optical coherence tomography* at International Plant Phenotyping Symposium, September 2022, (Wageningen, NL).

3. **Jos de Wit**, Kostas Angelopoulos, Jeroen Kalkman, and George-Othon Glentis. Oral presentation: *Spectral estimation optical coherence tomography for retinal imaging*, at Biophotonics Congress: Biomedical Optics 2022, (Fort Lauderdale, Florida, USA), paper CW1E.5.

2. **Jos de Wit**, Kostas Angelopoulos, Jeroen Kalkman, and George-Othon Glentis. Oral presentation: *Axial super-resolution for optical coherence tomography with the iterative adaptive approach*, at OSA Imaging and Applied Optics Congress 2021 (COSI) (online), paper DF4F.3.

1. **Jos de Wit**, Kostas Angelopoulos, Jeroen Kalkman, and George-Othon Glentis. Oral presentation: *Axial super-resolution for optical coherence tomography with the iterative adaptive approach*, at European Conferences on Biomedical Optics 2021 (ECBO) (online), paper ETu3D.7.

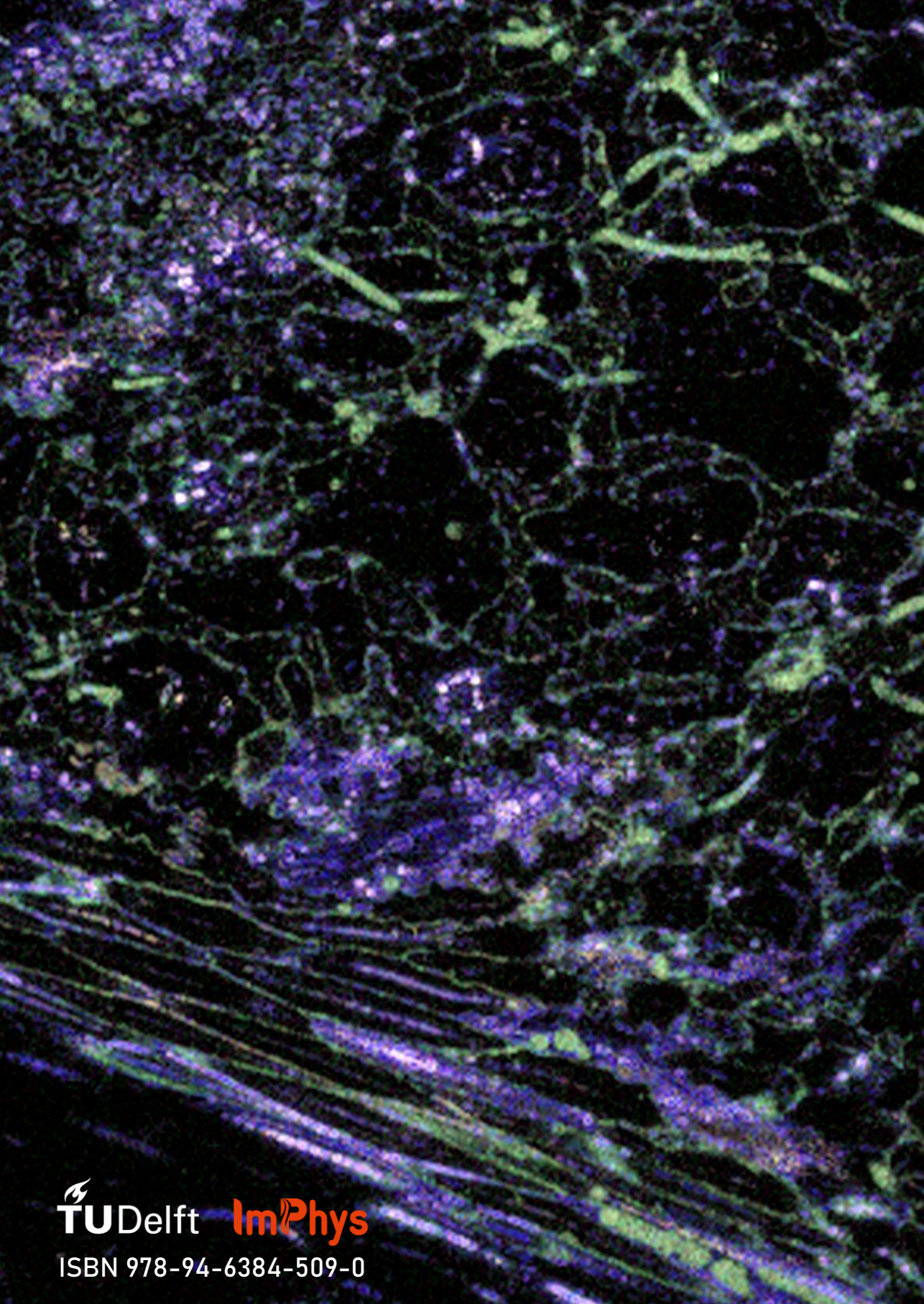

TU Delft ImPhys

ISBN 978-94-6384-509-0